From Model Membranes to Human Interfaces: Lipid Self-assembly, Gradients and Environmental Responses

Labecka, Nikol

2025

Document Version:
Publisher's PDF, also known as Version of record

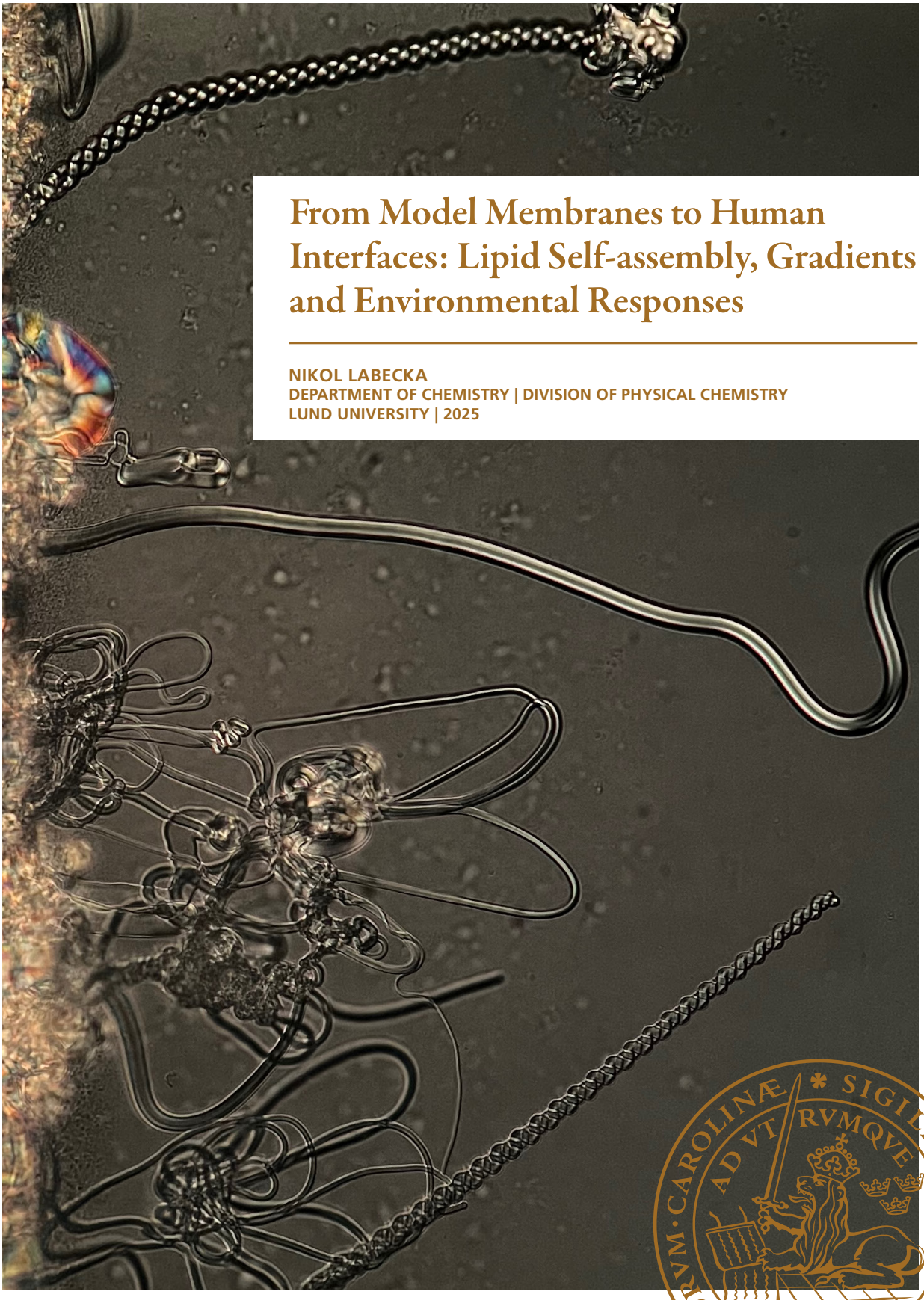

From Model Membranes to Human Interfaces: Lipid Self-assembly, Gradients and Environmental Responses

NIKOL LABECKA
DEPARTMENT OF CHEMISTRY | DIVISION OF PHYSICAL CHEMISTRY
LUND UNIVERSITY | 2025

From Model Membranes to Human Interfaces: Lipid Self-assembly, Gradients and Environmental Responses

From Model Membranes to Human Interfaces: Lipid Self-assembly, Gradients and Environmental Responses

by Nikol Labecka

LUND
UNIVERSITY

DOCTORAL DISSERTATION

Doctoral dissertation for the degree of Doctor of Philosophy (PhD) at the Faculty of Science at Lund University, Sweden. To be publicly defended on 5 December 2025 at 10.00 in B Hall at Department of Chemistry, Lund University.

Faculty opponent:

Associate prof. Adam Squires, Department of Chemistry, University of Bath

Organization: LUND UNIVERSITY

Document name: DOCTORAL DISSERTATION **Date of disputation:** 2025-12-05

Author(s): Nikol Labecka **Sponsoring organization:**

Title and subtitle: From Model Membranes to Human Interfaces: Lipid Self-assembly, Gradients and Environmental Responses

Abstract:

Biological membranes and human interfaces are maintained under non-equilibrium conditions, where they are constantly exposed to different stimuli. The aim of this work is to advance our knowledge of human interfaces and evaluate how they respond to stimuli they naturally encounter, such as fluctuations in external humidity conditions, temperature, or UVB irradiation.

In the first part of this thesis work, the behavior of model systems inspired by human interfaces such as lung surfactant and tear film lipid layer (TFLL) is investigated. Mixtures of phospholipids or phospholipids:triolein dispersed in water are added to a drying-cell setup, where the solutions naturally form multilayer films at the capillary edge exposed to ambient air. The structural characterization along the water gradient is performed by means of synchrotron X-ray mapping, while the composition gradient is traced either by Confocal Raman Microscopy or Confocal fluorescence Microscopy using fluorescent probes. Taken together, the results show that the lipids segregate along the hydration gradient in the vicinity of the air interface. For the DOPC:DPPC systems, the composition gradient preferentially forms a solid gel lamellar phase characterized by shorter-range interbilayer repulsion and reduced swelling in drier conditions. This finding shows that the solutes partition according to their ability to swell in water, which can be generalized to a broad range of soft-matter systems under non-equilibrium hydration gradients. For a system composed of polar and non-polar lipids (DOPC:DOPE:triolein) in water, a pronounced phase segregation in the vicinity of the air interface is observed. The isotropic oil-rich phase wets the lamellar multilayer from both sides and preferentially accumulates at the dry interface over time. These findings highlight a mechanistic framework for how lipid layers covering drying interfaces, such as the TFLL, can maintain the balance between lubrication and barrier integrity.

In the second part of this thesis work, the responses of different components of the outermost skin layer, stratum corneum (SC), are evaluated with respect to external stimuli such as temperature and levels of hydration. The behavior of SC lipids in a water gradient is evaluated by employing the drying-cell setup in combination with the same experimental techniques. The results show that the SC lipids respond to the changes in hydration in a functional way, by altering the balance between solid and fluid lipids within a solid lamellar structure. Furthermore, the antioxidative and structural responses of the SC components to UVB radiation and oxidative stress are evaluated. The results show that UVB has a strong effect on the antioxidative properties of native catalase, while the structural and molecular characteristics of the SC matrix that surrounds the enzyme are largely unchanged for comparably high UVB doses. Taken together, these results highlight the structural integrity of the SC layer and introduce a new experimental approach to evaluate the response of the SC components, which can in turn prove useful knowledge to improve transdermal delivery processes.

Key words: Evapoartion, non-equlibrium, gradinets, model membranse, stratum corneum, responses, UVB.

Supplementary bibliographical information

Language: English **Number of pages**: 216

ISBN (print): 978-91-8096-136-3

ISBN (digital): 978-91-8096-137-0

Recipient's notes: Price: Security classification

Signature  Date 2025-11-06

From Model Membranes to Human Interfaces: Lipid Self-assembly, Gradients and Environmental Responses

by Nikol Labecka

LUND
UNIVERSITY

Cover image: polarized light microscopy image of interfacial lipid film formed in drying-cell setup from a DOPC:DOPE [50:50] + 2.5wt% triolein dispersion in water after 24h.

Department of Chemistry

Faculty of Science

Lund University

SE-221 00 Lund, Sweden

ISBN 978-91-8096-136-3 (print)

ISBN 978-91-8096-137-0 (electronic)

Printed in Sweden by Tryckeriet i E-huset at Lunds Tekniska Högskola (LTH),
Lund, 2025

To my nephews: William, Emilio & Amelia.

Table of Contents

List of Papers

This thesis is based on the following publications, which will be referred to in the text by Roman numerals. The papers are appended at the end of the thesis.

I. **Hydration gradients drive lipid self-segregation**

Nikol Labecka, Jenny M. Andersson, Emma Sparr, Kevin Roger

Submitted, Under revision

II. **Structure and composition gradient across interfacial model lipid tear multilayer films**

Nikol Labecka, Kevin Roger, Emma Sparr

Submitted

III. **Stratum corneum lipids in a hydration gradient: robust lamellar organization and responsive fluidity**

Nikol Labecka, Enamul Haque Mojumdar, Jenny Andersson, Nicolas Velasquez, Sonoki Yoshihiko, Kim Nygård, Mads Carlsen, Kevin Roger, Emma Sparr

Manuscript

IV. **Unraveling UVB effects: catalase activity and molecular alterations in the stratum corneum**

Nikol Labecka, Michal Szczepanczyk, Enamul Mojumdar, Emma Sparr, Sebastian Björklund

Journal of Colloid and Interface Science, 666, (2024), 176–18.8

Author Contribution

I. NL, ES and KR designed the study. NL preformed most of the experimental work. NL performed all data analysis with inputs from KR and ES. NL, ES, and KR wrote the manuscript with inputs from all co-authors.

II. NL and ES designed the study tougher. NL preformed all experimental work and data analysis with inputs from ES and KR. NL wrote the manuscript together with the co-authors.

III. NL preformed the X-ray scattering experimental work under non-equilibrium conditions. NL performed X-ray scattering data analysis with inputs from ES, EHM KR. ES, EHM and NL wrote the manuscript with contributions from all co-authors.

IV. NL, ES and SB designed the study. NL preformed all experimental except SDS-page and FTIR. NL performed most of the data analysis with input from the co-authors. NL, SB and ES wrote the manuscript with inputs from all co-authors.

Popular Summary

Our body is covered by protective barriers such as the tear lipid film covering our eyes, the surfactant layer in our lungs, or the outermost layer of the skin. These layers are composed of diverse protein and lipid mixtures, specifically tailored for a multitude of physiological processes. What they share in common, is that they form an interface that separates a wet inner-body environment from the drier ambient conditions. These layers are constantly exposed to changes in external conditions (such as humidity and temperature) and work against water evaporation, chemical and microbial intrusion, as well as the harmful effects of solar radiation. Understanding how these interfaces respond to fluctuations in their environment and external stimuli is important for human health, skincare, and drug delivery.

Research presented in this thesis shows that lipids in these layers naturally segregate and structurally adapt to a water gradient in the vicinity of an air interface. It is observed that: 1) the phospholipids preferentially form a solid membrane structure with lower permeability to water in the driest conditions, 2) the non-polar and polar lipids phase-separate at the air-interface, forming a multilayer barrier with an oily layer which wets the polar-lipid layer, and 3) the skin lipids mostly preserve their solid structure but are able to adjust their mobile-to-solid lipid fraction in response to changes in external conditions. Additionally, it is observed that UVB irradiation has a more severe effect on the antioxidative properties of the outermost skin layer than on its structural components.

Together, all these insights improve our understanding of how human interfaces, such as the tear lipid film covering our eyes, the surfactant layer in our lungs, or the outermost layer of the skin, function and maintain their protective integrity under stress by structural adaptation. These insights can guide further development of drug delivery processes and be directly applied to the development of new bio-adaptive technologies.

Populärvetenskaplig Sammanfattning

Kroppen är täckt av skyddande barriärer, såsom lipidskiktet som täcker ögats yta, surfaktantlagret i lungorna och det yttersta hudlagret. Dessa barriärer består av komplexa blandning av proteiner och lipider som är specifikt anpassade för olika fysiologiska funktioner. Det de har gemensamt är att de utgör en gränsyta som separerar kroppens inte fuktiga miljö från den torrare omgivningen. Dessa lager är även ständigt utsatta för variationer i den yttre miljön (som relativ fuktighet och temperatur) och måste effektivt motverka vattendunstning, kemiska och mikrobiella angrepp samt skadliga effekter av solstrålning. De underliggande mekanismerna bakom hur dessa barriärer anpassar sig till förändringar i omgivningen är ännu inte fullt förstådda, vilket har motiverat detta arbete. En fördjupad kunskap inom dessa processer är av stor betydelse för människans hälsa, hudvård samt för utvecklingen av mer effektiva metoder för läkemedelstillförsel till kroppens inre.

Forskning som presenteras i denna avhandling visar att lipider i dessa skyddande barriärer segregerar och strukturellt anpassar sig till en vattengradient i närheten av en luftgränsyta. Resultaten visar att: 1) fosfolipider segregerar och bildar helst en fastare membranstruktur med lägre vattenpermeabilitet i lägre vattenhalt i närheten av en luftgränsyta, 2) blandningar av polära och icke-polära lipider fas-separeras och bildar en barriär där ett oljigt (icke-polärt) lager omsluter det polära lipidskiktet, samt att 3) hudlipider behåller sin fasta struktur i en vattengradient men kan anpassa sig genom att öka sin rörlighet i vissa delar av strukturen. Dessutom har det observerats att UVB-strålning har en större påverkan på de antioxidativa egenskaperna i hudens yttersta lager än på dess strukturella komponenter.

Tillsammans bidrar dessa insikter till en fördjupad förståelse av hur kroppens gränsytor fungerar och bevarar skyddande funktion under olika påfrestningar. Dessa insikter kan leda till framsteg inom läkemedelstillförsel och tillämpas i utvecklingen av nya bioadaptiva teknologier.

1. Motivation behind the research questions

Water is the main component of the human body, making up approximately two-thirds of its total mass (1). In the body, water is distributed between the intracellular and extracellular spaces, where it supports a multitude of physiological processes such as thermoregulation, blood pressure regulation, cellular homeostasis, and electrolyte balance, all of which are crucial for survival (1-3). Cellular membranes are highly permeable to water, and water moves between different environments due to the gradient in osmotic pressure (4, 5). Similarly, when hydrated tissue is exposed to ambient air, the imbalance in the osmotic pressure derives the water molecules to transform from a liquid state into a gaseous state and escape from the tissue in a process called evaporation (6). In nature, different strategies have been developed to minimize water evaporation across biological interfaces and to protect against the potential threat of drying out. In the human body, one can distinguish between several biological interfaces (biomembranes) such as the skin, the alveolar interfaces in the lungs and the tear lipid layer on the surface of the eyes, which are exposed to air. These biomembranes are mainly composed of a mixture of different lipids and proteins specifically tailored for a multitude of physiological processes, for example enabling breathing, providing mechanical and antioxidative protection and supporting visual perception (7, 8). What the above-mentioned biomembranes share in common is that they function at the boundary between dry and hydrated environments, constantly adapting to non-equilibrium conditions.

The aim of this thesis is to advance our understanding of biomembrane responses to the water gradient and other stimuli that they naturally encounter, such as UVB radiation. The compositions of the lung surfactant layer covering the alveolar interface and the outermost tear lipid layer, serve as sources of inspiration for the composition of the model systems used in **Paper I and II**, while the response of different protein and lipid components of the outermost skin layer, known as stratum corneum (SC), are evaluated in **Papers III and IV**. These biological interfaces will now be described in greater detail, along with how they inspired the research questions addressed in the papers.

1.1 Biological membranes and Human interfaces

1.1.1 Lung surfactant

Breathing is one of the most vital processes, enabling oxygen uptake and carbon dioxide release between the air in the alveoli of our lungs and the blood in pulmonary capillaries (9, 10). The alveolar interface is covered by a lung surfactant layer which separates the hydrated epithelial tissue from the air. The lung surfactant layer is composed of approximately 90 wt% lipids and 10 wt% proteins, where the majority of the proteins belong to the surfactant proteins: SP-A, SP-B, SP-C and SP-D (11, 12). The lipid matrix is mainly composed of phospholipids, where the majority belong to the zwitterionic phosphatidylcholines (PCs) (>80 %), with the fully saturated dipalmitoyl-phosphatidyl-choline (DPPC, 16:0/16:0-PC) as the main component. The remaining phospholipids belong to the phosphatidylglycerol (PG), phosphatidylserine (PS), phosphatidylethanolamine (PE) and phosphatidylinositol (PI) classes, and cholesterol is also found (13, 14). The main function of the surfactant layer is to act as a protective barrier against exogenous substances and to prevent alveolar collapse during respiration (15, 16). While the structural response of the surfactant layer with respect to lung expansion and compression is still under debate, a common view suggests formation of a lipid monolayer at the interface associated with a multilayer architecture that responds to the inhalation and exhalation cycle (15, 17). A schematic model of the lung surfactant multilayer architecture is shown in Fig. 1 (12).

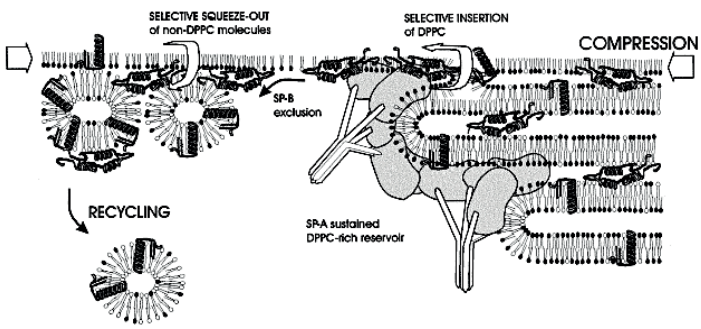

Figure 1. Schematic model of surfactant layer from 1998. Adopted from (12) with permission from Elsevier.

The deficiency of the lung surfactant layer is particularly linked the Neonatal Respiratory Distress Syndrome (NRDS), which is caused by the inability to inflate the lungs (18). The early replacement therapy based on aerosolized DPPC had no effect on the survival rate of premature infants suffering from NRDS (19). Subsequent developments in our understanding of the biophysical surfactant properties have led to improved lung surfactant replacement products (20-22), but the animal-derived replacement products still remain far superior to the synthetic ones (23, 24). This motivates further study of the behavior of the model lipid mixtures at the drying interface. It has been shown that one of the clinically used lipid mixtures (Curosurf) exhibits complex phase behavior in the vicinity of an air interface, forming coexisting lamellar structures that would otherwise not form under equilibrium conditions (25). This finding has been the primary source of inspiration for further evaluating the determining factors behind the gradient formation in the aqueous phospholipid mixtures in the vicinity of an air interface. The key questions asked in **Paper I** and initiating work done in **Paper II** are:

- Does the water gradient introduce a gradient in the phospholipid composition?
- How do these gradients influence the self-assembly behavior in the vicinity of an air interface?

In **Paper I,** the behavior of lipid mixture composed of two PC phospholipid (DOPC and DPPC) is evaluated along the water gradient. The two lipids have the same headgroup characteristics but different hydrocarbon chains, which makes them to preferentially self-assembly to liquid- and solid lamellar structures, respectively. In **Paper II**, this work is extended to study the behavior of two phospholipid with different headgroups but the same hydrocarbon chains characteristic namely, DOPC and DOPE. In this system, one of the lipids (DOPE) promotes formation of nonplanar self-assembly structures.

1.1.2 Eye lipid layer

Another example of a biological interface that separates a water-rich environment from the dry air is the outermost layer of our eyes, known as the tear film lipid layer (TFLL). The TFLL is ca. 100 nm thick and located on the surface of the aqueous tear solution, which is located on top of the corneal epithelium cells and separated by a mucin layer (26-28). The TFLL has many vital functions such as preventing water evaporation from the aqueous phase, acting as a defensive barrier against external contamination

and pathogen intrusion, and serving as a lubricant to smooth the ocular surface (7, 29, 30). While some of these functions are directly comparable to those of the lung surfactant layer, the molecular composition and interfacial structures are clearly different between the two systems. The TFLL is mainly composed of non-polar lipids (up to 80%), together with polar lipids and lower amount of proteins (31-33). The nonpolar lipids are mainly secreted by the Meibomian glands from the eyelids during blinking, while the polar lipids and other aqueous solutes are thought to reach the interface from below (7, 34). Most of the non-polar lipids belong to the classes of wax esters, cholesteryl esters, and triglycerides, which naturally form an isotropic oily phase rather than self-assemble into mesostructures. The polar lipid components mainly consist of PCs, PEs and free fatty acids (31-33), which have a natural tendency to assemble at water-oil and water-air interfaces. Due to the polar and non-polar nature of the lipids in the TFLL layer, several models propose that the lipids phase-separate into a multilayered structure where the polar lipids stabilize the water-oil interface formed by the non-polar lipids (35-37). A schematic model of the tear film and TFLL is shown in Fig. 2 (37).

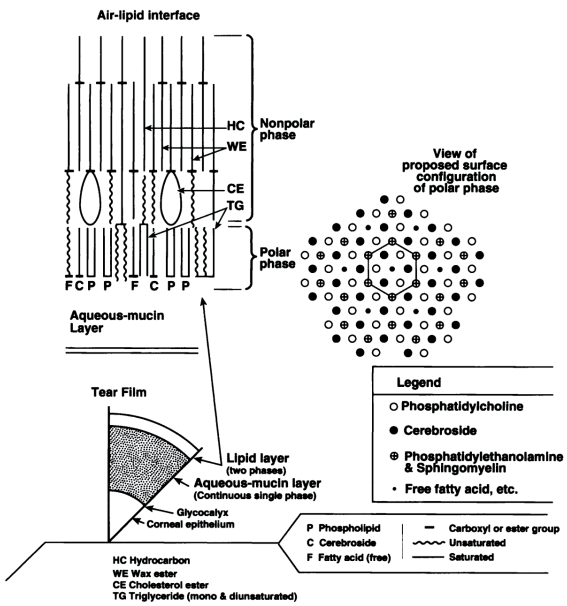

Figure 2. Schematic model of the tear film and TFLL from 1997. Adapted from (37) PMC Open Access PMID: 9440164.

One important observation regarding the TFLL, is that when the eye is forced to stay wide open, the TFLL film deteriorates quickly and breaks within a minute. The so-called tear break-up time has been widely used in eye health diagnostics and correlated with several diseases (38, 39). For example, in dry eye disease, the integrity of the TFLL is compromised immediately or within few seconds after blinking, which results in desiccation and irritation of the ocular surface (34). The instability of the TFLL film has more recently been linked to Meibomian gland dysfunction and altered lipid secretion (40, 41) highlighting the importance of the lipid matrix composition. These insights have been used in the development of new lipid-based therapeutics, resulting in better film stability and lubrication than artificial saline tear solutions (42, 43). Furthermore, the polar and non-polar nature of the TFLL lipids has enabled development of different formulation strategies. For example, liposome-based formulations exploit the self-assembly behavior of phospholipids to form lipid vesicles as pharmaceutical carriers, whereas emulsion-based formulations use non-polar lipid droplets as delivery carriers (44, 45). These formulations can be designed for different target regions with different objectives, for example, to act as topical lubricants or to deliver active substances to the corneal barrier of the eye (42, 46). What they have in common is that when deposited on the ocular surface, they become rapidly mixed with the tear liquid and washed away. The remaining formulation residues encounter a permeability barrier (for example, the TFLL or the mucin layer), often resulting in the delivery of a small fraction of the formulated dose (43, 47). These insights motivate further study of the behavior of lipid vesicles and oil droplet formulations in the vicinity of an air interface. Concentration of such systems (composed of polar and non-polar lipids) at a drying interface can result in vesicle fusion, lipid segregation and macroscopic phase separation, which can be used in development of new formulation strategies. The composition of the formulations used in **Paper II** is inspired by the natural components of the TFLL, where a triglyceride (triolein) is used as the non-polar lipid representative and two phospholipids with different self-assembly properties (DOPC and DOPE) are selected as the polar lipid representatives. The interfacial organization of these systems can mimic the TFLL and provide further insight into the behavior and response of the layer to a water gradient. The key questions asked in **Paper II** are:

- How are the polar and non-polar lipid mixtures structuring at the drying interface?
- Can the observed phenomena be related to the properties of the tear lipid layer?

1.1.3 Stratum corneum

Skin is the largest organ of the human body, which protects us from chemical and microbial intrusion as well as prevents desiccation. The outermost layer of the skin, known as the stratum corneum (SC), separates the viable part of the skin from the ambient air (48). The SC is approximately 20μm thick and characterized by a low water content. It is mainly composed of dead corneocyte cells (ca. 85wt% of dry SC mass) (49), which are joined together by corneodesmosomes (50) and embedded in a multilamellar lipid matrix (51). Structurally, the SC resembles a wall of bricks and mortar (Fig. 3A). The outer shell of the corneocytes (bricks) is composed of a cornified cell envelope of highly insoluble proteins (50). An important observation is that the corneocytes can swell and take up a substantial amount of water (52, 53). This implies that the cornified envelope is penetrable to water and most probably to other small polar molecules. The intracellular region of corneocytes is filled with solid keratin filaments, which reinforce the corneocyte structure (48). Each keratin filament is ca. 8 nm thick and composed of eight protofilaments. Each protofilament is composed of side-by-side stacked heterodimers with a coiled-coil structure. The heterodimers are strictly 50nm long and composed of one acidic (type I) and one neutral or basic (type II) keratin monomer, where each monomer has a secondary α-helix structure (54). It has been shown that the inter-chain distance (d-spacing) in the α-helix structure of the coiled-coil filament starts swelling when the SC is exposed to RH above 80% (55).

The extracellular lipid matrix is regarded as the main barrier component of the SC against water evaporation and chemical uptake, as it forms the only continuous path for transdermal entry (56). The lipid matrix is composed of an equimolar mixture of ceramides (CERs), free fatty acids (FFAs) and cholesterol (57-59). The matrix exhibits extraordinary species diversity, with up to 1,500 different CERs species identified to date (60). The majority of the CER and FFA lipids have exceptionally long hydrocarbon chains (from C12 to C36 and on average C20-22) and are fully saturated (61), which in turn contributes to the crystalline nature of the lipid matrix. Several studies have reported that the structure consists of multilamellar stacks with two typical repeat units of ca. 130Å and 60Å with orthorhombic and hexagonal chain packing. These repeat units are commonly referred to as the long periodicity phase (LPP) and the short periodicity phase (SPP) (62-64). Several studies have also shown that not all SC lipids in the lamellar matrix are solid, a smaller fraction of fluid lipids have been identified (65-70). The presence of a fluid lipid phase domain in the lamellar structure can have profound consequences for the transport efficiency of compounds across the lipid matrix, as the permeability of the fluid lamellar is several orders of magnitude larger than that of the solid lamella (65, 71). Fig. 3 shows the “brick and

mortar model" of the SC structure (63), and the solid-fluid lamellar model of the LPP phase which composes the intercellular lipid matrix (mortar) (64).

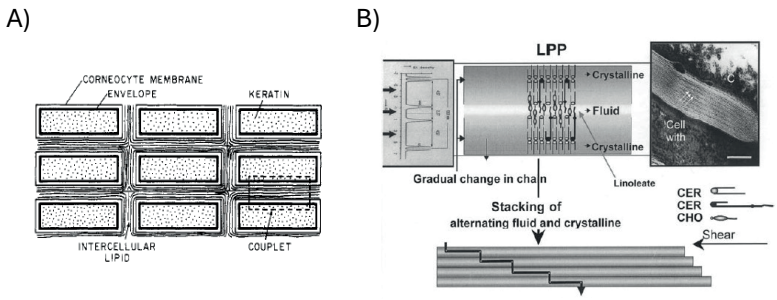

Figure 3. A) Schematic illustration the "Brick and Mortar" model of the SC layer proposed in 1988. Adopted from (63) with permission from American Chemical Society. B) Schematic model of the LPP structure found in the intercellular lipid matrix. Adopted from (72) with permission from Elsevier.

The evaporation rate through the SC layer displays a non-linear relationship with respect to the relative humidity (RH) of ambient air. The evaporation rate is very low and virtually constant for all RH below ca. 85% and decreases further with an increasing RH (73, 74). It has been suggested that this response can be attributed to the phase adaptation of the SC lipids, as different lamellar phases have significantly different permeability properties (75, 76). Although the behavior of SC lipids has been extensively characterized in fully hydrated conditions, little is known about their self-adaptation in a water gradient. This has motivated further study of the structural behavior and response of SC lipids in drying conditions. In **Paper III**, extracted SC lipids from a porcine source are used and the response to change in the water content and temperature is examined. In this work we ask:

- Do the SC lipids form the same structure in dry and fully hydrated conditions?
- Is there any difference in the mobility of different SC lipid components in the structure?
- Are there any structural differences when the SC multilayer is formed at a drying interface compared to the bulk?
- How does the structure respond to an abrupt change in hydration?

The SC layer contains relatively large amounts (ca 20 wt% of dry SC) of small polar molecules (osmolytes), chromophores and antioxidative enzymes acting together as an additional protection against dehydration, oxidative stress and photodamage (77, 78). It is well established that the solar UV irradiation is one of the major threats compromising the integrity of the skin (79-81). Depending on the incoming wavelength, the UV rays can penetrate into the different depths of the skin layer and cause photodamage. In particular, the short wavelength UVB rays are almost fully absorbed within the epidermis layer of the skin (79). The broadband UV rays can either be absorbed directly by the cellular components resulting in chemical bond disruptions (for example with pyrimidine dimers), or indirectly by exciting endogenous or exogenous sensitizers leading to the formation of reactive oxygen species (ROS) (79-81). Increased levels of ROS cause oxidative stress and can further damage other protein and lipid components in the tissue. For this reason, oxidative stress is pointed out as one of the main contributing factors to the development of skin disorders as skin aging, dermatitis and cancer (82, 83).

Catalase is an antioxidative enzyme, abundant in both the epidermis and the SC layer of the skin. Its native function is to scavenge ROS specie hydrogen peroxide (H_2O_2) by transforming it into oxygen gas (O_2) and water (H_2O) (84-86). The antioxidative activity of the catalase in the SC has been reported to undergo seasonal variation, where its activity is reduced during the summer season due to sun exposure (87). Although there are several studies evaluating the effect of UVB irradiation on the different biological and mechanical aspects of the epidermis integrity (81, 88-90), it is still unclear what effect UVB irradiation has on the SC layer alone. This has motivated further study of the UVB effects on the structural and antioxidative properties of the SC matrix, conducted in **Paper IV**. The key questions behind this work are:

- How does the native catalase respond to an increasing UVB dosage, and is this effect reversible?
- Does UVB irradiation alter the structure of SC components?
- Does UVB irradiation influence the molecular dynamics in the SC components?

In this work, different SC matrixes (from intact SC layer – to extracted corneocytes) is exposed to successively increasing UVB and hydrogen peroxide dosage. The deactivation of native catalase in the corneocytes matrix is studied and the molecular changes in the structure and mobility of different layers are evaluated.

2. Theoretical Background

Lipids comprise a broad group of organic compounds (such as phospholipids, fatty acids, waxes and sterols) which are generally insoluble in water but soluble in organic solvents. This property arises from a large hydrophobic region in the molecule, often composed of long hydrocarbon chains or ring structures. The physicochemical properties of lipids are determined by the molecular architecture of their hydrophobic and hydrophilic regions (91, 92). For example, the length of the hydrocarbon chains, their branching, and the number of double bonds, together with the properties of the hydrophilic lipid headgroup such as size and charge, control the phase behavior, melting point, and maximum solubility in different solvents (93, 94). In the case of polar lipids, also called amphiphilic lipids, the properties of the hydrocarbon chains in relation to the headgroups also determine the self-assembly behavior, which leads to formation of mesoscopic structures in water such as micelles and liquid-crystalline lamellar phases. The self-assembly structures can be thermodynamically stable or dispersed into metastable vesicles or lipid nanoparticles (92, 94). The aim of this chapter is to briefly describe the behavior of the various lipid systems dispersed in water that have been studied in this thesis work (**Papers I-III**). The self-assembly phenomena of lipids in other solvents are outside of the scope of this thesis. The emphasis in this chapter is on the equilibrium self-assembly of phospholipids, together with how different external factors and composition can influence the behavior. The final section of this chapter introduces the non-equilibrium behavior that can occur in the vicinity of an air interface in aqueous lipid systems.

2.1 Lipid Self-assembly

Self-assembly refers to a process where molecules spontaneously organize into a structure without any prior guidance, after their solubility limit in water is exceeded. For amphiphilic lipids, this process is mainly governed by the hydrophobic effect which drives the non-polar part of the molecules (hydrophobic hydrocarbon tails) to cluster together and causes the hydrophilic headgroups to rearrange towards water.

Which self-assembly structure is formed depends on the properties of the self-assembling molecule, the properties of the solution, as well as the experimental conditions (95). The non-polar lipids (such as waxes and oils) do not self-assemble into mesoscopic structures but rather phase separate into droplets or macroscopically segregated phases (96-98).

There is a large variety of self-assembly structures that amphiphilic lipids can adopt. These structures can be classified by 1) the geometry in one, two, or three dimensions, 2) the arrangement of the hydrocarbon chains within the structure, and 3) the orientation of the hydrophilic and hydrophobic part of the lipid with respect to the surrounding medium (normal or inverted structure) (94). Conceptually, the collective behavior of amphiphilic lipids can be described in terms of single molecule parameters such as the effective headgroup area a_0, the length of the hydrocarbon chain l, and the hydrophobic volume V, in terms of a packing parameter:

$$N_s = \frac{V}{a_0 l} \tag{1}$$

The packing parameter, N_s, also known as the surfactant number, gives a ratio between the size of the polar and non-polar parts of the molecule and relates to the preferred curvature of the mesoscopic structure. The single molecule parameters, the N_s values and how they relate to the formed self-assembly structures is displayed in Fig. 4.

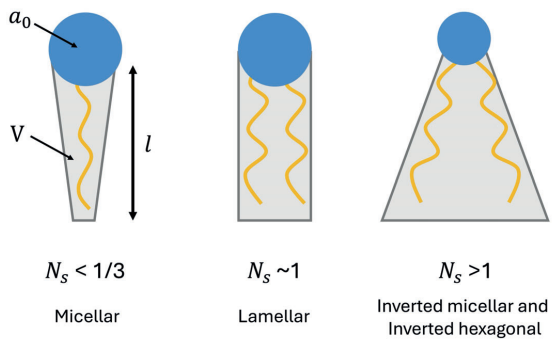

Figure 4. Schematic illustration of how the single molecule parameters influence the packing parameter (N_s) and relates to the formed self-assembly structure such as micellar, lamellar, inverted micellar and inverted hexagonal phases. Blue color corresponds to the effective headgroup (a_0), while hydrocarbon chains with length l are colored in orange, the hydrophobic volume (V) colored in gray.

For $N_s < 1$, the volume of the hydrophobic part is smaller than the headgroup part, and the lipids self-assemble to curved aggregates with the hydrocarbon tails densely packed together (as in micelles). The inverse is true for lipids with $N_s > 1$. For $N_s \approx 1$, the molecules don't favour any preferential curvature and self-assembles into planar bilayer structures (92, 99). There are several chemical and physical factors that can affect the interactions between the lipid headgroups and tails and thus influence the apparent packing parameter of the lipid (92, 99). These are briefly described in the following section.

2.1.1 Factors affecting lipid self-assembly

Lipid Structure

In this work, the lipid self-assembly structures were mainly evaluated for different subclasses of glycerophospholipids. The common feature of glycerophospholipids is that they all have a polar headgroup attached to the 3rd position of sn-glycerol via a phosphate group. For example, the choline, and ethanolamine headgroups are both zwitterionic, yet have different headgroup size and thus different headgroup area (a_0) parameters. A serine headgroup has similar a_0 compared to the choline headgroup but is negatively charged. When one of these headgroups is coupled together with two hydrocarbon chains via the remaining sites of the sn-glycerol backbone, it forms the basis for what is known as phosphatidylcholine (PC), phosphatidylethanolamine (PE) and phosphatidylserine (PS) phospholipids (99). The length and chemical structure of the two hydrocarbon chains tune the N_s parameter (by affecting V and l in eq. (1)) and determine the state (solid or fluid) of the hydrocarbon chains. Besides the length, the number of double bonds also has a strong effect on the conformational arrangement of the hydrocarbon chains within the self-assembly structure (92). For example, when DOPC is composed of two 18-carbon (C18) long chains with two cis-double bonds [18:1Δ^9] is mixed with water at room temperature, it assembles into a liquid crystal lamellar (L_α) structure with fluid chains (trans-gauche conformation). While DPPC, composed of two fully saturated C16 long chains [16:0], assembles into a lamellar gel phase with tilted solid (all-trans conformation) chains ($L_{\beta'}$) at the same conditions. Changing the PC headgroup to PE for the same [18:1Δ^9] hydrocarbon chains, changes the mesoscopic structure from L_α for DOPC to an inverted hexagonal phase (H_{II}) phase for DOPE (94). This demonstrates the sensitivity of the self-assembly phase behavior to the chemical alterations in the phospholipid structure. The chemical structure of the DPPC, DOPC and DOPE lipids together with the packing parameter (N_s) are shown in Fig. 5. The long and saturated ceramides found in the lipid matrix of the stratum

corneum (SC) are mainly adopting solid lamellar structures (62, 64). The skin ceramides are usually composed of a C20-22 long saturated hydrocarbon chain coupled to a C18 sphingoid base (61, 100).

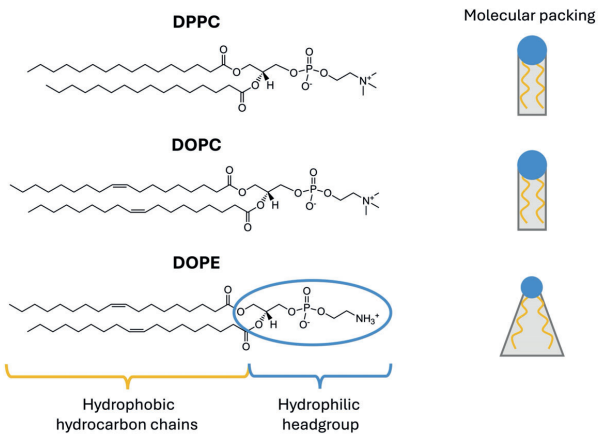

Figure 5. Chemical structures of DPPC, DOPC and DOPE, together with the packing parameter (Ns) in excess water at room conditions. The DPPC and DOPC have $N_S \approx 1$ forming lamellar structures, while the DOPE has a $N_S > 1$, promoting formation of non-planar self-assembly structures as the inverted hexagonal phase.

Beside the lipid structure, the external parameters such as temperature, level of hydration, solution conditions such as ionic strength and pH, and bulk additives can tune the phase behavior of amphiphilic lipids in water. In this work, the effect of temperature and level of hydration was of main interest and will be described in greater detail.

Temperature

Lipid self-assembly structures have a characteristic melting temperature (commonly denoted as T_m), above which the hydrocarbon chains adopt a fluid arrangement, similar to that found in liquid crystal structures (94). For certain systems, the temperature increase can have a more pronounced effect on the effective volume of the hydrocarbon chains (V, increasing the value of N_s) and a transition from lamellar to a non-lamellar structure can be induced. For example, DPPC lipids in fully hydrated conditions phase transition from a tilted lamellar to a tilted rippled gel phase ($L_{\beta'}$ to $P_{\beta'}$) at 35 °C and further to a liquid crystalline lamellar phase ($P_{\beta'}$ to L_α) at 41.5 °C. On the other hand, the packing parameter (N_s) of DOPE lipids in fully hydrated conditions

is substantially affected by the temperature. The system forms a liquid crystal lamellar (L_α) phase below ca. 8.5°C, while above this temperature, an inverted hexagonal phase (H_{II}) is formed instead (94).

Water content

In fully hydrated conditions, the self-assembly structure is fully swollen, any further addition of water will form a separate excess bulk phase. The fully swollen self-assembled structure can either be present as a macroscopically segregated phases (in equilibrium) or dispersed into smaller particles that are homogeneously distributed in the aqueous phase e.g., vesicles or hexosomes or cubosomes particles. The dispersed particles are metastable, and they will aggregate and fuse together over time to form the equilibrium phases (101, 102).

Of particular interest in this work (**Papers I and II**) is the observation that the phase behavior of phospholipids can be altered by changing the level of hydration in the system at constant temperature. The water chemical protentional ($\Delta\mu_w$) is a thermodynamic quantity that describes the free energy (G) per mole of water molecules, and can be directly translated to the water activity (a_w):

$$\Delta\mu_w = \mu_w - \mu_o = RTln\, a_w = \left(\frac{\partial G}{\partial n_w}\right)_{T,P} \quad (2)$$

where μ_o is the standard chemical potential of pure water, R is the gas constant and T is the temperature. Equilibrium conditions require that the chemical potentials of all components are the same in all phases, which implies that there is no net transfer of water mass between coexisting phases. When the system is in equilibrium with the vapor phase, the water chemical potential can be directly deduced from the ratio between the partial vapor pressure of water (p_w) and its saturation vapor pressure (p_w^0), which is generally referred to as the relative humidity (RH): $a_w = \frac{p_w}{p_w^0} = \frac{RH(\%)}{100}$. The a_w of a system range from 0 in water-free samples up to 1 for pure water (6, 103, 104). The relationship between the RH and the amount of water in the sample (wt%) is non-trivial and depends on several factors, such as the chemical composition and phase structure. This relationship can be determined experimentally and is referred to as a sorption isotherm. (105-107)

The water chemical potential is also related to the osmotic pressure Π_{osm} of the solvent, and for lamellar structures it can be directly translated into the force between two planar bilayer surfaces:

$$\Delta\mu_w = -V_m\Pi_{\text{osm}} = -V_m\frac{F}{area} \quad (3)$$

where V_m is the molar volume of the water. At equilibrium, there is a balance between the repulsive and attractive interlamellar forces, which will in turn determine the interbilayer aqueous layer separation. The phases with fluid chain arrangement (as in L_α) display lipid protrusion and bilayer undulations which are restricted at shorter interbilayer separations (95). This implies stronger (entropy-driven) interlamellar repulsion in the L_α phase as compared to the solid lamellar L_β phase (108).

Dehydration of a lipid lamellar system leads to deswelling and can further promote transitions to phases with more closely packed lipids or inverted phases. For example, fully hydrated DPPC at temperatures above T_m (42 °C) goes through a L_α to L_β phase transition upon dehydration (109), and DOPE at 20 °C goes through a H_{II} to L_α phase transition (via phase co-existence) upon dehydration. The phase diagram of DOPE:water system is attached in Fig. 6 (110).

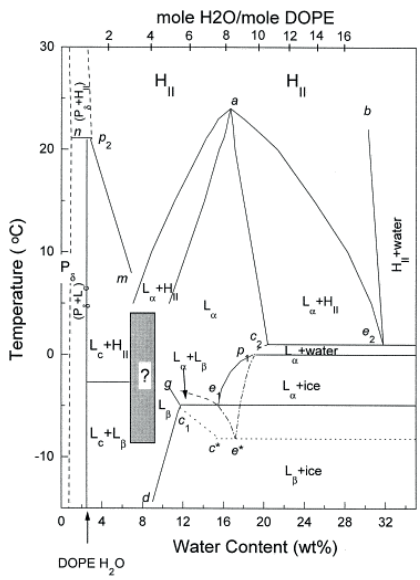

Figure 6. Phase diagram of DOPE: water system adopted from (110), used under a Creative Commons CC-BY-NC-ND license.

Lipid Composition

The phase behavior can become more complex when different phospholipids are mixed in an aqueous system. Phospholipids with similar physicochemical properties generally mix well together within the self-assembly structure (homogeneous distribution). On the other hand, mixing phospholipids with different headgroup and hydrocarbon chain properties can lead to segregation into separate phases with different composition and structure (phase coexistence), and thus heterogeneous distribution of the lipids and water between the self-assembly structures (111, 112). For two lipid components (i = 1, 2) and water (*w*) forming two coexisting phases (α and β), the chemical potential of each species must be equal in each phase ($\mu_1^\alpha = \mu_1^\beta, \mu_2^\alpha = \mu_2^\beta$ and $\mu_w^\alpha = \mu_w^\beta$) (113). Depending on the physicochemical properties of the lipids, mixing of two lipids can also result in the formation of new mesoscopic phases that are not formed in systems containing single phospholipid components (25).

2.1.2 Phase diagrams

Phase diagrams are used to map out the phase behavior of a systems with respect to the changes in composition and external conditions such as temperature and pressure. The experimental approach behind the characterization of the phase behavior is briefly outlined in chapter 3, while this subchapter focuses on how to read and navigate binary and ternary phase diagrams. As described in the previous section, phospholipids spontaneously self-assemble into mesoscopic phases, and any changes in the composition or external conditions can then influence the phase behavior. When the system reaches equilibrium, the self-assembly does not change over time and the behavior can be systematically mapped out versus parameters that can be varied. Thus, the phase diagrams provide a link between the thermodynamic parameters, mesoscopic structure at equilibrium and the underlying intermolecular interactions driving self-assembly (114).

The thermodynamic parameters in a system can be divided into 1) extensive, which depend on the size of a system such as volume and mass, and 2) intensive, which are independent of the size of the system such as temperature, pressure, concentration and chemical potential. The intensive parameters determine which self-assembly phase is formed and their variability is displayed on the axes of a phase diagram. The Gibbs phase rule can be used to relate the number of independent intensive variables that can be freely changed (degrees of freedom, F) to the number of components C in a system and the number of P phases. For a system kept at constant pressure (isobaric) while the intensive variable of temperature is free to change, the Gibbs phase rule is given by:

$$F = C - P + 1 \quad (4)$$

For example, for one lipid component in water (C = 2), temperature and the relative composition of the components can freely vary within one phase region (P =1) in the phase diagram. However, in the two-phase region (P = 2), the degree of freedom is 1, which means that any change in temperature comes with a change in the relative composition of the phases (114). The relative amount of each phase in the two-phase sample can then be determined by the lever rule, where the fraction of each phase (φ_i where $i = \beta \; or \; a$) is related to the distance (l_α, l_β) from the point corresponding to the sample composition to the phase boundary of the single phases (with molar composition of B in phase β as $\chi_{\beta 2}$ and A in phase β as $\chi_{\alpha 2} = 1 - \chi_{\beta 2}$) along the tie-line. This is graphically represented in Fig. 7 where yellow star indicates the sample composition. According to the lever rule, the fraction of phase β (φ_β) is given by: $\varphi_\beta = \frac{l_\alpha}{l_\alpha + l_\beta} = 1 - \varphi_\alpha$. This means that when the composition of the sample is changed, for example the amount of component B is increased (which shifts the yellow star to the right), the relative fraction of phase β with respect to α ($\varphi_\beta / \varphi_\alpha$) becomes larger (111, 114).

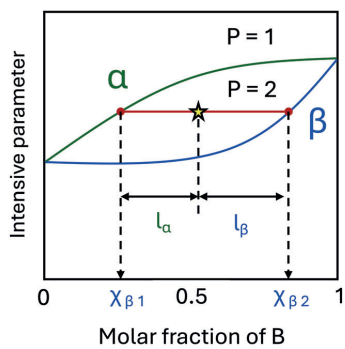

Figure 7. Schematic phase diagram of binary mixture (of A and B) illustrating lever rule. P represents the number of coexisting phases (here, α or β), and C is the number of components (here, C = 2). The fraction of each phase in the coexisting region is determined by the distances l_α, l_β from overall composition (here indicated by a start).

The number of degrees of freedom increases by one for each new component added to the system. For three-component systems (C = 3), the phase diagrams are often represented by a triangular plot where each corner corresponds to one of the pure components, and both temperature and pressure are kept constant (114). The ternary phase diagram of DOPC:DPPC:water shown in Fig. 8 was characterized in **Paper I**

(the data is included in the SI section of **Paper I**). Under isothermal and isobaric conditions, the number of intensive variables that can be freely changed in a system within a given state is described by Gibbs phase rule $F = C - P$. In a single phase region (P = 1), F is equal to 2, meaning that the composition of two components can be varied independently within the single phase. At phase coexistence (P = 2), there is only one degree of freedom left (F = 1), which means that the relative composition of two components is constrained. In two-phase regions, this can be represented by a tie-line. The constraint comes from the fact that for each component, the chemical potential must be the same in each phase. For an aqueous ternary system, this also implies that the two remaining components are free to rebalance (partition) in response to any change in the water chemical potential. (113) The lever rule can be used to estimate the relative amount of each phase as long as the tie-lines are known. This is graphically shown in Fig. 8, where the l_α, l_β distances from a given composition (indicated by star) to the phase boundaries (L_α and $L_{\beta'}$) determine the relative fraction of each phase in the two-phase region.

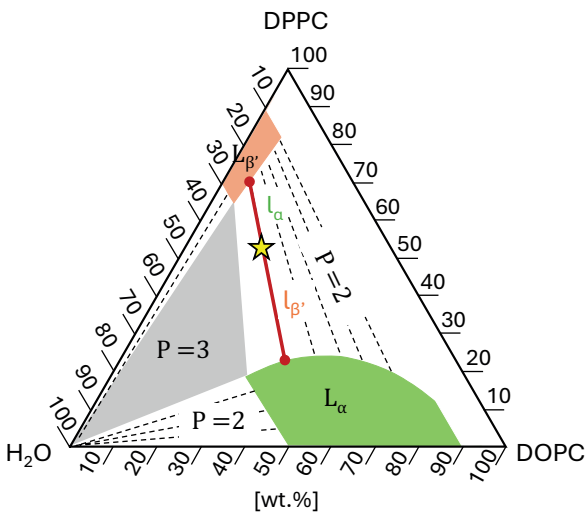

Figure 8. Ternary phase diagram of DOPC:DPPC:H_2O system at 25°C characterized in **Paper I.** P represents the number of coexisting phases (here, Lα, Lβ, water),The red line in the two-phase region indicates the composition of two phases in equilibrium. The relative fraction between the two phases at each point long the line (here indicated by a star) shifts according to the lever rule.

2.2 Non-equilibrium caused by water evaporation

Evaporation is a surface located phenomenon where the molecules in the liquid state transform into a gaseous state (103, 104). Clearly, this phenomenon is not unique to water and there are many examples of other solvents and solutes that are even more volatile than water. The volatility of a molecule is mainly governed by the intermolecular interactions in the condensed phase. Consequently, different components in a liquid mixture may be more or less prone to evaporate into the ambient air, which induces gradient formation the vicinity of the water air interface (115-118). In this thesis work (**Papers I - III**) the behavior of polar lipids, non-polar lipids and skin lipid extracts has been studied in non-equilibrium conditions imposed by a water gradient. This subchapter focuses on the crucial phenomena that can occur in aqueous lipid systems in the water gradient when exposed to the air.

Evaporation is driven by the difference in chemical potential across the interface and is related to the vapor pressures of the molecules in question. For pure water, the gradient in chemical potential is simply related to the relative humidity (RH) of the ambient air (as discussed in chapter 2.1.1) with respect to the water chemical potential in the bulk solution ($\Delta\mu_w = \mu_{RH} - \mu_{bulk}$). Thus, the evaporation rate of water is faster when the system is exposed to the lower RH conditions (92). The net flow of mass (flux, J) of component *i* (here denoting water) in a concentration gradient c, can be described by the generalized Fick's first law:

$$J_i = -\frac{D_i}{RT} c_i \left(\frac{d\mu_i}{dz}\right) \tag{5}$$

Where $d\mu_i$ is the difference in chemical potential along direction z, D is the diffusion coefficient, R is the gas constant and T is the temperature. This equation relates the molecular flux to the gradient in chemical potential and the diffusion properties of the molecule in water (119). For example, for a dilute spherical particle with radius r, the diffusion coefficient D is given by the Stokes-Einstein relation: $D = \frac{k_B T}{6\pi\eta r}$, where k_B is the Boltzmann constant and η is the viscosity of the medium (120). In aqueous solution containing dispersed lipids, the evaporation of water leads to the accumulation of the non-volatile lipids in the vicinity of the air interface. In this case, the system is in non-equilibrium conditions forming different concentration gradients with respect to water. For non-polar lipids, the concentration gradient can result in phase separation and the formation of an oily layer at the water surface. A classic example of such a system is the separation of olive oil in water. For amphiphilic lipids on the other hand, the

interfacial accumulation results in the formation of a monolayer at the interface and further concentration can promote the formation of self-assembly structures in the opposite direction of the water gradient (25, 117, 118). Since the self-assembly phases can adapt and transition with respect to the local water chemical potential, they can be regarded as a structurally responsive barrier for water evaporation (117). Nevertheless, both the phase separated oily layer and the formed mesophase structure, provide a barrier for water transport from the bulk solution to the air interface, significantly slowing down the rate of evaporation.

The evaporation rate from the system strongly depends on the water permeability across the interfacial layer, which can be expressed in terms the permeability coefficient: $P_w = \frac{D_w K_w}{l}$ where l is the thickness of the barrier layer, D_w is the diffusion coefficient of the diffusing species in the layer (here water in the oily layer or bilayer), and K_w is the partition coefficient which relates the solubility of the water in the layer as compared to the surrounding solution. Since the diffusion coefficient of water in different liquid lipid layers is of the same magnitude as in water, the effective water permeability (normalized to the thickness of the phase) is mainly determined by the partition coefficient K_w (119).

The self-assembly phases will adapt to the (local) water chemical potential. For multicomponent lipid systems forming more than one phase, it is possible that the water gradient drives gradients also in the lipid composition, which can result in situations where the proportions of the lipids is not constant along the water gradient (113, 117). The self-assembly behavior of two phospholipids in a water gradient and how it leads to phase segregation in the vicinity of the air interface is the key finding of **Paper I.** To examine how the self-assembly is guided by the gradient in composition, a phase diagram of a DOPC:DPPC:H_2O system is used. If the ratio between the two lipids is kept constant as in the initial bulk mixture, the trajectory path in the phase diagram follows a straight line towards decreasing water content when approaching the dry air interface. This is schematically shown in Fig. 9 for a DOPC:DPPC system with an initial $[20{:}80]_{wt\%}$ ratio in water. In this case, the straight line (black dashed) indicates the formation of two coexisting phases along the entire water gradient, while the relative proportion between the two phases is determined by the lever rule. Since a given water chemical potential can correspond to a variety of compositions, the lipids have a degree of freedom to partition and redistribute along the water gradient. In the case of gradient formation in the relative DOPC:DPPC composition, the trajectory path along the water gradient would not follow the straight line in the phase diagram. This is schematically indicated by the red dashed line in Fig.

9. For this gradient line, the system would form an L_α phase in the higher water content regime and $L_\alpha + L_\beta$ phase coexistence at lower water content.

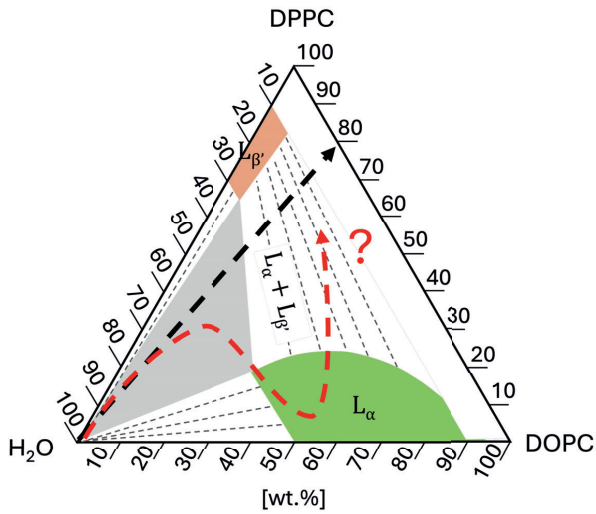

Figure 9. Ternary phase diagram of DOPC:DPPC:H_2O system serving as road map for tracking gradient formation in the vicinity of an air interface. The black dashed line show trajectory path where the DOPC:DPPC lipids preserve their initial composition along the water gradient. The red dashed line shows hypothetical gradient formation in the lipid composition along the water gradient.

3. System design and experimental consideration

The purpose of this chapter is to introduce the model systems that have been studied in this thesis work and to discuss how the scientific question has guided the system design and experimental approach, together with obstacles and considerations that arose. The basic concepts behind the key characterization techniques: confocal Raman- and fluorescence microscopy, X-ray scattering and ^{13}C polarization transfer solid-state NMR (PTssNMR) will also be described. The techniques that have been used in a standard manner will be covered.

3.1 Bioinspired model systems and experimental consideration

An important aspect of studying multicomponent lipid systems is to decipher the role of different components to understand how they influence each other, leading to the common features and phenomena. One way to approach this is to use simplified model systems that are designed to represent different aspects of the complex biological systems, and to formulate research questions that can be answered within certain frameworks. There is no pre-defined way or approach to compose a good model system, and there is always a trade-off between general principles and aiming for specific details. In this thesis work, the system design has been inspired by the composition of different biological membranes and human interfaces, namely the lung surfactant, tear lipid layer and stratum corneum (SC).

There is an abundance of different ways to model biological membranes and biointerfaces with respect to the composition and experimental approach. Biological membranes (inspired either by eukaryotic or bacterial membranes) can be designed with a focus on examining, for example, the antimicrobial properties of different compounds, drug penetration efficiency or protein-lipid interactions (121, 122). The

eukaryotic membranes are most commonly mimicked by using mixtures of PC phospholipids with smaller amounts of other phospholipids classes such as: PS, PE or cholesterol depending on the scientific question (121, 123). On the other hand, bacterial-like model membranes contain a higher content of negatively charged PG lipids in the phospholipoid mixture, which is more representative of the native composition (124, 125). Model membranes with more diverse lipid composition have also been used in research, for example trying to capture interbilayer asymmetry found in Gram-negative bacteria (126) and evaluating total bacterial membrane extracts (127). Similarly, different model systems have been used to mimic non-cellular biological lipid-rich interfaces such as the SC, lung surfactant and tear lipid film layer. In all cases, the complexity can range from a few lipids representing the main components up to the whole natural extracts (7, 15, 56). For example, the model systems of SC can use the intact tissue, or isolated components such as the extracellular lipids and corneocytes, or simplified lipid mixtures of few ceramides, free fatty acids and cholesterol representatives (55, 64, 69, 128-130). All these models have been used in the literature to either answer questions about the response of SC macroscopic properties to changes in external conditions, or more fundamental questions about the importance of certain lipid components in the formation of the SC lipid matrix structure, such as long periodicity phase (LPP).

In **Papers III and IV**, we used SC lipid extracts as well as intact SC and isolated corneocytes from an animal source (porcine ear skin) to answer questions about the phase behavior and response to changes in hydration and external stimuli. An important factor driving the selection of the model system besides the fundamental question, is the accessibility of the product and the desirable sample size for the experiments. The porcine skin shares molecular resemblance to human skin and is widely accepted as a skin model system in biomedical research, for example in transdermal drug delivery (131, 132) (133-135). Yet, a few differences in the crystalline packing of the lipids have been observed (8, 64). In this thesis work, the SC lipids are separated from the corneocytes rich matrix by extraction using a protocol involving several steps with mixed organic solvents (described in (55)). It has been shown (see SI section of **Paper III**) that the PTssNMR spectra of the intact SC layer can be reconstructed by the linear combination of the extracted SC lipids and the remaining corneocyte matrix. This confirms that the separation procedure does not lead to any detectable protein or lipid degradation or contamination.

Similar approaches can be used to model and evaluate the behavior of other biological membranes such as lung surfactants or the tear lipid film layer, where both natural extracts and simple model mixtures of a few lipid representatives can be studied. The

tear lipid film layer is usually modeled by mixing polar and non-polar lipid representatives, most commonly by mixing PC lipids with a smaller addition of PG, PE or free fatty acids, together with triolein and cholesteryl oleate (29, 136, 137). Accessing clinical extracts of tear lipid film is more demanding due to the scarcity of the product, the high risk of contamination and sample diversity that can put additional constrains on the reproducibility. In **Paper I and II**, simple model systems of a few lipid components are used to answer fundamental questions about the behavior of polar and non-polar lipids in a water gradient and how it translates to the behavior of biological membranes and drying interfaces. In **Paper I**, the behavior of liquid and solid lamellar phases is modeled by mixing DOPC:DPPC phospholipid in water, which is highly relevant for the understanding of lung surfactant behavior. In **Paper II**, the tear lipid film is modeled by mixing DOPC:DOPE lipids with an increasing amount of triolein in water, which captures the composition diversity of the natural layer.

3.2 Experimental approach and consideration

In an experimental laboratory setup, the behavior of model membranes is predominantly studied as dispersed lipid vesicles in bulk solution or as a monolayer or supported bilayer at the water-air interface in combination with different characterization techniques (121). One limitation of these model systems is that they do not capture (or resolve) what is happening beyond a simple monolayer or bilayer response in the cases of multilayered structures. Thus, forming a multilayer structure at the air interface can provide novel and important information for many multilayered biological interfaces and makes it possible to capture the behavior with respect to a water gradient. One main difficulty with studying lipid multilayer systems in non-equilibrium conditions is to control the boundary conditions so that the findings are reproducible. The response and adaptation of a system to external and internal stimuli may happen fast and not always in an intuitive manner. This puts additional demands on the spatial- and temporal resolution of the characterization techniques, as well as the requirement to resolve different molecular species. The need to keep the system in an open-air environment also limits the number of available characterization techniques.

To control experimental conditions in this thesis work (**Papers I - III**), a previously developed drying-cell setup for studies of lipid self-assembly in a water gradient is used (117). The setup is made of a ca 5 cm long glass capillary with a rectangular cross section (1 x 0.1 mm^2) connected to plastic cylinder that serves as a sample reservoir

(Fig. 9). The reservoir cap is pinched with a plastic tube to assure pressure equilibration in the systems. The aqueous lipid dispersion flows naturally towards the capillary tip where the less volatile solutes concentrate up in the opposite direction to the water gradient. The water gradient spans from almost fully hydrated bulk conditions (close to a_w = 1, which corresponds to 100% RH) to the surrounding air outside of the capillary tip maintained at controlled relative humidity (RH). The polar lipids can form different self-assembled structures at different positions in the water gradient, where the phase behavior is set by the local water chemical potential (see chapter 2.1.1). With time, the lipids continue to concentrate in the vicinity of the air interface, influencing the water gradient and naturally forming a thicker film and self-assembled phases.

For mixed phospholipid and surfactant systems, it has been shown that the thickness of the formed lipid phases scales linearly with the square root of time at the drying interface (118). This scaling behavior is crucial as it shows that the self-assembly phases can be grown larger at the capillary tip in order to reach the spatial resolution of the desired characterization techniques, without being compromised in their interfacial phase behavior within a certain time frame. Another advantage of the drying-cell setup is that it is easy and cheap to make, it can be placed and transferred between different environments (as in desiccators or ovens) and is compatible with "open-air" characterization techniques as long as the signal is not disturbed by the capillary glass. Furthermore, having the lipid film exposed to the ambient conditions also enables to study the multilayer response to more abrupt changes in the external environment as for example, abrupt exposure to water and partitioning of the molecules into the interfacial film. This has been done in **Papers II and III** by dipping the capillary tip into water and fluorophore solutions.

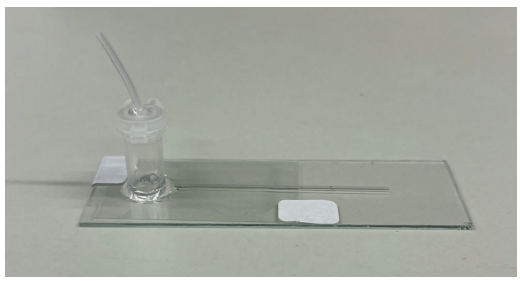

Figure 10. Image of the drying-cell setup sticked on top of a microscope slide for additional support. The setup is made of plastic cylinder glued to a small glass capillary cross on top of thin cover slide. The cylinder has a cap with small tube to ensure pressure equilibration in the system after closing. The lipid dispersion is added to the cylinder, which acts as reservoir, and the solution flows naturally towards the capillary tip. The multilayer lipid film is formed in the vicinity of the air interface at the capillary tip.

3.3 Main characterization techniques and methodology

In this work, a different and diverse range of characterization techniques have been used. This section aims to describe the key characterization techniques which have been used in the different projects and how they needed to be optimized for different scientific questions and the drying-cell setup. Confocal Raman microscopy was exclusively used in **Paper I** to quantitatively characterize the gradient between DOPC:DPPC:water components in the vicinity of the air interface. The Raman microscopy approach will be described in greater detail below. Confocal fluorescence microscopy was used in **Paper II** to image the distribution of different fluorescent probes between polar and non-polar lipid environments, and in **Paper III,** to image the penetration of a fluorophore into the SC lipid multilayer structure. In all **Papers (I-IV)** the structural characterization of lipid and corneocytes samples was done by either in-house small- and wide angle X-ray scattering (SAXS and WAXS) for bulk samples or synchrotron SAXS and WAXS for samples in a water gradient. The ^{13}C polarization transfer solid-state NMR (PTssNMR) was used in **Papers III-IV** to assess changes in molecular dynamics of different SC components after exposure to different stimuli.

3.3.1 Confocal Raman microscopy

Confocal microscopy refers to an optical technique in which a laser beam is focused to a point-like spot through an objective and the out-of-focus light is filtered away by a pinhole before reaching a CCD (Charge-Coupled Device) detector (138). This approach improves the contrast and spatial resolution of the technique significantly compared to conventional microscopy (139) and allows for 3D image reconstruction of the sample. The spatial resolution is limited by the wavelength of the light source and the numerical aperture (NA) of the objective (140). For optical lasers in a confocal setup the spatial resolution can go down to ca. 0.2 x 0.6 μm^2 depending on the objective and immersion medium (141). The temporal resolution is limited by the number of acquisitions, spectral averaging and scanning speed of the laser, all of which need to be optimized with respect to the signal output and heat damage to the sample (142, 143).

In confocal Raman microscopy, the Raman effect (inelastic scattering) from the sample is used to gather information about the electronic structure of the molecules in the confocal spot. Inelastic scattering refers to a process where the energy of the scattered photon is different from the incoming photon after interacting with the molecule. In Raman spectroscopy, this occurs when part of the incoming photon energy is used to excite the molecule to a higher vibrational state so that the scattered

photon leaves with lower energy (Stoke scattering). Only the vibrations which result in the fluctuation of the electron cloud polarizability of the molecule are Raman active (144). In Raman spectroscopy, a green laser ($\lambda = 532\ nm$) is commonly used as the excitation source. It provides strong Raman scattering with high sensitivity to different modes of vibrations, at the same time as being further away from electronic transitions which can in turn result in fluorescence and overpower the output signal. The Raman scattering from a sample is normally expressed in terms of the energy shift from the incoming photon and is given by the wavenumber as $\Delta\tilde{\nu} = \frac{1}{\lambda_0} - \frac{1}{\lambda_1}\ (cm^{-1})$, where each Raman peak corresponds to a different mode of atomic bond vibration. This makes this method one of the most sensitive to the electronic structure of the molecules, and a perfect candidate to resolve composition gradients across an interfacial layer (144, 145). Notably, the infrared spectroscopy methods, such as FTIR are highly sensitive to water vibrational modes, which can mask or dominate spectral features of lipids (146, 147).

The Raman peaks of various molecules are well characterized in the literature. The Raman spectrum of the water molecule is mainly composed of a broad continuous band ranging between 3100-3600 cm^{-1}, which corresponds to the symmetric (v_s) and asymmetric stretching (v_{as}) modes of the O-H bonds (148). While the magnitude of this band directly related to the water content, its shape depends on the local environment (149-151). Any quantitative assessment of the water content in a sample requires prior calibration to account for the non-linear behavior. In the literature, this has mainly been done by establishing a calibration curve that relates the actual water content (wt%) in the sample to the intensity ratio between the stretching vibration of the CH_2 groups (in the 2800-3000 cm^{-1} region) and the OH bonds (around 3400 cm^{-1}) to find a general relationship (152-155). In **Paper I**, the DOPC samples were equilibrated at different RH and water conditions, and the Raman signal of the water peak in the mixed samples was normalized to the integral of pure water. This enabled to make a calibration curve that directly relates the water peak integral to the water-DOPC ratio.

The Raman spectra of lipid molecules contain a large number of peaks spanning a wide range of Raman shifts. The majority of the peaks are attributed to different vibration modes of the hydrocarbon chains, as they often compose the largest structural component of the lipids. The Raman spectra of phospholipids can be roughly divided into three main regions: 1) the stretching vibration of the C-C bonds located between 1050-1200 cm^{-1}, 2) the twisting and scissoring vibrations modes of the CH_2 and CH_3 groups between 1400-1500 cm^{-1} and 3) the symmetric and asymmetric stretching

vibrations modes of the CH_2 and CH_3 groups between 2800-3000 cm^{-1} (156). For phospholipids, most of the Raman peaks overlap when there is no significant difference in the hydrocarbon chain structure. This makes the quantification of the relative composition in mixed lipid samples challenging. One way to estimate the lipid composition from the spectra, is to work with phospholipids that give rise to signature Raman peaks and to compare the peaks relative shape and intensities. This has been done for DOPC:DPPC mixtures by assessing the change in peak shapes as a function of composition (152, 157). In **Paper I**, the relative DOPC:DPPC composition was deduced from the spectra by fitting reference spectra of pure components in the spectral region that contains signature C=C peak (at 1657cm^{-1}) indicative of DOPC. The stretching vibrations in the highest spectral region 3) are sensitive to the trans-gauche (TG) or all-trans (AT) chain conformations, which are found in the L_α and L_β self-assembly structures, respectively (156). The spectral features in this region have previously been used to characterize the phase transition behavior of DMPC and DPPC vesicles in bulk conditions as a function of temperature (158, 159). The Raman features in the highest spectral region have been used to resolve TG or AT chain conformations behavior in the DOPC:DPPC mixtures (157).

Quantitative analysis of the gradient formation in mixed DOPC:DPPC:water systems at drying interface.

The spatially resolved confocal Raman microscopy combined with the drying-cell setup is used to estimate the composition gradients that are formed in the interfacial film layer. In order to perform quantitative analysis of the mixed lipid systems, the spectral features of the pure DOPC and DPPC films must be evaluated along the water gradient to find and select appropriate regions to perform the analysis. The experimental approach is schematically displayed in Fig. 11A for the interfacial DOPC film. The capillary edge is set to 0 and the Raman spectra are acquired along the water gradient as indicated by the color bar on top of the light microscopy image (Fig. 11B). The color ranges from red – close to the air interface, to blue – towards the hydrated bulk region in the capillary. The Raman spectra are later plotted on top of each other (Fig. 11C) and the spectral changes in the different Raman shift regions are evaluated. After comparing the spectra from DOPC and DPPC films, three spectral regions were selected for analysis. Region **A**: containing signature νC=C peak of DOPC for the quantitative composition analysis; region **B**: containing $\nu_s CH_{2/3}$ and $\nu_{as} CH_2$ modes for TG or AT chain conformations analysis; and region **C**: capturing vibrations of O-H for water content analysis. The zoom-in of these regions (**A-C**) for interfacial films made from DOPC, DPPC and mixed DOPC:DPPC $[20:80]_{wt\%}$ vesicle dispersions in water are attached in Fig. 12, together with the peak assignment. Optical microscopy images of the films are included in the SI section of **Paper I**.

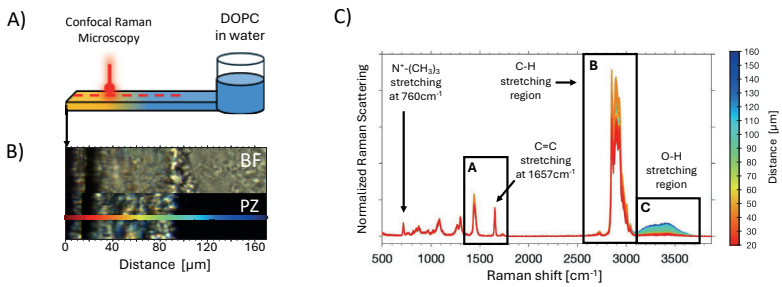

Figure 11. A) Schematic illustration of the Confocal Raman Microscopy characterization along the capillary axis. B) Optical (BF) and Polarized (PZ) light image of the DOPC multilayer film formed from a DOPC vesicle dispersion in water. C) Confocal Raman Spectra resolved along the capillary axis as indicated by the color bar. Region **A**, **B** and **C** are used for quantitative estimation of the composition gradient.

Spectral differences are observed for different vibrational modes in the lipid films along the water gradient. For example, when comparing the spectra of DOPC and DPPC films in region **A**, a stronger $\beta CH_{2/3}$ peak relative to the $\alpha CH_{2/3}$ is observed in the DPPC film, while the signature νC=C peak is only observed in the DOPC film. A clear difference in the peak shape and intensity is also observed in the spectral region **B**, where the stretching vibrations of the CH_2 groups are stronger in the DPPC film than in the DOPC film. The shape of the peaks is typical of what has previously been observed for TG hydrocarbon chain configurations in the L_α structure and AT hydrocarbon chain configurations in the L_β structure (156-159), which can be formed by pure DOPC and DPPC in water, respectively. In both systems, increasing water band integral is observed in region **C** as moving from air interface (red) towards more hydrated conditions (blue). For comparison, the lipid film made from mixed DOPC:DPPC is shown in the bottom panel, where spectral characteristics from both DOPC and DPPC systems can be identified. Interestingly, νC=C peak is only present in a certain region of the film facing more hydrated conditions (turquoise). The appearance of the νC=C peak is also associated with a change in the stretching vibration of the CH_2 (region **B**) to be more DOPC-like, while the remaining spectra are more DPPC-like.

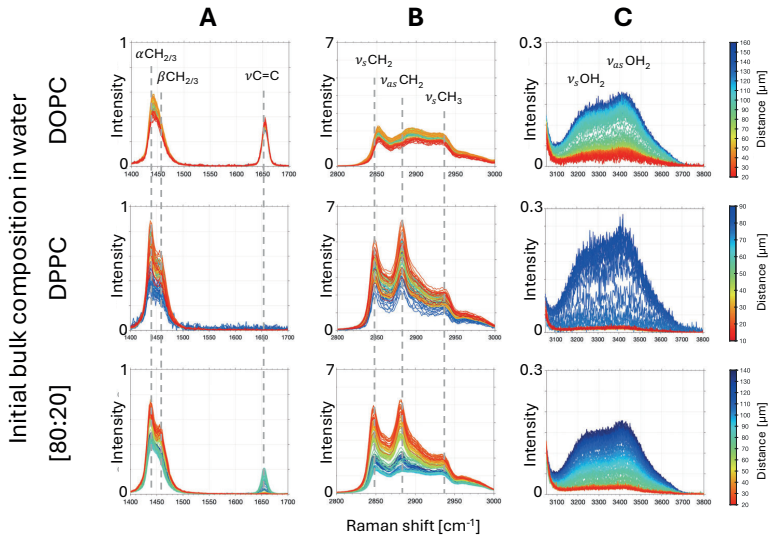

Figure 12. Zoom-in of region **A, B, C** in the confocal Raman spectra of multilayer films made from DOPC, DPPC and DOPC:DPPC [80:20] vesicle dispersions in the drying-cell setup respectively. Supplementary data can be found in Paper I. Spectral features in region A are used for estimation of relative DOPC:DPPC composition along the lipid film. Spectra feature in region B are used for analysis of hydrocarbon chain configuration and region B for estimation of the water gradient.

A two-step procedure is used in **Paper I** to quantify the composition gradients and phase transition in the interfacial lipid layer formed from mixed DOPC:DPPC vesicle dispersions. The first step involves the translation of the water peak integral (3100-3700 cm^{-1}) to the actual water content with the help of a calibration curve. The calibration curve is constructed by preparing DOPC samples with known water content, either by equilibrating a deposited lipid film at specific RH or by mixing the samples with known water compositions. The Raman spectra of the calibration samples are included in Fig. 13A. The water integral is then normalized to the integral of pure water (black) and plotted versus the water content in the lipid sample (wt% = water/(water + lipid)) to create a calibration curve shown in Fig. 13B. To evaluate whether the calibration curve can be applied to estimate the water content in DPPC and mixed DOPC:DPPC lipid film samples, the contribution of different components to the Raman spectra was investigated. All Raman spectra resolved along the water gradient for DOPC (purple) and DPPC (green) film are plotted on top of each other in Fig. 13C. In Fig. 13D, the lipid contribution to the spectra (integral under curve 600 – 3100cm^{-1} indicated by blue line) is plotted versus the water band contribution to the

spectra (3100 – 3800 cm^{-1} indicated by red line) for both systems. The integrals are linearly correlated and perfectly overlap for all DOPC and DPPC spectra along the water gradient (Fig. 13D). This means that the calibration curve shown in Fig. 13B can be used interchangeably between the two systems, and the DOPC:DPPC mixed samples to estimate the actual water profile.

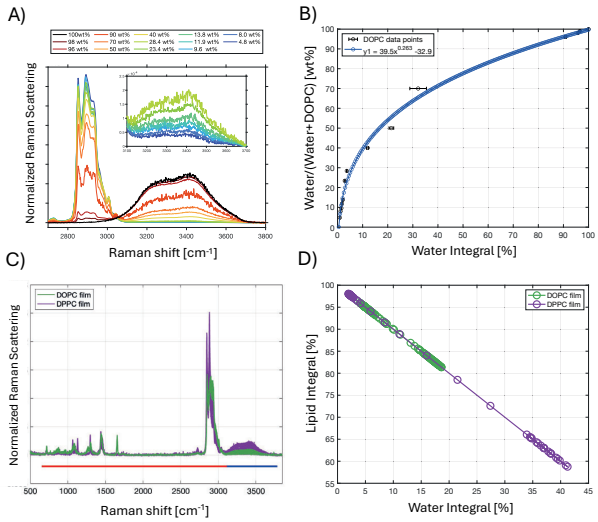

Figure 13. A)Calibration data of DOPC samples equilibrated at different water contents given in the legend. B) The extracted calibration curve to translate water peak integral to water content in the lipid film samples made in drying-cell setup. D) Raman spectra of DOPC (green) and DPPC (purple) multilayer films resolved along the water gradient. The red and blue line indicate the integration area for lipid and water respectively. D) Correlation between the lipid and water integral in the Raman spectra of DOPC and DPPC multilayer films in C.

The second step in quantifying the composition gradients formed along the interfacial lipid film is to translate the spectral behavior of the Raman peaks originating from the lipids to the relative DOPC:DPPC composition. The Raman spectra are first normalized to the C-N vibration found in the PC headgroup, which has previously been identified as insensitive to the lipid's phase behavior (160). To obtain the relative lipid composition, two reference spectra from DOPC and DPPC films at different hydration levels are selected and a linear least squares fitting of spectra with mixed lipid composition is performed in the spectral region covering the signature νC=C peak (region **A** in Fig. 12). The νC=C peak is virtually constant along the water gradient which makes it appropriate for the quantitative assessment of the DOPC content in the mixed lipid films. The fitting coefficient is translated to the relative DOPC:DPPC

weight composition and normalized to the estimated water content at each point by the calibration curve. The points are finally plotted in a ternary diagram to generate a quantitative composition trajectory path along the capillary axis. The analysis of the hydrocarbon chain phase (AT vs TG) is done by linearly fitting the DOPC and DPPC spectra (in L_α and $L_{\beta'}$ phase) in the Raman region sensitive to the conformation of the hydrocarbon chain (**B** in Fig. 12). The Raman microscopy studies are later supplemented by small- and wide angle Xray scattering mapping along the capillary axis, which is described in chapter 3.3.3.

3.3.2 Confocal fluorescence microscopy

In confocal fluorescence microscopy, a laser in the visible light range is used to excite fluorophores to a higher electronic state, which eventually re-emits photons with lower energy that are detected by a CCD camera. The excitation and emission wavelengths are strongly dependent on the fluorophore's electronic structure, where only certain electronic transitions are permitted (161). At room temperature, the fluorophore electrons are mostly present in their lowest energy state (S_0). When the incoming laser photon matches the energy gap between S_0 and a higher excited state (S1, S2, … Sn), light can be absorbed (Fig. 14A). The absorption occurs within a few femtoseconds and can excite the electron to any of the vibrational sublevels (v = 1, 2 … n) within the higher state. When the electron is in the higher vibrational state, it quickly relaxes to the lower vibrational ground sublevel (v = 0) in a non-radiative process (162). This process usually involves molecular collisions and the transfer of energy in the form of heat to the surrounding medium (163, 164). When the electron is in the lowest vibrational level of the excited state, it can undergo a slower photon-generating decay back to the ground state (S_0) as shown in Fig. 14A. The transition from the vibrational ground level of the excited S_1 state to any of the S_0 states can produce fluorescence, where the outgoing photons have a longer wavelength shifted by to the energy that was dissipated during the relaxation process. The shift of the re-emitted photons to the longer wavelength is referred to as the Stokes shift (shown in Fig. 14B), and it.is critical for the detection of the signal as it enables to block away wavelength of the incoming excitation light (162). Fluorophores with different electronic structures have different excitation wavelength, stoke shifts and emission wavelength which enables selective detection with multiple laser sources. In general, fluorophores can undergo several thousand of absorption-fluorescence cycles before becoming destructed, so-called photo-bleached (161, 165).

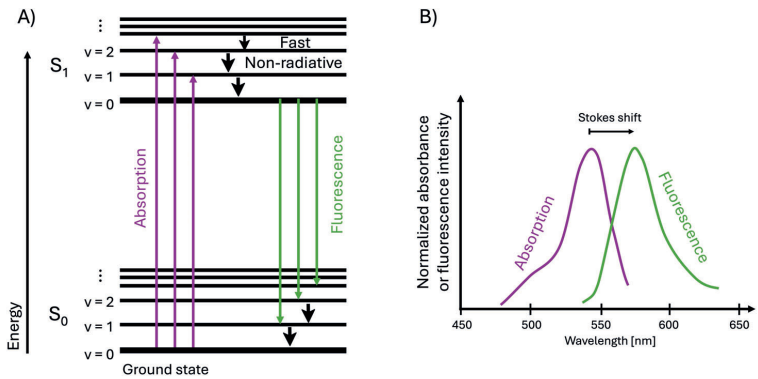

Figure 14. A) Jablonski diagram illustrating electronic states (S) tighter with the processes of absorption (purple) and emission of fluorescent photons (green) in molecular spectroscopy. The black arrows indicate non-radiative processes resulting in Stokes shift of the emitted photon. S_0 indicates the ground state, while v denotes vibrational sublevel. B) Typical absorption and emission spectra of a fluorophore.

Fluorophores can be classified into organic dyes, fluorescent proteins and inorganic probes, and the selection is guided by the scientific question (165). They can have a natural origin and be intrinsically fluorescent such as for example tryptophan amino acid, collagen, many porphyrin derivatives, flavins and NADH coenzymes. These have been used as indicators to study cellular processes and for example bacterial inactivation upon UV light exposure (166-168). Yet, the selectivity of naturally fluorescent components in biological samples limited, and in many cases, including the SC samples studied in this thesis, they contribute to background autofluorescence hindering detailed analysis (169). To circumvent the issue and improve selectivity, a multitude of fluorescent probes have been developed commercially and derivatized to shift their excitation and emission bandgaps to different wavelength regions and improving their photostability and fluorescent brightness. Additionally, the fluorescent probes have also been covalently conjugated to different chemical groups and linkers to improve their selectivity massively and their application in various research fields is countless. In this work, only organic dyes were used, and their usage will be described in greater detail, omitting fluorescent proteins and inorganic probes.

Organic dyes are small organic molecules, often rich in double bond conjugation in their structure (170). They can have slightly different physicochemical properties such as pH sensitivity, charge and hydrophobicity. For selective lipid staining, different fluorescent lipid analogs have been developed. The intrinsic properties of the dye molecule and its placement within the lipid structure is crucial. Lipids are amphiphilic

in their nature, with a hydrophilic headgroup and a hydrophobic hydrocarbon tail structure. The dye molecule can be covalently linked to either the headgroup or the chain, which leads to different perturbations. The properties of fluorescent lipid analogues are generally not representative of the corresponding native lipid species, as the addition of fluorescent groups typically leads to large increase in the lipid's molecular weight (up to twice the size). Instead, the partitioning of the fluorescent lipid analogues is used to probe differences between regions in a heterogenous sample (171). Several fluorescent probes can be used simultaneously as long as they do not overlap in their excitation-emission spectra (161, 165).

In **Paper II** of this thesis work, two chemically different fluorophores were used to distinguish between polar and non-polar lipid regions in mixed DOPC:DOPE:triolein lipid films. In this work, the polar region is probed by 18:0 Cyanine 5.5 PE (Cy5.5-DOPE) (Ex/Em 677/707 nm)[172] analog, while the presence of non-polar regions is probed by TopFluor-TG (Ex/Em 495/503 nm)[173]. Fig. 15 shows the chemical structure of the two dyes. The selection of these two dyes was guided by the initial composition of the lipid mixture in this research, the excitation/emission gap and commercial availability.

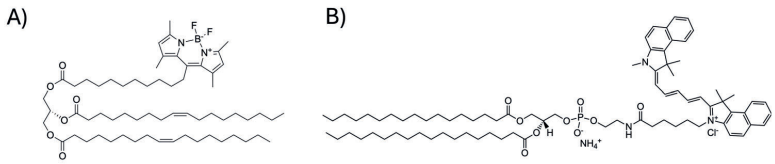

Figure 15. Chemical structure of A) TopFluor-TG and B) 18:0 Cyanine 5.5 PE.

In **Paper III,** the Rhodamine B free base fluorophore is used to image the penetration of hydrophobic molecule into the SC lipid film. To select a fluorophore, autofluorescence of the extracted SC lipids needs to be evaluated first for different lasers and emission filters. Fig. 16 shows the autofluorescence of a dry SC lipid film formed in the vicinity of an air interface in the drying-cell setup for two different lasers ($\lambda = 514$ nm and 543 nm) at the same laser power. The intensity of autofluorescence was among the lowest for the laser with $\lambda = 543$ nm. Rhodamine B free base has an excitation and emission maximum (Ex/Em) at 550/580 nm. Additionally, it is a stable and bright dye with moderate hydrophobicity (log P = 2) [174].

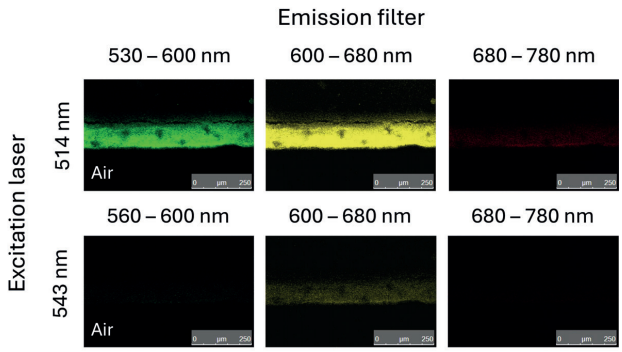

Figure 16. Confocal fluoresces microscopy of SC lipid film formed in the drying-cell. Images show autofluorescence in the sample at 514 nm and 543 nm captured with different emission filters.

3.3.3 X-ray scattering

X-rays are a type of high energy electromagnetic radiation with wavelengths between 0.01 and 10 nm (175). The X-ray scattering techniques rely on the interaction between the incoming X-ray photons and the variations in electron density within the sample. In the case of an elastic scattering event, the wavelength (or energy) of the scattered X-ray photon from the sample remains unchanged. The total electric field (E_{rad}) is equal to the superposition of all scattered waves, and the corresponding intensity ($I_{rad} = E_{rad}^2$) is detected by a 2D detector at a distance L from the sample over time (176, 177). This is schematically illustrated in Fig. 17. The resulting scattering pattern provides information about the size, shape, orientation, internal structure and heterogeneity within the sample.

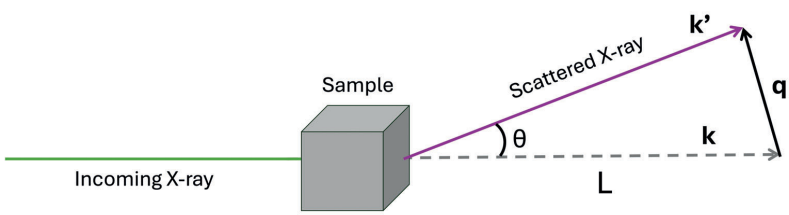

Figure 17. Schematic representation of typical scattering experiment. The incoming X-ray beam is scattered from the sample and scattering pattern at distance L are detected.

To extract the information, the scattering angle (Θ) is commonly translated to the so-called scattering vector q as:

$$q = |\mathbf{q}| = \frac{4\pi}{\lambda} \sin\left(\frac{\Theta}{2}\right) \quad (6)$$

Where λ is the wavelength, and $\boldsymbol{q} = \boldsymbol{k}' - \boldsymbol{k}$, where $\boldsymbol{k}$ and $\boldsymbol{k}'$ denote the wave vector of the incoming and scattered beam given by $k = \frac{2\pi}{\lambda}$, respectively (Fig. 17)(176). After radial integration of the detector image along the azimuthal axis (see Fig. 18) , a 1D scattering curve ($I_{rad}(q)$ vs q) can be achieved. The scattering curve can be further divided into three characteristic q-ranges as the regions provides different information about the sample. The low q-regime, also called 1) Guinier regime, provides information about the radius of gyration of the particles, followed by 2) the Porod regime, which provides information about the shape of the particles and 3) the diffraction regime, which gives information about the internal heterogeneity and structure within the particles, as well as interatomic distances (178). The analysis of the scattering patterns in this thesis work is limited to the diffraction regime.

In the diffraction regime, the scattering vector q is directly related to the real-space periodicity in the sample (d, also referred to as d-spacing or repeat distance), according to $q = \frac{2\pi}{d}$. The appearance of Bragg peaks at a given scattering angle Θ (or at given q, related by Eq. 6) is described by Bragg's law: $n\lambda = 2d \sin\left(\frac{\Theta}{2}\right)$ where n = 1, 2, 3… denotes the diffraction order. For a perfectly periodic crystal lattice, the Bragg peaks arise from the atomic planes with interplanar distance given by d_{hkl} (where h,k,l are the Miller indices). For periodic self-assembled structures, the Bragg peaks contain contributions form diffuse scattering due to the lattice fluctuations. Additionally, the Bragg-like peaks in the scattering pattern arise from the characteristic repeat distances of mesoscopic structures. The position of the first scattering peak corresponds to the lowest-order reflection from the periodic lattice and can be used to determine the characteristic repeat distance of the structure. The relative positions and intensity of the subsequent peaks are specific to symmetry and type of the self-assembled phase. The relative positions of the scattering peaks at q_n with respect to the fundamental peak at q_1 for lamellar, hexagonal, and bicontinuous cubic (double diamond) structure are displayed in Table 1.

Table 1. Peak position in scattering pattern relative to the lowest order reflection q_1 for different self-assembly structures.

Self-assembly structure	Ratio q_n / q_1
Lamellar	1 :2 : 3 : 4 : 5
Hexagonal	1 : √3 : 2 : √7 : 3
Cubic (double diamond)	√2 : √3 : 2 : √6 : √8

In the high q-regime (wide angle regime, referred to as WAXS), the scattering pattern probes distances corresponding to hydrocarbon chain arrangement (lateral packing) within the self-assembled structures. A hexagonal arrangement hydrocarbon chains, as found in solid lamellar structures such as L_β, gives rise to a sharp peak at approximately q = 15.3 nm^{-1} (d = 0.41 nm), whereas disordered hydrocarbon chains, as found in melted structures like L_α, display a broad feature in the same q-region.

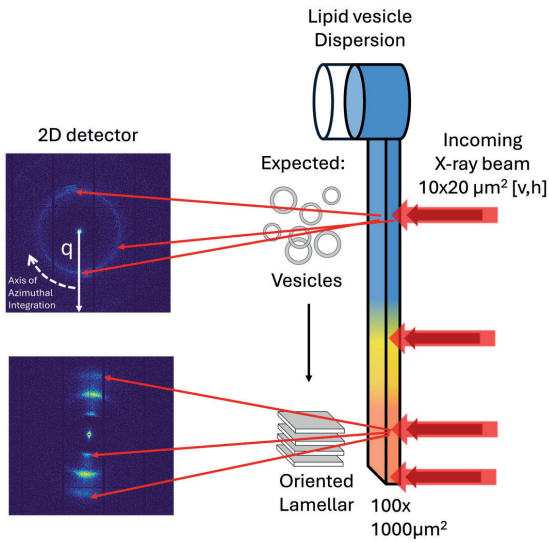

Figure 18. Schematic illustration of the synchrotron X-ray characterization of the multilayer lipid films formed in the drying-cell setup. The capillary is mounted vertically in the X-ray beam and scanned along the capillary axis. The lamellar structures close to the air interface display anisotropic scattering patterns which indicates preferential orientation with respect to the incoming beam. The lamellar structures stacks horizontally with respect to the air interface. The scattering vector q is indicted by solid arrow in the detector image, together with the axis of azimuthal integration (white dashed arrow).

In **Papers I-III**, a synchrotron X-ray source was used to determine the self-assembly structure formed along the water gradient in the drying-cell setup. The setup was mounted in the X-ray beam with spatial resolution of approximately 10x20 μm^2 and a scan was performed along the capillary axis, as schematically shown in the Fig. 18. The self-assembled structure in the interfacial multilayer films often arranges with respect to the air interface, producing oriented scattering patterns on the detector. The radially integrated scattering patterns can later put together to from 2D maps resolved along the capillary axis.

3.3.4 PTssNMR

To study molecular dynamics in SC samples, natural abundance of ^{13}C polarization transfer solid-state NMR (PTssNMR) was used. This method has previously been optimized by Nowacka and coworkers for self-assembled lipid systems (179) and later used to study the molecular mobility of SC components after various treatments (55, 65, 68, 180). PTssNMR is a combination of three individual experiments performed on the same sample in a sequential manner; cross-polarization (CP), insensitive nucleus enhanced by polarization transfer (INEPT) and direct polarization (DP), all performed under magic-angle spinning (MAS) with high-power proton decoupling technique. The PTssNMR acronym has been introduced to denote the usage of the CP-INEPT-DP set of measurements for analysis of the molecular mobility (179).

The CP and INEPT signals depend on the rotational correlation time τ_c which measures the rate of the C-H bond reorientation, and the absolute value of the order parameter $|S_{CH}|$, which provides information about the degree of anisotropy in C-H bond reorientation. The $|S_{CH}|$ values range from 0 for segments with isotropic reorientation to 1 for rigid and ordered lipid segments (181).

- In the **CP** experiment, the ^{13}C signal is enhanced by through-space dipolar coupling with neighbouring ^{1}H nuclei (182). For fast and isotropic C-H bond reorientation ($|S_{CH}| < 0.01$ and $\tau_c < 10$ ns), the CP polarization transfer averages to zero, while it is efficient for segments exhibiting slow ($\tau_c >$ 0.1 ms) and anisotropic motions (Fig. 19) (181).
- In the **INEPT** experiment, the ^{13}C signal is enhanced by through-bond scalar polarization transfer with covalently bound ^{1}H nuclei (182). Efficient INEPT transfer requires that the ^{1}H and ^{13}C transverse relaxation times (T_2) remain long compared to the time required for the ^{1}H-^{13}C polarization transfer (a few ms). For rigid molecules and/or those with highly anisotropic C-H bond reorientation ($|S_{CH}| > 0.5$ and $\tau_c < 0.1$ μs), the T_2 is short and does not

contribute significantly to the INEPT signal. On the other hand, the INEPT signal is enhanced in mobile segments (with $\tau_c < 10$ ns) because rapid molecular motions average out ^{1}H-^{1}H and ^{1}H-^{13}C dipolar interactions, leading to longer T_2 values for both ^{1}H and ^{13}C nuclei (Fig. 19)(181).

- In the **DP** experiment, the ^{13}C nuclei are directly excited by an RF pulse, and the appearance of the ^{13}C signal depends entirely on the longitudinal relaxation rate (T_1) of the nuclei (181). The spectrum displays resonances from all carbon atoms in the sample.

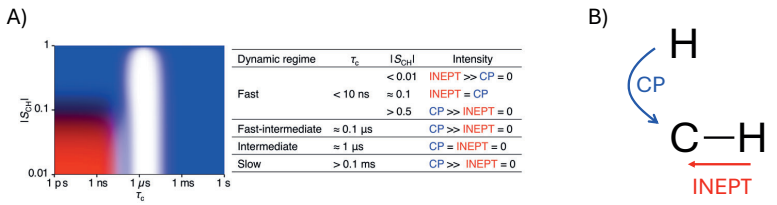

Figure 19. A) Signal enhancement in the PTssNMR experiment as a function of correlation time τ_c and absolute value of the order parameter $|S_{CH}|$. Adopted and modified from (68). B) Overview of peak enhancement during CP (blue) and INEPT (red) experiments in the PTssNMR.

For the evaluation of the segment mobility, the CP, INEPT and DP spectra are compared at the same chemical shift, where the DP spectrum serves as a reference spectrum. It is important to note that the INEPT signal is increased for both "fast isotropic" and "fast anisotropic" motions. In the latter case, the INEPT signal is accompanied by CP signal at the same chemical shift. (179, 181). The PTssNMR spectra of SC equilibrated at 97% RH together with peak assignment is shown in Fig 20. In **Papers III and IV**, the PTssNMR technique was used to study the change in the mobility of SC components as a response to different stimuli. In **Paper III**, changes in the mobility of extracted SC lipids is evaluated in dry and fully hydrated conditions in a stepwise temperature cycle (at 68°C, 45°C and 32°C). In **Paper IV**, changes in the mobility of SC components is evaluated at two different hydration levels (84% and 97% RH) after the exposure to UVB irradiation.

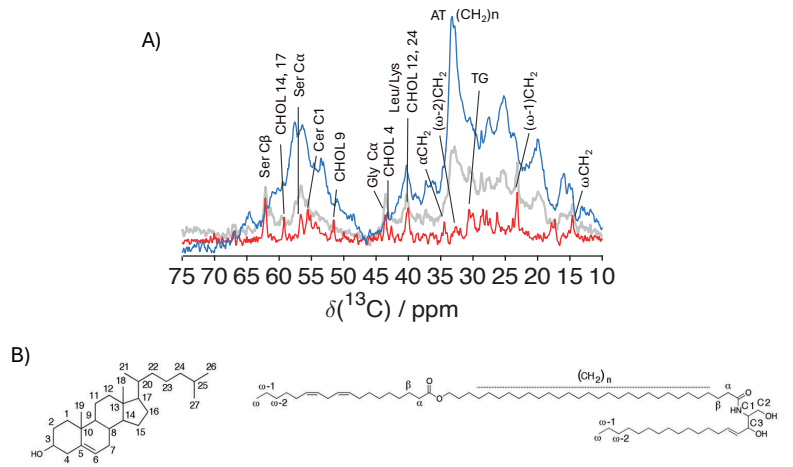

Figure 20. PTssNMR spectra of DP (gray), CP (blue), INEPT (red) experiment of SC equilibrated at 97% RH together with peak assignment. B) Chemical structure of cholesterol (left) and Ceramide lipid (right) with peak assignment.

4. Bioinspired model systems at drying interface

The purpose of this chapter is to summarize the main findings in **Papers I and II** of this thesis work. The lipid model systems in these papers were inspired by the biological interfaces (introduced in chapter 1) and the scientific questions were designed to answer fundamental questions about the behavior of polar and non-polar lipids in a water gradient.

4.1 Introduction to bioinspired model systems at drying interface

It has been observed that evaporation of water from multicomponent lipid mixtures can generate compositional gradients and spatial segregation of non-volatile components in the vicinity of an air interface (117, 183). Insights into the compositional and structural variations generated by the water gradient can be crucial for our understanding of biomembranes function which are in non-equilibrium conditions such as lung surfactant, tear film lipid layer (TFLL) and stratum corneum (SC). This work can also be directly translated to a wide range of technological processes, such as drying of the lipid formulations in food and pharmaceutical industries (116, 183-185).

Research in **Paper I** focuses on the question of whether a water gradient introduces other gradients in the phospholipid composition, and how it translates to the self-assembly structures formed at the drying interface. In this work, a model system of DOPC:DPPC in water was selected. The selection of the model system is inspired by the composition of eucaryotic membranes and clinical lung surfactants extracts commonly used in the replacement therapies (22, 121). The DOPC and DPPC are structurally similar with respect to the packing parameter (N_s) and differ only in the number of C=C bonds in the hydrocarbon chain, which makes them to self-assemble

into fluid L_α and solid $L_{\beta'}$ phase, respectively (94). The L_α and $L_{\beta'}$ also exhibit clearly different swelling behavior and water permeability due to their fluid and solid chain nature (186). These features can be further reinforced in the water gradient when the lipids are free to segregate. The lipid segregation can result in phase behavior that is not directly predicted from the initial bulk composition (25). In this work, we aim to examine how systems of mixed DOPC:DPPC lipids adapts to a water gradient and further influence the formation of self-assembly structures in the vicinity of the air interface.

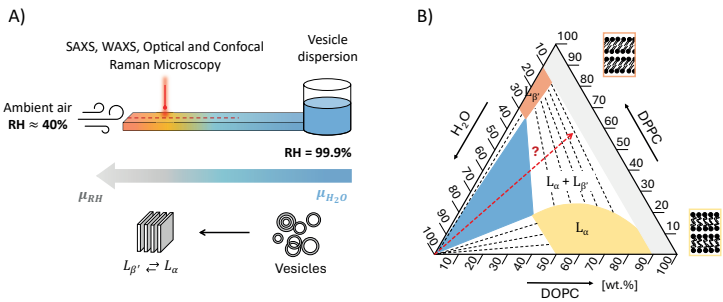

Figure 21. A) Schematic illustration of the unidirectional drying-cell setup. The reservoir is filled with an aqueous vesicle dispersion, which flows naturally towards the capillary tip that is exposed to ambient air. Thus, the phospholipid mixture is placed in a water chemical potential gradient between the reservoir (RH = 99.9%) and the air with lower RH. As the hydration gradient develops, the phospholipids accumulate in the vicinity of the air liquid interface, forming multilamellar structures. B) Equilibrium phase diagram of the DOPC:DPPC:H_2O mixture at 25°C (data included in SI section of paper I). At all relevant water contents, DOPC forms a liquid crystalline phase (L_α) with fluid hydrocarbon chains, while DPPC forms a lamellar gel phase ($L_{\beta'}$). In addition to the two single-phase regions, the phase diagram is dominated by two-phase coexistence region (white, with dotted black tie-lines) and a three-phase triangle (blue). The red dashed arrow indicates a trajectory the system would follow if DOPC:DPPC ratio of the bulk was preserved along the hydration gradient.

To approach this, multilayer lipid films are formed from DOPC:DPPC vesicle dispersion with varying initial lipid composition in the drying-cell setup (previously introduced in chapter 3.2). A characterization approach based on the spatially resolved confocal Raman microscopy and small- and wide angle X-ray scattering (SAXS and WAXS) mapping of the multilayer lipid films along the water gradient was developed as described in chapter 3. The composition gradient is traced quantitatively and related to the self-assembly structures formed in the vicinity of an air interface. The experimental approach and the ideas behind the main research question in **Paper I** are schematically outlined in Fig. 20. In the absence of lipid segregation, the proportion between the DOPC:DPPC lipids in the water gradient would be the same as the initial composition and the self-assembly phase in the interfacial multilayer lipid film would

follow the trajectory along the straight line (indicated by a dashed red arrow) in the ternary phase diagram when approaching the dry interface. Any deviation in the lipid composition from the initial bulk proportions along the water gradient would appear as a deviation from this line. The trajectory can be governed either by the free energy minimization of the system (thermodynamics) by transport properties of the components (kinetics), or both. This work aims to understand the driving force behind the lipid segregation in the water gradient.

Research in **Paper II** focuses on how the polar and non-polar lipids segregate in a water gradient when they are exposed to an air interface. In this work, the model systems are composed of DOPC:DOPE mixtures with increasing amount of triolein. Depending on the amount of triolein in the system, the initial bulk structure can vary from lipid vesicles to stabilized emulsions droplets in water (187, 188). The DOPE is structurally different from the DOPC and promotes the formation of nonplanar self-assembly structures (see Fig. 5 in chapter 2) (94). The main idea behind the project is schematically illustrated in Fig. 22. When the vesicles or droplets approach an air interface, they may fuse, coalesce and phase separate within the water gradient. The system design was inspired by the composition of the tear lipid layer (TFLL), and clinical formulations used for treatment of various eye related conditions, which are expected to behave in similar way at the eye interface (43, 44).

To study the interfacial behavior of the TFLL model systems, the same characterization approach based on the drying-cell setup is used (introduced in chapter 3). The Raman signal of unsaturated lipids strongly overlaps without any signature peaks, disabling the quantitative analysis described in chapter 3.3.1. Instead, segregation between regions rich in polar and non-polar lipids was captured by tracing the partitioning of different fluorescent probes in the vicinity of the air interface. The DOPC and DOPE lipids have the same hydrocarbon chains, but they are structurally different with respect to their headgroups. The DOPC forms a lamellar structure, while the DOPE with its smaller PE headgroup, promotes the formation of nonlamellar structures as for example inverted hexagonal and cubic phases (94). Due to these differences, successive addition of the DOPE to the DOPC or DOPC:triolein mixtures can have pronounced effects on the interfacial behavior of the system. For example, it may contribute to the formation of more diverse self-assembly structures or promote phase separation and tubule formation (Fig. 22). In this work, we aim to determine how the initial lipid composition affects the structural organization of the interfacial film and how the hydration gradient influences the segregation of polar and non-polar lipids close to the water-air interface.

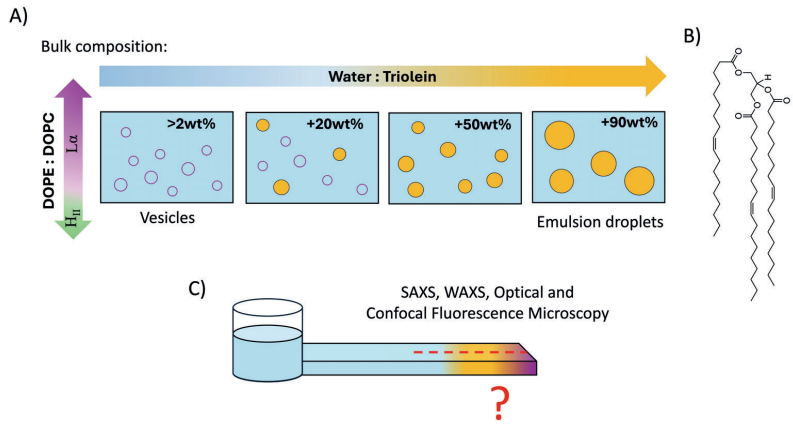

Figure 22. Schematic illustration of the idea behind research done in Paper II. A) The model system is composed of varying bulk composition of DOPC:DOPE:triolein in water. Due to the different nature of the lipids, the bulk structure can vary from dispersed lipid vesicles (purple circle) to stabilized emulsion droplet (orange). B) Chemical structure of triolein. C) The lipid dispersion is added to the drying-cell setup and flows naturally to the capillary tip facing air. The interfacial behavior is characterized by the means of SAXS, WAXS and confocal fluorescence microscopy.

4.2 Partitioning of phospholipid in the water gradient

This subchapter summarizes the data from **Papers I and II**, with aims to answer the following set of questions:

- Does the water gradient introduce a gradient in the phospholipid composition?
- How do these gradients influence the self-assembly behavior in the vicinity of an air interface?

4.1.1 Phospholipids with different chain composition

A multi-technique characterization approach combined with the drying-cell setup was used to study the partitioning of DOPC and DPPC lipids along the water gradient. Fig. 23 summarizes the composition and phase characterization of the interfacial multilayer formed from DOPC:DPPC vesicle dispersion with initial $[10{:}90]_{wt\%}$ composition in

water. Formation of two distinct birefringent regions is observed close to the capillary tip facing air (Fig. 23A). The analysis based on spatially resolved confocal Raman microscopy (described in chapter 3.3.1) shows that the water content is low (<20wt%) in the interfacial layer. The water content increases sharply when moving along the capillary axis from the air interface towards bulk solution (Fig. 23B). Notably, strong enrichment in DOPC (up to an $[80:20]_{wt\%}$ DOPC:DPPC composition) is observed at intermediate and high hydration levels, which is balanced out by a strong depletion in DOPC (down to $[10:90]_{wt\%}$) in the driest part of the interfacial film (Fig. 23C). The data on lipid composition and water composition are combined into a ternary composition path and plotted on top of the phase diagram of the system in Fig. 23F. It is concluded that the DOPC and DPPC lipids strongly segregate along the water gradient, and they do not preserve their initial bulk composition, which would otherwise follow the dashed grey arrow in Fig. 23F.

Further analysis of the hydrocarbon chain conformation reveals that the enrichment in DOPC is associated with trans-gauche (TG) chain conformation, which is indicative of the DOPC-rich L_α phase. In the DPPC-enriched parts of the film facing air, on the other hand, the hydrocarbon chains are present in all-trans (AT) conformation, indicative of an $L_{\beta'}$ phase. At intermediate DOPC:DPPC compositions both TG and AT conformation are detected. Spatially resolved synchrotron SAXS and WAXS were used to directly characterize the mesostructures along the capillary axis. The SAXS spectra are combined into a 2D map and displayed in Fig. 23D. Evenly distributed sharp peaks with decreasing intensity characteristic for a lamellar structure, are observed spanning the driest part of the interfacial film in the vicinity of the air interface. When moving towards more hydrated regions of the film along the capillary axis, the appearance of an additional set of sharp peaks with similar intensity characteristic is observed. This pattern indicates lamellar-phase coexistence. Taken together, the structural analysis reveals segregation of single phases at different positions in the water gradient, instead of phase coexistence along the whole film which would be predicted by the initial bulk composition over the same range of water contents.

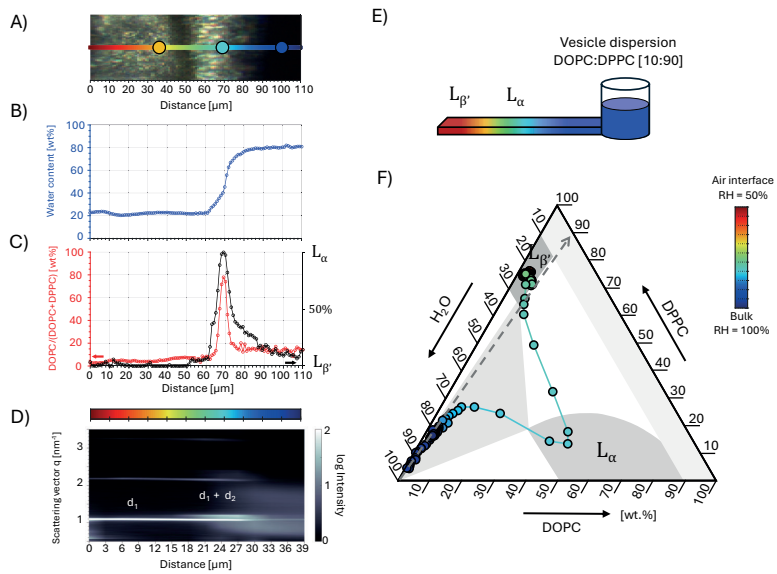

Figure 23. Monitoring composition and structural gradients in a hydration gradient for a lipid mixture composed of phospholipids in water ([10:90]$_{wt\%}$ DOPC:DPPC). The hydration boundary at the interface exposed to air is defined by the relative humidity, which is 50% RH here. A) Optical microscopy image of the sample in between crossed polarizers, showing the formation of birefringent structures. B) Raman confocal microscopy measurements of the water gradient along the capillary axis, obtained by comparing νOH vibrations (water) to νCH$_2$ and ν_sCH$_3$ (all phospholipids) vibrations. C) Confocal Raman microscopy measurements of the variation of the DOPC:DPPC proportions along the hydration gradient (red dots), obtained by comparing νC=C vibrations (DOPC) with νCH$_2$ and ν_sCH$_3$ (all phospholipids) vibrations, revealing a sharp self-segregation of the two phospholipids. A finer analysis of the νCH$_2$ and ν_sCH$_3$ vibrations provides insights into lipid chain conformation (TG and AT), indicative of the L_α and $L_{\beta'}$ phases, respectively (black dots). D) Small angle X-ray scattering (SAXS) map showing the scattering intensity at different scattering vectors q along the hydration gradient. Sharp structural peaks (white lines) are observed, indicating the formation of lamellar phases with equidistant repeats. F) Composition trajectory derived from B) and C) plotted on top of the equilibrium phase diagram. Phospholipid self-partitioning corresponds to a serpentine trajectory rather than following a diagonal at a constant DOPC:DPPC ratio. E) Schematic illustration of the drying-cell showing the phase characterization of the formed multilayer films.

The same experimental approach was used to characterize the interfacial lipid films formed from DOPC:DPPC systems with $[20:80]_{wt\%}$ and $[70:30]_{wt\%}$ initial lipid compositions. For both systems, preferential lipid segregation along the water gradient is observed. The DPPC lipid accumulates in the lowest water content regime in the vicinity of the air interface, resulting in the formation of the $L_{\beta'}$ structure, while DOPC segregates to the higher water content regimes and forms L_α structure. On the other hand, when the initial composition of DPPC was below the solubility limit of the L_α phase, the interfacial lipid film formed coexisting $L_\alpha + L_{\beta'}$ phase in the vicinity of the air interface. The results are summarized in Fig. 24.

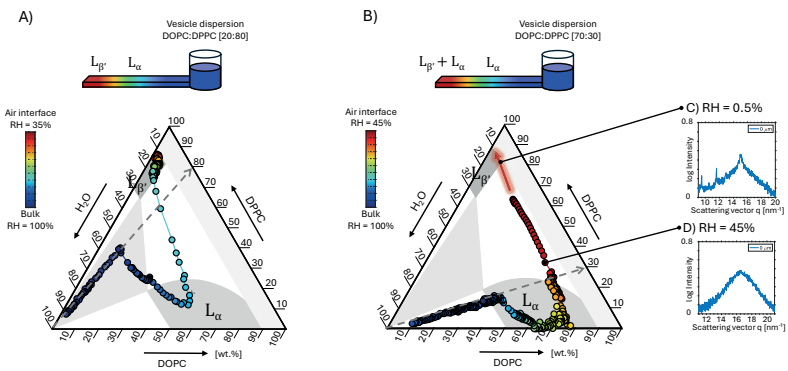

Figure 24. Characterization of the multilayer film formed in a drying-cell setup from a lipid dispersion with initial A) $[20:80]_{wt\%}$, B) $[70:30]_{wt\%}$ DOPC:DPPC composition in water. The composition trajectories are plotted on top of the phase diagram where the color-bar indicates the distance from the air interface. Optical images of the films are included in the SI section of Paper I. For both systems, a clear gradient formation in the lipid composition deviating from the initial bulk composition (indicated by the gray arrow) is formed along the water gradient. The DOPC is always enriching in the more hydrated regions of the interfacial films, while the DPPC content always increases towards the drier regions of the films. The results are graphically represented above the phase diagrams. The WAXS spectra of the lipid film exposed to two different relative humidities C) 0.5% and D) 45% at the capillary tip.

We further evaluated the response of the interfacial lipid film made from $[70:30]_{wt\%}$ DOPC:DPPC to the change in external relative humidity conditions. A stream of N_2 gas (RH ≈ 0.5%) was blown on the capillary tip with coexisting $L_\alpha + L_{\beta'}$ phases. The SAXS and WAXS characterization revealed that the lipid film is responsive, and the interfacial layer can be pushed to form single $L_{\beta'}$ phase by lowering the external RH. This is schematically illustrated by a red arrow in Fig. 24B. These results showcase the sensitivity of the lipid phase behavior at the drying interface with respect to the

external conditions, and that the structural response can be tuned by the relative composition of the lipids in the system. How easily the system phase-separates or phase-coexists depends on how close the initial lipid composition is to the phase boundaries. This observation is highly relevant and directly translatable to our understanding of how the biological interfaces may tune their physicochemical properties at the drying interface.

Free energy gain

Having established the compositional and structural trajectories in the phase diagram for a set of different conditions, we next evaluate what could be the driving force for the lipid segregation in the water gradient. A two-state system is employed where the $L_{\beta'}$ phase with mixed lipid composition are assumed to behave the same as the $L_{\beta'}$ phase made of pure DPPC, and the mixed composition L_{α} phases behaves as the pure DOPC L_{α} phase. We analyse the contribution to the free energy from the interlamellar interactions in the two phases along the water gradient. For a lamellar phase, this free energy contribution can be obtained from the interlamellar force per area (Eq. 3 in chapter 2.1.1), integrated over the interbilayer separation, which can in turn be related to the water content. In **Paper I**, the interbilayer separation for L_{α} and $L_{\beta'}$ phases are directly obtained from the water content at each point along the gradient, and the contribution to the total free energy is calculated by estimating the relative amount of each phase by using the level rule. The calculation is done both for the straight line that preserves the initial DOPC:DPPC ratio constant along the water gradient, and for the actual serpentine trajectory line from the experimental characterization where the ratio between the two lipids changes. As an example, the calculation is done for the gradient formed in a $[80{:}20]_{wt\%}$ DOPC:DPPC lipid system and summarised in Fig. 23A. The difference in free energy between the linear and experimental serpentine path along the water gradient is shown in Fig. 25. We conclude that there is a large gain in free energy when forming the $L_{\beta'}$ structure with shorter-range repulsion in the low hydration regime. This result agrees with the observed phase segregation in the mixed DOPC:DPPC lipid systems, where the $L_{\beta'}$ phase is preferentially formed in the regions facing drier conditions. This result showcases that the self-assembly structure with the lower water permeability forms naturally at the air interface as a response to drier conditions.

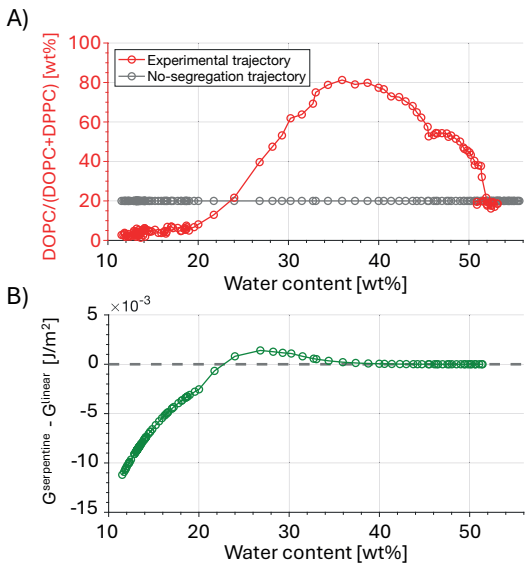

Figure 25. A) Lipid composition gradient (red, experimental trajectory) along the water gradient (x-axis) in the lipid multilayer film from a $[20:80]_{wt\%}$ DOPC:DPPC vesicle dispersion. The hypothetical linear path preserving the initial lipid composition is indicated in gray. The water content is translated to the interlamellar spacing, h_L for each phase L_α and $L_{\beta'}$ (see table S4 in Paper I), and the variation in free energy is plotted in B). Depletion of DOPC from the driest part of the hydration gradient leads to a large free energy gain ($G^{serpentine} - G^{linear} << 0$), while the accumulation of DOPC at intermediate hydration leads to a small free energy loss. The total free energy confirms that self-segregation and phase separation are favorable and spontaneous.

4.2.2 Phospholipids with different headgroups

The phase behavior of interfacial lipid films formed from DOPC:DOPE lipid systems at the drying interface was evaluated in **Paper II.** In this system, DOPC and DOPE molecules have the same hydrocarbon chains, but they differ with respect to their headgroups (Fig. 5). The DOPE lipid is known to promote formation of non-planar self-assembly structures such as inverse hexagonal phase. For this reason, lipid segregation in these systems can have a strong effect on the interfacial phase formation along the water gradient. Since the two lipids have the same hydrocarbon chains, their Raman spectra strongly overlap, and the quantitative composition analysis cannot be performed. In this case, the SAXS characterization of the interfacial films is performed and compared to the phase behavior of the pure lipid systems and the literature studies.

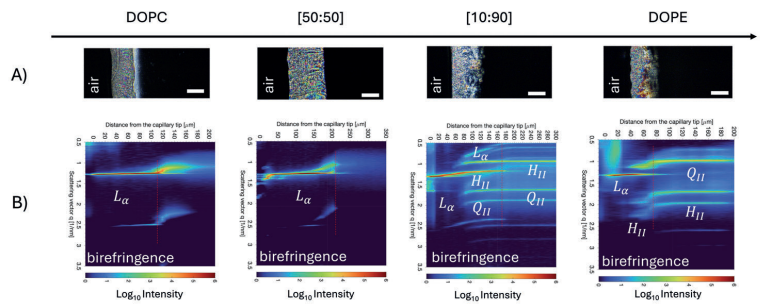

Figure 26. A) Polarized light optical images of interfacial multilayer lipid films formed from DOPC:DOPE vesicle dispersions with varying molar ratio in water. The white bar in the images corresponds to 100 µm. B) The SAXS characterization of the multilayer films along the capillary axis together with the phase assignment. The 0 is placed at the air interface and the vertical red line indicates approximate end-position of the birefringence observed in the optical images.

Fig. 26 summarizes the interfacial behavior of DOPC:DOPE lipid systems characterized in the drying-cell setup exposed to ca. 60% RH at the capillary tip. For DOPC:DOPE systems with initial $[50:50]_{wt\%}$ composition, the formation of a single L_α phase was observed along the water gradient. This behavior is not predicted by the bulk phase studies, which show the presence of inverse hexagonal (H_{II}) and cubic phases forming at reduced hydration for the same lipid mixtures (189). This result indicates that DOPC and DOPE undergo segregation in the water gradient where the DOPC lipid accumulates in the drier regions. On the other hand, a much richer phase behavior is observed in the lipid film formed from an initial $[10:90]_{wt\%}$ DOPC:DOPE composition where the amount of DOPC is low. Similarly, formation of a single L_α

phase facing the air interface is observed together with H_{II} and cubic phases in the water gradient. Both H_{II} and Q_{II} phase display changes in lamellar repeat distance along the water gradient. As the interfacial layers formed in the systems enriched with the more hydrophobic DOPE are typically thin, it is difficult to experimentally resolve which of the interfacial phases are present at each position. For the DOPE-water system, formation of a single L_α phase is followed by what appears as L_α + H_{II} phase coexistence, and then H_{II} and Q_{II} coexistence along the water gradient facing bulk. These observations of two-phase coexistence in the binary DOPE-system are inconsistent with local equilibrium along a hydration gradient, since two phases coexist only at a single water chemical potential. The observation of coexistence likely reflects the limited spatial resolution in the SAXS experiments, where each measurement point (spectrum) covers a broader range of water activities.

4.2 Segregation of polar and non-polar lipids at drying interface

This subchapter summarizes the data from **Paper II,** aiming to answer the following set of questions:

- How are the polar and non-polar lipid mixtures structuring at the drying interface?
- Can the observed phenomena be related to the properties of the tear lipid layer?

The interfacial behavior of DOPC system with an increasing amount of non-polar triolein was characterized in the drying-cell setup. For all systems examined (DOPC with up to 90wt% triolein in bulk – from vesicles to oil droplets; see SI section in **Paper II**) the formation of a birefringent layer in the vicinity of the air interface is observed (Fig. 27A). The SAXS mapping of the layers, confirms presence of an L_α phase which is indicated by evenly distributed sharp peaks (Fig. 27B). Peak broadening is observed with increasing triolein content. By studying the partitioning of different fluorophores (Cy5.5-DOPE lipid analogue and TopFluor-TG, Fig. 15) between the different regions using confocal fluorescent microscopy, it is revealed that the more hydrophobic triolein-rich phase (green) is wetting both sides of the phospholipid-rich lamellar phase (red). This result shows that the polar and non-polar lipids phase-segregates into heterogeneous layers in the vicinity of the air interface already at very low contents of nonpolar lipid.

The findings of strong segregation between phospholipid-rich lamellar regions and isotropic triolein domains in a water gradient support previously proposed models of TFLL organization, which suggest a multilayered structure composed of a thin polar phospholipid layer adjacent to the aqueous tear liquid, covered by a thicker nonpolar lipid phase at the air interface (35-37). The observation that triolein preferentially wets the lamellar phase may have important implications. A low interfacial free energy between nonpolar lipids secreted from the eyelid glands and the existing tear film lipid layer likely facilitates the rapid spreading of a continuous, nonpolar film during blinking. The favourable spreading of nonpolar lipids on the TFLL may also enhance mechanical stability under shear, helping to preserve its integrity while maintaining ocular surface lubrication (7, 29, 30).

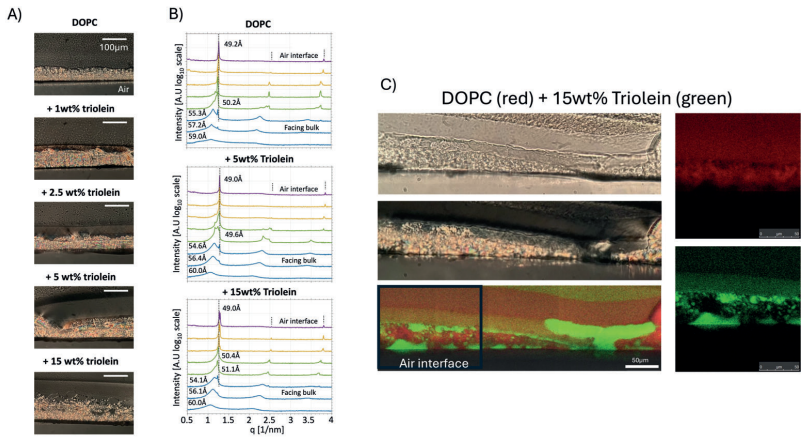

Figure 27. A) The interfacial layer formed from different DOPC-triolein compositions observed through optical microscopy with cross polarizers. The white bar corresponds to 100 µm and applies to all optical images in A. B) Azimuthally integrated SAXS spectra obtained at different positions in the hydration gradient along the capillary axis. The color coding: purple (facing air), fused layer (yellow), transition region between fused and unfused layer (green) and unfused layer (blue) facing bulk. Dotted lines indicate equidistant Bragg reflections from the lamellar phase in the driest part of the interfacial layer. C) Confocal microscopy images of the distribution of Cy5.5-DOPE (red) TopFluor-TG (green) within the interfacial layer. The interfacial films were formed and characterized at T ≈23 °C and RH ≈ 45%.

One key functional role of the TFLL is to prevent evaporation of the tear fluid (26, 190-192). Incomplete tear lipid films have been associated with dry eye disease and tear hyperosmolarity (193, 194). Importantly, the phospholipid lamellar structure introduces functional properties that are not captured by the single phospholipid monolayers used in most previous TFLL model studies (136, 195, 196). Both the oriented lamellar phase and the overlying oil layer act as effective barriers to water evaporation. In terms of protection against external chemicals, the oriented lamellar phase restricts diffusional transport of both hydrophilic and hydrophobic substances, analogous to the multilamellar lipid matrix of the stratum corneum in the skin (197, 198). In contrast, the hydrophobic nonpolar lipid layer and the single phospholipid monolayer do not significantly limit the diffusional transport of hydrophobic compounds. Taken together, the two-layer TFLL oil–lamellar arrangement fulfils multiple functions, including spreading, lubrication, evaporation control, and protection against environmental agents.

As a next step, DOPE was added to the DOPC:triolein bulk mixtures. Similar to the DOPC:triolein system, a birefringent layer with an L_α structure is formed close to the air interface (SAXS characterization in the SI section of **Paper II**). In addition, the systems display tubulation phenomena stretching from the interfacial lipid layer towards the bulk solution (Fig. 28). The tubules are thinner and able to extend further out for the systems with an increasing amount of DOPE. Over time, the tubules collapse back onto the multilayer interfacial layer to form a thicker film close to the air interface. The collapse of the tubules is slow (over several days) and tends to squeeze the triolein-rich domains towards both the interfacial and hydrated sides of the phospholipid-rich film (Fig. 29).

The balance between phospholipid components in the TFLL can have important functional consequences. In the tear film, PE levels are well below the threshold required to form non-lamellar phases (Fig. 25). Maintaining oriented lamellar structures across the full hydration gradient provides an effective barrier to the diffusional transport of both hydrophilic and hydrophobic compounds. The tubulation process, in which bilayer structures migrate against the osmotic gradient, may have functional consequences by facilitating the transport of hydrophobic species across the aqueous tear layer. Tubulation may also provide a mechanism for redistributing material within the lipid layer, potentially contributing to layer stability and uniformity.

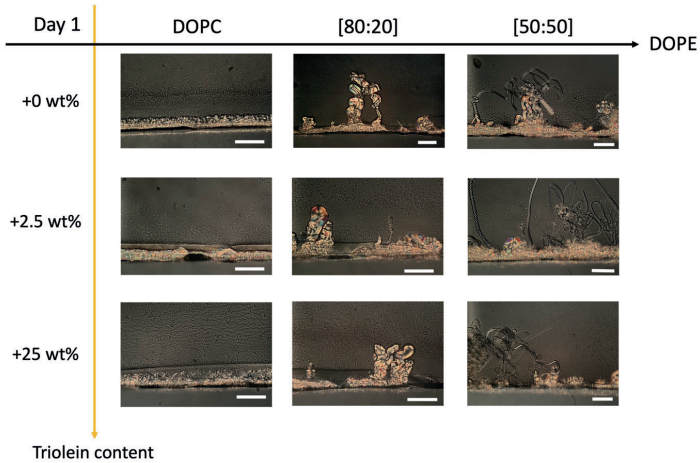

Figure 28. Interfacial layers formed for different DOPC:DOPE:triolein compositions observed through optical microscopy with cross polarizers at T ≈ 23 °C and RH ≈ 45%. The white bar in the images corresponds to 100 µm. Tubulation phenomena extending towards bulk is observed at the air interface in systems containing DOPE.

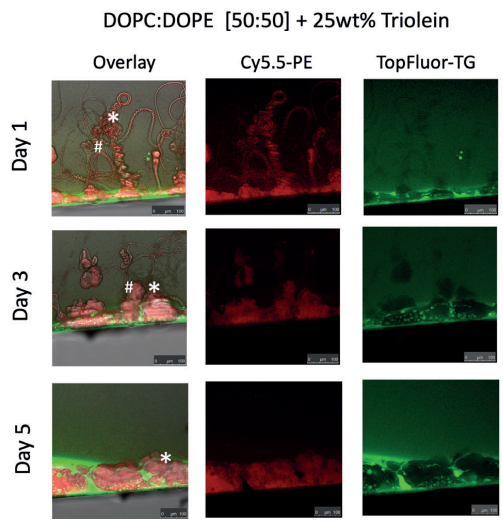

Figure 29. Evolution of interfacial layers formed from DOPC:DOPE $[50:50]_{wt\%}$ + 25wt% triolein compositions observed through confocal fluorescence microscope. Distribution of Cy5.5-DOPE (red) and TopFluor-TG (green) is observed in different region of the film. The * and # symbols indicate the collapse of a tubule and formation of larger triolein-rich domains, respectively.

We further evaluated how the phase-separated lipid layer (formed from DOPC:DOPE $[50:50]_{wt\%}$ with 25 wt% triolein) responds to the instantaneous change in the hydration level from the previously dry outside environment. The capillary tip was dipped into a water droplet, and the behavior of the phase-segregated lipid layer was imaged by polarized optical- and fluorescence microscopy (Fig. 30). When soaked in water, instantaneous formation of tubules towards the water droplet was observed. Furthermore, the triolein-rich domains (appearing as green) were squeezed into oil droplets at the phospholipid-water interface and prevented tubulation from occurring in the same region. These observations provide valuable insights into the behavior of mixed polar and non-polar lipid layers at the water-air interface. The non-polar lipid layer seems to coat and stabilize the phospholipid-rich structure, which is dynamically more responsive to environmental changes (as observed in Fig. 29). This may provide useful information about the protective role of the non-polar lipid layers, such as the one found in the TFLL, in preventing structural deformation under abrupt changes in the level of hydration, for example as in tearing.

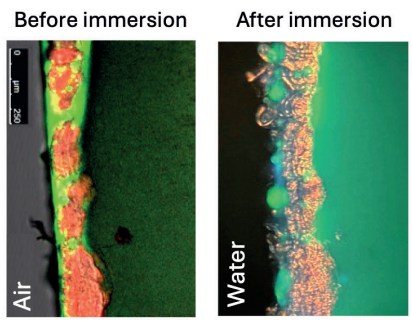

Figure 30. A) Confocal fluorescence microscopy and image of the interfacial lipid film formed from DOPC:DOPE $[50:50]_{wt\%}$ + 25 wt% triolein. Distribution of Cy5.5-DOPE (red) and TopFluor-TG (green) is observed in different region of the film. B) Optical microscopy images under cross polarized light overlaid with fluorescence filter of the same lipid film immersed in a water droplet. Color contrast in the images is enhanced.

4.3 Conclusion and outlook

In **Papers I and II**, the interfacial behavior of polar (phospholipids) and non-polar lipid mixtures was evaluated with the aim of provide further understanding of biological interfaces, such as lung surfactant layer and TFLL. As the combination of different polar and non-polar lipids can be endless, one needs to think about an interesting research question before selecting new lipids for the model system. Research conducted in **Paper I** (and partially in **Paper II)** focused more on the fundamental understanding of what aspects govern phospholipid segregation in a water gradient. In this work (Chapter 4.1), the behavior of phospholipids with different hydrocarbon tails (DOPC:DPPC) or different headgroup properties (DOPC:DOPE) was evaluated, leading to the conclusion that the water gradient induces the formation of gradients in the lipid composition. In **Paper I** it was shown that the solid lamellar phase ($L_{\beta'}$) with shorter-range repulsion was preferentially formed in the lower-hydration regime facing the air interface. As a further outlook, it would be of interest to study the segregation of phospholipids which still form the L_α and L_β structures but can exhibit more profound swelling behavior. An example of such a system would be a mixture of DOPC:DPPS in water. In this system, the headgroup of the PS lipid is charged. It is well known that the addition of PS lipids into the DOPC-L_α phase increases d-swelling up to ~70Å (199). Yet, the DPPS lipid alone in water forms an L_β structure with a similar d-spacing as DPPC (94). This means that the formation of a composition gradient in the interfacial multilayer can have a stronger effect on the long-range repulsion in the system. One open question is: *will the DPPS lipids preferentially form an L_β phase in the vicinity of the air interface or will the DPPS lipid be preferentially allocated in more hydrated conditions, contributing to the larger interbilayer swelling of an L_α phase?*

Follow-up studies on this topic could explore how strong is the effect with respect to the initial DOPC:DPPS bulk composition, or external RH conditions, in a similar manner as it was done in **Paper I**. Additionally, DOPS or DPPS could be added to the DOPC:DPPC systems which have already been studied in this work. In this case, the effect of similar headgroups versus the effect of similar hydrocarbon chains could be compared for the PS-lipid. Yet, for such a system ternary lipid system in water, the quantitative analysis approach that was developed in **Paper I** to study compositional gradient formation would not be applicable.

In **Paper II,** the model lipid systems were designed to mimic the composition of the TFLL layer. It was shown that the addition of DOPE to the DOPC:triolein lipid system

had a profound effect on the interfacial behavior, inducing tubulation. As an extension of this work, it would be of interest to add additional TFLL component representatives, particularly lipids belonging to the class of cholesteryl esters, such as cholesteryl oleate. Cholesteryl oleate has a distinct cholesterol headgroup structure, but unlike free cholesterol, it is non-polar due to the attached hydrocarbon chain at the polar cholesterol hydroxyl group (-OH). For this reason, cholesteryl oleate would be expected to preferentially segregate into the triolein-rich non-polar regions instead of the polar ones. It would be of interest to investigate how an increasing amount of cholesteryl oleate relative to triolein in a polar lipid system would influence the interfacial behavior and segregation. Such a study could provide further insight into how individual TFLL components contribute to the structural organization and stability of the tear film lipid layer. Investigating these effects would provide a molecular understanding of tear film stability and is of particular interest for the treatment of TFLL-related diseases.

This type of study can be further extended to examine the effect of abrupt and cyclic changes in external conditions. This was initiated as a proof of concept by dipping the multilayer structure into a water droplet (Fig. 30). It was observed that the non-polar lipid layer formed a barrier against tubule formation. Similarly, the capillary tip can be dipped into isotropic liquids to mimic conditions that are more representative of eye blinking (spreading of a nonpolar film), or into lipid formulations dispersed in water to simulate conditions relevant for pharmaceutical drug delivery.

Hopefully, these ideas will be successfully realized.

5. Stratum corneum systems

The stratum corneum (SC) is the outermost layer of the skin. It serves as the first and main barrier against water evaporation, chemical penetration and other harmful factors such as solar radiation (48). The SC layer is composed corneocytes filled with solid keratin filaments, corneodesmosomal junctions upholding the corneocyte structure, a complex extracellular lipid matrix, together with enzymes, chromophores and other small polar molecules (such as osmolytes). All these components work together to maintain the integrity of the SC barrier and its specific functions (50, 51). It has been established that there are two possible transportation routes for exogenous molecules to cross the SC layer and reach viable parts of the skin. Depending on the physicochemical properties of the molecule, the transport can occur either via 1) lipid matrix avoiding the water-rich corneocytes or 2) transversely passing both the water-rich corneocytes and the lipid matrix. In both cases, transport takes place through the lipids, meaning that the properties of the SC lipid matrix are crucial for the transdermal transport processes (56). Alterations in the SC lipids composition are associated with several skin diseases and well known to result in impaired barrier function of the skin (200). This motivates further study of the SC lipid matrix. In **Paper III**, we evaluated the structural responses of the SC lipids to changes in the environment conditions such as temperature and levels of hydration.

Additionally, fracture strength and strain of the SC layer have been shown to decrease significantly with increased exposure to UV light (89). UV radiation is also well known to cause photodamage to different chemical bonds, compounds and is able to alter the enzymatic activity in the SC layer (79-81). This motivates further study of the response of different SC components to external stimuli such as UV radiation. In **Paper IV**, we evaluated the response of different SC components to external stimuli, such as UVB radiation and oxidative stress. The results from the two papers will now be presented in two separate subsections and guided by the scientific questions.

5.1 Structure and mobility of the SC lipids in dry and fully hydrated conditions

The structural behavior of extracted SC lipids and SC lipid model systems with a few components has been extensively studied in the literature, providing fundamental understanding of the SC lipid structure and the importance of different lipid components. The SC lipid composition is distinctly different from many other biological membranes as they do not contain any phospholipids. The SC lipid matrix is instead composed of a vast number of different ceramides and free fatty acids along with high levels of cholesterol (60, 61). The lipids assemble into predominantly solid lamellar structures with either orthorhombic or hexagonal chain packing depending on the composition of the system. The most prominent and characteristic structure of the SC lipids is the so-called long periodicity phase (LPP), which has unusually large repeat distance (ca 130 Å) (64, 201, 202) . The LPP commonly coexists with other shorter repeat-distance lamellar phases, and several studies have shown that not all of the lipids in the matrix are solid (69, 180). To gain better insights into the behavior and fluidity of different SC lipid components in the SC layer, in **Paper III** we study the extracted SC lipids in both dry and fully hydrated conditions under a temperature cycle by employing small- and wide angle X-ray scattering (SAXS, WAXS) and solid stated NMR (PTssNMR) methods**.** The combination of these methods gives detailed information about the lamellar structures, crystalline packing and molecular dynamics of different lipid components. This work aims to answer the following questions:

- Do the SC lipids form the same structure in dry and fully hydrated conditions?
- Is there any difference in the mobility of different SC lipid components in the structure?

The self-assembly behavior of the extracted SC lipids was evaluated in a heating and cooling cycle at different hydration levels. First, the lipid samples are heated above the melting temperature (ca. 70°C) and a SAXS, WAXS and PTssNMR characterization is performed at 68°C, 45°C and 32°C. The SAXS data in Fig. 31A shows that the SC lipid recrystallizes to a characteristic LPP structure when cooled down to 45°C in dry condition, and that the formed structure does not change further when cooling to 32°C. The repeat distance of the LPP phase is constant at 14.3 nm, which agrees with previous reports from both the intact SC layer and SC model systems (63, 203). Up to the 7^{th} equidistant Bragg reflection of the LPP phase was identified in the spectra as indicated by the vertical black dotted lines. The WAXS spectra reveal that the

formation of the LPP phase is also associated with hexagonal hydrocarbon chain packing, which is indicated by a sharp peak at q = 15.2 nm^{-1} (d = 0.41 nm). The same hydrocarbon chain packing has been observed for porcine SC lipids in the literature (64, 200).

In Fig. 31B, the SC lipids were subjected to the same heating-cooling procedure but in fully hydrated conditions. Formation of an LPP phase is observed in a similar manner when cooling from 68°C to 45°C and further 32°C. The repeat distance of the LPP phase is slightly shorter in the fully hydrated condition (13.6 nm) in comparison with the dry conditions (14.3 nm). The LPP phase with up to the 6^{th} equidistant Bragg reflection can be identified in the spectra, as indicated by the black dotted lines. An additional peak is observed around the third LPP reflection at q = 1.19 nm-1 (d = 5.25 nm) as indicated by the red dotted line. This peak can correspond to a coexisting phase with shorter repeat distance but cannot be assigned due to an overlapping peak in the spectra. A sharp WAXS peak indicating hexagonal hydrocarbon chain packing is observed in the spectra associated with the LPP structure. The SAXS spectra obtained in dry and fully hydrated conditions at 45°C and 32°C are compared in the zoom-in panel C) and D) in Fig. 31, respectively.

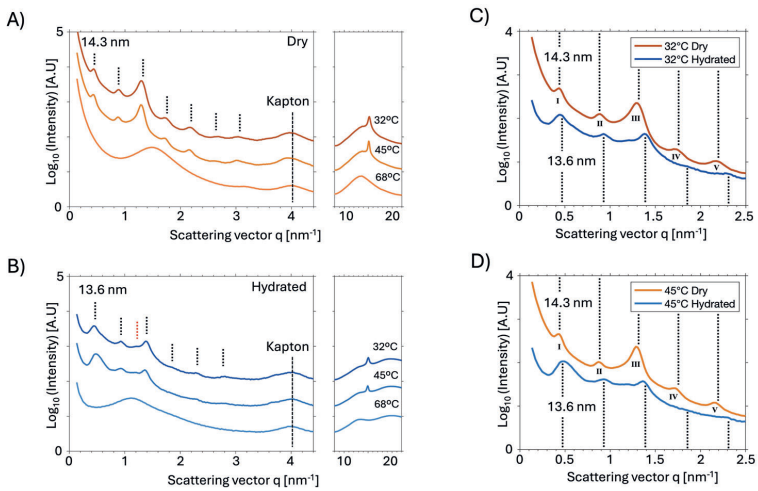

Figure 31. SAXS and WAXS spectra for A) dry SC lipids and B) fully hydrated SC lipids at varying temperatures, going from 68-45-32 °C. At 68 °C. The multiple reflections from the LPP structures with d = 14.3 and 13.6 nm (up to 7th order reflections) are indicated by the black dotted lines. C,D) Comparisons of SAXS spectra from the dry and hydrated SC lipid samples at 32 °C and 45 °C. The dotted lines indicate the theoretical positions of higher and lower order Bragg reflection based on the position of the second peak from the dry samples.

The molecular dynamics of the different SC lipid components subjected to the same temperature cycle in both dry and fully hydrated conditions were further evaluated by PTssNMR. In this method, the ^{13}C MAS NMR spectra of DP (grey), CP (blue) and INEPT (red) are compared with each other and between the different experiments to give information about the changes in the mobile and rigid states of the lipid components. The spectra from the low chemical shift region (10 - 85 ppm) show that most of the lipids in the dry SC lipid sample at 32°C and 45°C are rigid (Fig. 32A). This is inferred from the dominating CP signal in the spectra. A sharp INEPT signal from hydrocarbon chain components is also observed in the spectra. This indicates presence of an isotropic liquid fraction in the structure, which is consistent with previous observations in the literature of intact SC layer and model SC lipid systems (65, 68, 69, 204). It is observed that the CP signal in the spectra decreases with increasing temperature and the INEPT signal eventually dominates at 68°C. This indicates that the lipids are completely in an isotropic liquid state. Similar spectral behavior is observed for the SC lipids with increasing temperature in fully hydrated conditions (Fig. 32B). Additionally, the INEPT signal corresponding to cholesterol and ceramide headgroups increases at higher temperatures (45°C and 68°C), which indicates increased mobility in the fully hydrated samples compared with the dry state.

Taken together, the SAXS and WAXS spectra reveal that SC lipids adopt a well-ordered LPP structure with a hexagonal hydrocarbon chain arrangement in both dry and fully hydrated conditions. The ^{13}C MAS NMR analysis reveals presence of a minor mobile lipid fraction within the lamellar structure which become larger in the fully hydrated conditions. Interestingly, the LPP structure also displays a slight decrease in the lamellar repeat distance in fully hydrated condition. This behavior is in sharp contrast to many other lamellar phases composed of solid bilayer, for example the DPPC $L_{\beta'}$ gel phase, which swells in interlamellar distance but keeps the bilayer thickness unchanged (shown in Fig. 34). The decreased repeat distance of the LPP is likely caused by thinning of the lamellas as the fraction of fluid lipids increases.

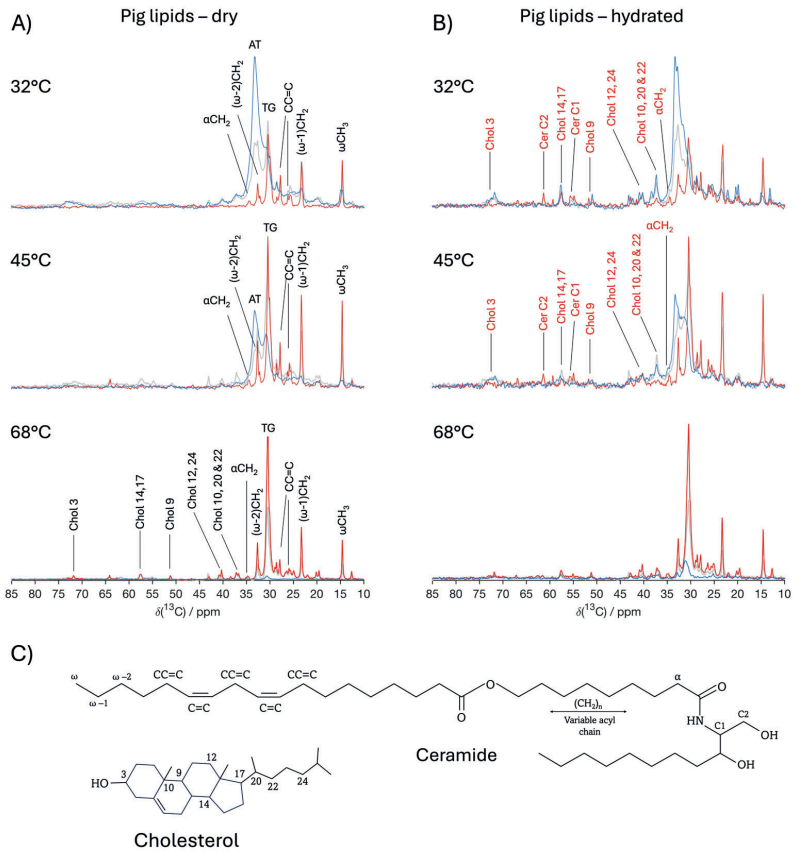

Figure 32. ^{13}C MAS NMR spectra for A) dry and B) fully hydrated SC lipids at temperatures going from 68-45-32 °C. The individual DP (gray), CP (blue) and INEPT (red) spectra are overlaid for comparison purpose. Prominent resonance lines originating from different molecular segments of SC lipids are labelled in black in the spectra from the dry samples. The red labelling in the spectra from the hydrated samples indicates increase in INEPT/DP signal ratio compared spectrum from the dry sample at that corresponding temperature. (C) Chemical structures with numbered/labelled segments of cholesterol and relevant lipid carbons (here illustrated with ceramide).

5.2 Response of the SC lipids to a water gradient

In reality, the SC lipids are present in a fluctuating water gradient, where the interior of the epidermis is always wet and the ambient exterior conditions can fluctuate from dry to fully hydrated RH conditions. Thus, in the second part of **Paper III** we aimed to answer the following questions:

- Are there any structural differences when the SC multilayer is formed at a drying interface compared to the bulk?
- How does the structure respond to an abrupt change in hydration?

To approach these questions, we evaluated the behavior of extracted SC lipids in a water gradient by using the drying-cell setup combined with SAXS mapping (Fig. 33A). This setup provides conditions that are more similar to the natural environment of the SC lipids in the skin. Fig. 33B. shows a birefringent SC lipid layer formed at the capillary tip facing dry conditions. SAXS characterization at different positions along the capillary axis was performed. It is observed that the SC lipids form the characteristic LPP structure with strong orientation relative to the air interface (Fig. 33D-E). The repeat distance of the LPP structure is 13.3 nm and remains constant along the water gradient as indicated by the dotted line (Fig. 33C). This repeat distance is in close agreement with that was observed for the fully hydrated SC lipids (Fig. 31B). Furthermore, a pronounced peak splitting and shift is observed around the third LPP reflection ($q = 1.4\ nm^{-1}$). In the zoom-in panel, it is observed that the 4.2 nm peak is much more pronounced in the regions facing bulk conditions and that the peak disappears towards the air interface. Simultaneously, a peak corresponding to 4.9 nm becomes more pronounced. Taken together, these data show that the LPP structure is robust and does not swell in a water gradient while a change in the repeat distance of the shorter phases is observed. This behavior cannot be resolved in bulk systems.

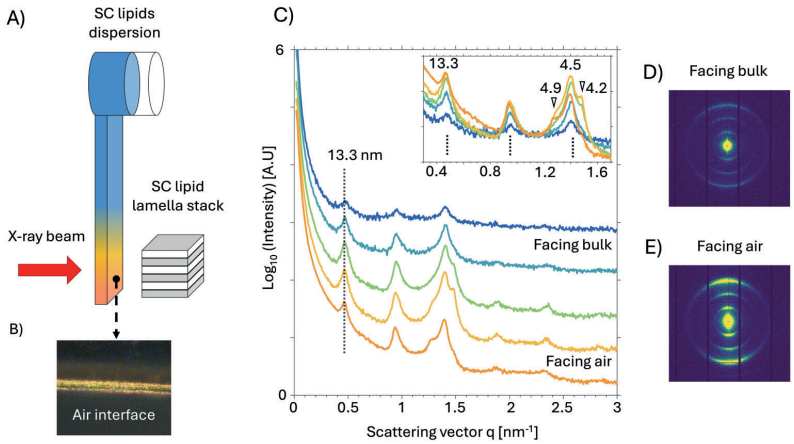

Figure 33. A)Schematic illustration of the capillary setup: An aqueous dispersion of SC lipids is added to the reservoir and flows towards the capillary tip that is exposed to air with controlled RH. This leads to the formation of an oriented multilayer film in the vicinity of the air interface. B) The birefringent interfacial layer formed at the capillary tip observed through optical microscopy with cross polarizers. The white bar corresponds to 1mm. C) Azimuthally averaged SAXS spectra obtained at different positions in the hydration gradient along the capillary axis. The LPP structure (13.3 nm) is indicated by a dotted line together with the reflections in the zoom in panel. D) 2D SAXS detector images revealing lamellar structure with strong alignment parallel to the air interface. The interfacial multilayer films were formed and characterized at T = 42°C.

The capillary tip with the SC multilayer structure is exposed to ambient air, which enables the study of how the structures respond to changes in the boundary conditions on the outer side of the layer. The capillary tip with an SC lipid multilayer film was dipped into a water droplet and the response of the multilayer was evaluated by SAXS mapping after the droplet was removed. The procedure is schematically illustrated in Fig. 34A. Fig. 34B shows a 2D SAXS map of the SC multilayer film along the capillary axis before the tip was dipped into water. The spectrum of this film serves as a reference for the phase behavior and structural response. By comparing the SAXS maps at different time points after the exposure to water, it was concluded that the abrupt change in boundary conditions does not influence the SC lipid structure within the examined time frame. This is illustrated in Fig. 34D where the SAXS spectrum from a fixed position in the multilayer film close to the interface is plotted versus time. As a comparison, the same experiment was performed for a lamellar gel phase ($L_{\beta'}$) with solid chain lipids made of DPPC (Fig. 34E and F), where a clear difference in the repeat distance in response to the change in boundary conditions is observed. The

interlamellar spacing increases in response to the increased water content at the boundary. From the combination of results from the bulk and non-equilibrium experiments (Fig. 31-34), it is proposed that the SC responds to changes in hydration in a functional way instead, by altering the balance between solid and fluid lipids, which are all embedded in the robust LPP structure. This is graphically illustrated in Fig. 35.

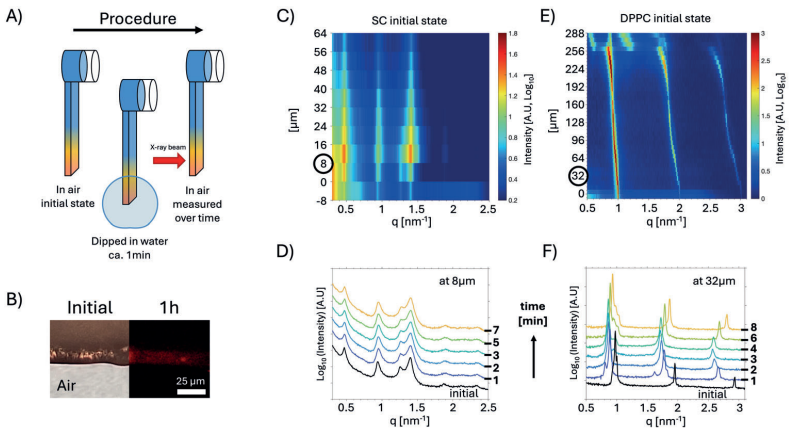

Figure 34 A) Schematic illustration of the experimental setup used to study the response of the interfacial multilayer structures to rapid changes in the outer boundary condition hydration. B). The birefringent interfacial layer formed at the capillary edge was observed using optical microscopy with crossed polarizers, while the penetration of Rhodamine B into the SC multilamellar structure was monitored over time by confocal fluorescence microscopy. Rhodamine B fluorophore was introduced into the water droplet (see panel A, exposure time 1 hour), which was then placed back in air for the measurements. SAXS maps of interfacial multilayer structures formed by C) SC lipids and E) DPPC gel phase prior to water exposure at the outer boundary. The maps display the scattering vector magnitude, q, versus the distance from the air−liquid interface, where the color scale corresponds to the logarithm of the scattered intensity. D) SAXS spectra recorded at one fixed position within the SC lipid interfacial layer (black circle in C) at different time points after the outer boundary was exposed to water and subsequently returned to dry air following the procedure in A. E) Corresponding SAXS spectra recorded at one fixed position within the DPPC gel phase layer (black circle in F) at different time points after water exposure. The SC lipid and the DPPC interfacial layers were formed at T = 42°C and 23°C, respectively and investigated by SAXS at the same temperatures.

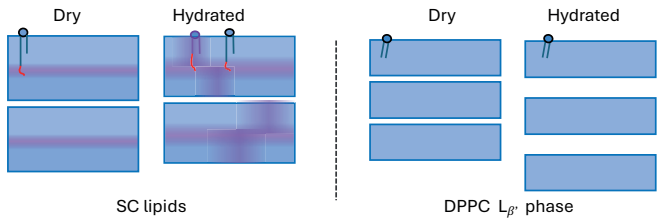

Figure 35. Cartoons illustrating different scenarios for the distribution of fluid (pink), and solid (blue) lipids in the extracellular SC lamellar structure under dry and hydrated conditions. When fluid lipids are present only as isolated regions embedded within the center of the solid lamellae in the LPP structure, there is no continuous pathway of fluid lipids across the stacked layers, resulting in very low effective water permeability. In contrast, when fluid lipid regions span across the lamellae in hydrated SC, a continuous route is formed. This functional response of SC lipids to hydration contrasts with the 1D swelling response of a phospholipid gel phase, where hydration increases interlamellar spacing but the bilayers remain solid.

Finally, the drying-cell setup was used to study the partitioning of small molecules into the SC multilayer structure. As a proof of concept, the Rhodamine B free base fluorophore was added to the water droplet at the capillary tip. Penetration of the dye into the SC lipid layer was observed by confocal fluorescence microscopy (Fig. 33B). This experiment demonstrates that hydrophobic molecules can enter the SC lipid layer from the outside and that the distribution of the dye molecules can be imaged over time. This work can be further extended to investigate the transport of different solutes within and across the SC lipid layer, as well as how these molecules affect the interfacial structure. This approach would provide valuable insights for transdermal delivery applications.

5.3 Effect of UVB on the antioxidative properties of the SC layer

This part of the thesis (**Paper IV**) aims to characterize the responses of different SC components to the external stimuli such as UVB radiation and oxidative stress. The SC layer is the first line of defense against solar UV radiation and is naturally equipped with chromophores and prosthetic groups that can directly absorb UV radiation and promote ROS formation. The accumulation of ROS molecules leads to oxidative stress, which can further lead to damage to cellular components such as lipids, proteins and nucleic acids components through oxidation.

Catalase is an antioxidative enzyme found throughout different layers of the skin, as well as in the SC layer. Catalase is well known to scavenge the ROS species hydrogen

peroxide (H_2O_2) with a very high turnover number. It's composed of four peptide chains forming a tetramer structure where each chain is equipped with an iron-containing Heme group that can decompose hydrogen peroxide into oxygen gas and water as: $2H_2O_2 \xrightarrow{Catalse} 2H_2O + O_2$. Hydrogen peroxide is also a natural by-product of cellular metabolism and is considered as one of the most abundant ROS species in the cells. Previous studies have shown that the catalase activity in the SC layer undergoes seasonal variation, where the enzyme becomes less active during the summer season due to solar radiation. Inactivation of catalase in a solution or when expressed in cells by UV radiation has also been shown. This means that the detrimental effect of UVB can be two-sided, leading to both ROS formation and the deactivation of ROS-scavenging enzyme catalase in the SC layer. In **Paper IV** we evaluated the effect of UVB radiation on the antioxidative properties of native catalase in the SC layer in a dose-depended manner. Here we asked:

- How does native catalase respond to an increasing UVB dosage, and is this effect reversible?

To approach this question experimentally, the lipid matrix was first separated from the SC layer to ensure easier and more homogenous transport of the substrate and formed product (H_2O_2 and O_2) through the SC layer for the electrochemical analysis of catalase activity. The catalase activity in this experiment was evaluated by oxygen electrode chronoamperometry, which has previously been described in reference (86). The extracted corneocyte matrix with entrapped catalase was mounted to top of an oxygen electrode and exposed to an increasing dose of UVB radiation. The effect of UVB on the antioxidative properties of catalase was evaluated by dipping the matrix-covered electrode into a buffer solution and sequentially adding H_2O_2. Formation of O_2 was measured as a function of increasing substrate concentration (by increments of 0.05mM) and converted to the reaction rate. Fig. 36A shows the reaction rate of the catalase as a function of increasing UVB dose investigated doses of 1, 2, 4 and 16 J/cm^2 corresponds to approximately 2, 4, 7 and 29h of constant solar UVB radiation. The results clearly show that the catalase activity in the corneocyte matrix decreases in a dose-dependent manner, leading to complete deactivation of the enzyme after 16 J/cm^2. This effect was irreversible; catalase did not regain its antioxidative properties after UVB deactivation.

To verify that the observed effect of catalase was not influenced by the extraction procedure involving mixtures of different organic solvents (which could otherwise denature the enzyme), the experiment was repeated using a film made of lyophilized catalase alone. The catalase film (1µg) was formed on a Tafone membrane from an

aliquot solution, mounted to top of the oxygen electrode, and exposed to UVB radiation in the same manner. For comparison, the normalized reaction rate of the catalase film and native catalase in the corneocyte matrix are plotted together in Fig. 36. Similar does-dependent deactivation of the catalase in the film was observed, where 16 J/cm^2 leads to complete and irreversible deactivation.

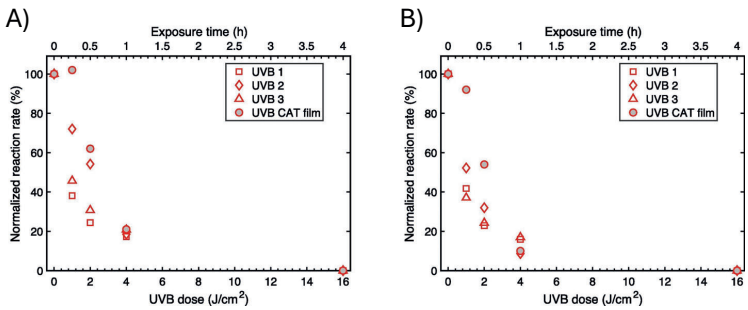

Figure 36. The effect of UVB radiation on the catalase reaction rate (νH_2O_2) in comparison to nonradiated reference samples. A) and B) show the normalized reduction in catalase reaction rate in corneocyte samples after increasing the substrate concentration by A) 0.05 mM and B) 0.20 mM (n = 3 for UVB irradiated and n = 1 for reference. For comparison, A) and B) also include data obtained with films of lyophilized catalase that were freshly prepared for each time point and initially measured without UVB radiation, followed by repeated measurements after UVB radiation (n = 1 for 5 separate samples).

These results highlight the sensitivity of catalase to UVB radiation. To investigate possible molecular explanations for the catalase deactivation, the structural changes and disintegration of the enzyme were evaluated by Circular Dichroism (CD) and SDS-PAGE after UVB exposure. In this work, it was also considered that UVB radiation can lead to the formation of reactive radical species in the presence of H_2O_2, which could also affect the structural features of the enzyme. No observable changes in the catalase's secondary structure were observed after exposure to 4 J/cm^2 of UVB irradiation (Fig. 37A). The result was the same, irrespective of elevated levels of H_2O_2 in the solution (100mM). The same result was obtained for higher UVB dose (16 J/cm^2) and H_2O_2 in different buffers (data is provided in the SI section of **Paper IV**). Thus, it is concluded that the observed catalase deactivation is not caused by changes in the secondary structure. Furthermore, disintegration of catalase was evaluated after treatment with 4 J/cm^2 of UVB radiation in the presence and absence of H_2O_2 (100 mM) by means of SDS-PAGE. No disintegration of the catalase was observed after the treatment as the catalase band (at ~57 kDa) remained unaffected (in Fig. 37B). This indicates that the catalase deactivation is not caused by degradation of the enzyme. Further analysis of the effect of UVB on the active site of the catalase enzyme (Heme group) was beyond the scope of this thesis work.

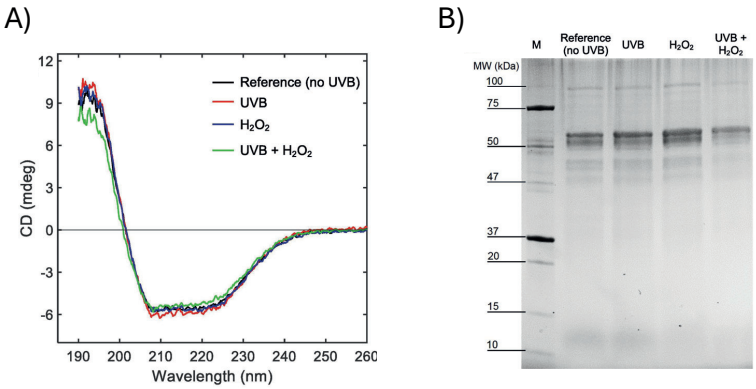

Figure 37. A) Normalized CD spectra of catalase where the reference sample corresponds to lyophilized catalase (0.11 mg/ml) in PB; UVB represents an identical sample but exposed to 4 J/cm2 of UVB radiation. The samples with H2O2 were obtained in the presence of 100 mM H2O2, with or without 4 J/cm2 UVB exposure. (B) Results from SDS-PAGE measurements with the same conditions as for CD experiments, except that 5 µg of lyophilized catalase was used per 20 µL well and PBS was used as buffer. In (B), the intensity of lane H2O2 + UVB is due to loss of material due to O2 bubbling during the sample preparation.

5.4 Effect of UVB on the structure and mobility of different SC components

After evaluating the influence of UVB irradiation on the antioxidative properties of catalase in the SC matrix, we further evaluated the effect of UVB radiation on the SC matrix that surrounds the enzyme, including both SC lipids and corneocytes. UVB radiation can cause chemical damage directly, for example by modifying C=C bonds, or indirectly (via endogenous sensitizers) by promoting ROS formation, which can lead to oxidation of other chemical groups such as C=O. These effects can result in structural alterations in the SC matrix, including isomerization of the lipid hydrocarbon chains and modification of protein backbones containing amide bonds (79-81). Although previous studies have evaluated the effect of elevated UVB doses on the mechanical and macroscopic properties of the epidermis layer (88-90), the effect of UVB on the molecular structure and mobility of the SC components has not been evaluated. In **Paper IV**, the changes in the molecular structure and mobility of the SC components are evaluated after UVB exposure and correlated with macroscopic properties of water sorption. Here we ask:

- Does UVB irradiation alter the structure of SC components?
- Does UVB irradiation influence the molecular dynamics in the SC components?

To address these questions, the SC layer and extracted corneocyte layer were exposed to a high UVB dose of 160 J/cm^2 at different RH conditions and characterized by means of WAXS. A UVB dose of 160 J/cm^2 corresponds approximately to 14 continuous days of solar UVB exposure to the skin (89). Fig. 38A shows WAXS spectra of the SC layer after exposure to 160 J/cm^2 UVB at 84 %RH and 97 %RH. No major changes in the lipid and protein structure are observed. For the SC samples, the lipids preserved their hexagonal hydrocarbon chain packing as indicated by the 0.41 nm peak. On the other hand, a small decrease in the shoulder intensity at 0.57 nm and 0.52 nm, corresponding to the α-helical and β-sheet of keratin respectively, was observed at 84% RH after UVB exposure. The observed difference in the peak intensities may be attributed to the natural variation in the sample composition and could be enhanced by the curve normalization. No alteration in interchain distance (at q = 6.3 nm^{-1}) in the coiled coil dimer of the keratin filament was observed after UVB radiation in both SC and corneocyte samples.

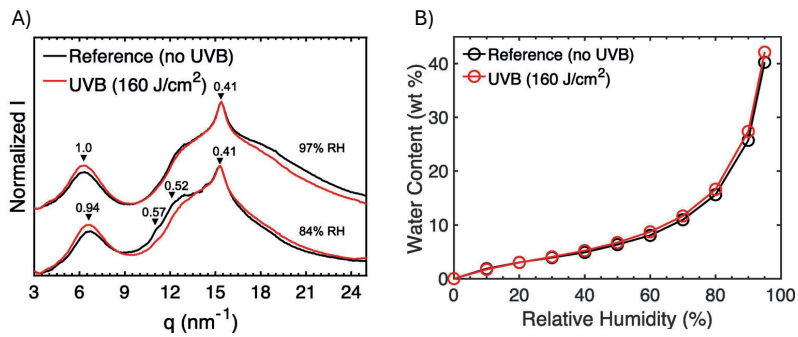

Figure 38. A) The effects of UVB radiation on the SC molecular organization studies by WAXD . The reference samples correspond to a non-irradiated SC samples (black) while UVB represents samples exposed to 160 J/cm2 of irradiation (red). Diffraction curves in A) were obtained after equilibration the SC samples at 84 % and 97 % RH. The intensity, $\log_{10}$ I, in (A) is normalized to give identical values at q = 15.2 nm−1. Numbers marked by arrows give the d-spacing in nm B) The effect of UVB radiation on the SC water uptake. The reference sample corresponds to non-irradiated SC sample (black) while UVB represents the identical sample exposed to 160 J/cm2 of irradiation (red).

Before evaluating the effect of UVB on the mobility of the SC components, it was examined whether the UVB radiation causes any alteration in the water sorption properties of the SC components. Fig. 38B shows that the water sorption of the SC layer remains almost unaffected by UVB irradiation. This result indicates that the structural changes observed in the WAXS characterization are not caused by the differences in the water content.

Finally, the molecular dynamics of the SC components was evaluated by means of PTssNMR at different humidities. Previous studies have shown that the mobility of SC lipids increases gradually with increasing RH, whereas the protein components exhibit a threshold behavior where significant mobility is only observed at RH levels above approximately 85–90% (55, 68). The PTssNMR spectra of non-irradiated SC layer equilibrated at 97% RH shown in Fig. 39A are used as a reference to assess the effect of UVB irradiation on the different protein and lipid components at the same RH. The majority of the SC components are rigid, which is inferred from the high CP signal (blue) relative to the DP signal (gray). INEPT signal (red) corresponding to several protein components of keratin and lipid groups are identified in the reference spectra, which agrees with previous observations (55, 68).

For both UVB doses (80 J/cm^2 and 280 J/cm^2), a small change in the molecular dynamics of SC lipid and protein components is observed after the UVB exposure (Fig. 38B-C). For example, the mobility of the terminal regions of the lipid alkyl chains (i.e., ωCH_3 and $(\omega\text{-}1)CH_3$) increased after UV exposure, as indicated by the increased INEPT signal with respect to the DP signal, while the mobility of the hydrocarbon chains (TG) decreased as indicated by the increased CP signal with respect to DP after UVB exposure. Furthermore, the rigidity of several protein groups corresponding to the polypeptide backbone of keratin (Leu Cβ and/or Lys Cε) increased after UVB exposure. An increased rigidity of the carbonyl carbon (at 177 ppm), which can indicate increased rigidity of the polypeptide chain within the keratin filaments, is also observed with increased UVB exposure. The rigidity of the C=C segment is also increased as indicated in the 130-140 ppm shift region, except for the peak at 130.5 ppm where a sharp INEPT signal is observed. The resonances in the 130-140 ppm region can arise from several SC components such as unsaturated lipid segments of free fatty acids and ceramides, and also from the amino acid residues found in Tyr, His and Phe.

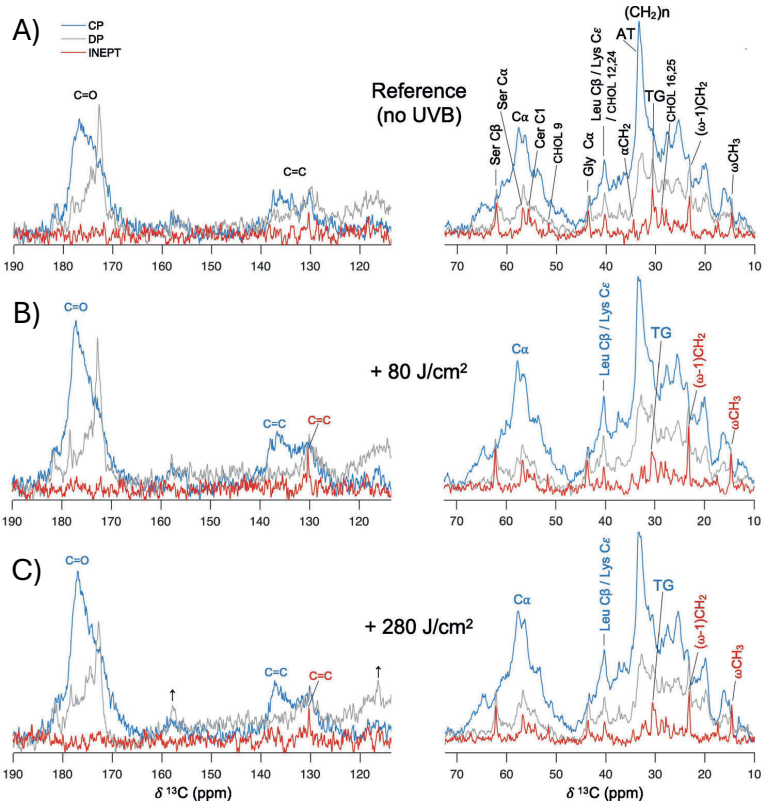

Figure 39. PT ssNMR 13C results of SC samples exposed to A) 0, B) 80, and C) 280 J/cm2 and finally equilibrated at 97 % RH (See Paper IV for signature peaks and meaning of coloring, table for the peak assignment is in the SI secion).

Taken together, after evaluating the effect of a broad range of UVB doses on different aspects of the SC layer, a clear asymmetry in the response was observed. The UVB irradiation had a strong effect on the antioxidative response, leading to irreversible deactivation of catalase, while the structural and molecular characteristics of the SC layer remained largely unchanged, even after exposure to comparably high UVB doses. The deactivation of catalase was not caused by increased levels of H_2O_2 nor by changes in the enzyme's secondary structure or degradation. This suggests that the effect of deactivation could be attributed to the changes in the active site (as for example the Heme-groups) of the catalase, which should be further investigated.

5.5 Conclusion and outlook

In **Paper III** it was demonstrated that the stratum corneum (SC) lipids are able to adapt to a water gradient in a more complex manner than through interbilayer swelling. By employing the drying-cell setup combined with microbeam X-ray scanning, an improved resolution of the structural features was achieved compared to the bulk samples. This is mainly caused by the strong orientation of the SC lipids with respect to the air interface (i.e., horizontal stacking) which minimizes diffuse scattering from the sample and enhances sharpness of diffraction peaks.

In this work, it was shown that the Rhodamine B is able to partition into the SC layer (Fig. 34). As a further extension of this study, it would be of interest to investigate molecular transport within the SC lipid multilayer in comparison to DPPC-$L_{\beta'}$ multilayer. By forming thicker multilayer films in the drying-cell setup, one could potentially monitor the partitioning or diffusion of the fluorescent probes through the multilayer films in a more controlled way. The lamellar phases formed by SC lipids and DPPC exhibit structurally different responses to abrupt changes in hydration (Fig. 34), where the DPPC multilayer displays large interbilayer swelling which is not found for SC multilayer. With this in mind, it would be valuable to evaluate how these differences influence the transport processes of, for example, hydrophilic and hydrophobic molecules, respectively. Such a study could be potentially employ fluorescence correlation spectroscopy (FCS) and pair-correlation function (pCF) analysis to investigate fluorophore dynamics (205). Insights from such study would provide a deeper understanding of the structural responses, permeability and barrier properties of SC lipids.

As a further outlook, it would be of interest to systematically evaluate the effects of relevant additives on the structural organization of the SC lipids and to determine whether they influence their response to hydration. There is a broad range of interesting molecules one can select for this type of study. For cosmetically and pharmaceutically relevant formulations, the effect of moisturizers and active compounds such as glycerol, urea, hyaluronic acid, and salicylic acid can be investigated (206, 207). These molecules are used in the treatment of skin-related conditions such as dry skin, psoriasis and ichthyosis, where the barrier function of SC lipids is compromised (208, 209). Insights gained from such studies would provide a deeper understanding of how additives influence SC lipid organization at the drying interface and could potentially lead to the development of improved topical formulations.

It is well known that UVB exposure of the skin causes inflammation, leading to erythema (210-212). The experimental approach used in this work (**Paper IV**) could be further applied to investigate the effects of UVB on the functional, structural and molecular properties of the newly formed SC, following UVB exposure of the viable proliferating layers of the tissue. These experiments could be extended to study the effect of UVA exposure, which could potentially enable to distinguish effects of UVA and UVB on the bio-enzymatic pathways responsible for proliferation and SC layer formation.

Hopefully, these ideas will be successfully realized.

Reference

1. S. M. Shirreffs, R. J. Maughan, "ELECTROLYTES | Water–Electrolyte Balance" in Encyclopedia of Human Nutrition (Second Edition), B. Caballero, Ed. (Elsevier, Oxford, 2005), pp. 100–105.
2. E. Jéquier, F. Constant, Water as an essential nutrient: the physiological basis of hydration. *Eur J Clin Nutr* **64**, 115–123 (2010).
3. S. J. Zheng, Y. Li, Y. F. Shao, L. Li, F. Song, Osmotic Pressure and Its Biological Implications. *Int J Mol Sci* **25** (2024).
4. H. Wennerstrom, M. Oliveberg, On the osmotic pressure of cells. *QRB Discov* **3**, e12 (2022).
5. F. Lang *et al.*, Functional significance of cell volume regulatory mechanisms. *Physiol Rev* **78**, 247–306 (1998).
6. R. Feistel, J. W. Lovell-Smith, Defining relative humidity in terms of water activity. Part 1: definition. *Metrologia* **54**, 566–576 (2017).
7. P. Bertsch, J. Bergfreund, E. J. Windhab, P. Fischer, Physiological fluid interfaces: Functional microenvironments, drug delivery targets, and first line of defense. *Acta Biomater* **130**, 32–53 (2021).
8. P. Bouwstra J. A., G. S. K., Ponec M., "Structure of the Skin Barrier" in Skin Barrier. (Taylor & Francis Group, New York, 2006), vol. 1, chap. 7, pp. 65–98.
9. A. Bidani, E. D. Crandall, Velocity of CO2 exchanges in the lungs. *Annu Rev Physiol* **50**, 639–652 (1988).
10. V. Pretini *et al.*, Red Blood Cells: Chasing Interactions. *Front Physiol* **10**, 945 (2019).
11. S. Han, R. K. Mallampalli, The Role of Surfactant in Lung Disease and Host Defense against Pulmonary Infections. *Ann Am Thorac Soc* **12**, 765–774 (2015).
12. J. Pérez-Gil, K. M. W. Keough, Interfacial properties of surfactant proteins. *Bba-Mol Basis Dis* **1408**, 203–217 (1998).
13. C. J. Lang *et al.*, Dipalmitoylphosphatidylcholine is not the major surfactant phospholipid species in all mammals. *Am J Physiol Regul Integr Comp Physiol* **289**, R1426–1439 (2005).
14. A. D. Postle, E. L. Heeley, D. C. Wilton, A comparison of the molecular species compositions of mammalian lung surfactant phospholipids. *Comp Biochem Phys A* **129**, 65–73 (2001).
15. F. Possmayer, Y. Y. Zuo, R. A. W. Veldhuizen, N. O. Petersen, Pulmonary Surfactant: A Mighty Thin Film. *Chem Rev* **123**, 13209–13290 (2023).
16. F. F. Wang, J. F. Liu, H. B. Zeng, Interactions of particulate matter and pulmonary surfactant: Implications for human health. *Adv Colloid Interfac* **284** (2020).

17. Y. Y. Zuo, R. A. W. Veldhuizen, A. W. Neumann, N. O. Petersen, F. Possmayer, Current perspectives in pulmonary surfactant - Inhibition, enhancement and evaluation. *Bba-Biomembranes* **1778**, 1947–1977 (2008).
18. M. E. Avery, S. Said, Surface Phenomena in Lungs in Health and Disease. *Medicine* **44**, 503–+ (1965).
19. R. F. Soll, Synthetic surfactant for respiratory distress syndrome in preterm infants. *Cochrane Database Syst Rev* **1998**, CD001149 (2000).
20. A. Dushianthan, R. Cusack, V. Goss, A. D. Postle, M. P. W. Grocott, Clinical review: Exogenous surfactant therapy for acute lung injury/acute respiratory distress syndrome - where do we go from here? *Crit Care* **16** (2012).
21. R. J. r. McIntyre, E. J. Pulido, D. D. Bensard, B. D. Shames, E. Abraham, Thirty years of clinical trials in acute respiratory distress syndrome. *Crit Care Med* **28**, 3314–3331 (2000).
22. R. A. Polin, W. A. Carlo, C. F. Newborn, Surfactant Replacement Therapy for Preterm and Term Neonates With Respiratory Distress. *Pediatrics* **133**, 156–163 (2014).
23. R. F. Soll, F. Blanco, Natural surfactant extract versus synthetic surfactant for neonatal respiratory distress syndrome. *Cochrane Database Syst Rev* 10.1002/14651858.CD000144, CD000144 (2001).
24. M. Mussavi, K. Mirnia, K. Asadollahi, Comparison of the Efficacy of Three Natural Surfactants (Curosurf, Survanta, and Alveofact) in the Treatment of Respiratory Distress Syndrome Among Neonates: A Randomized Controlled Trial. *Iran J Pediatr* **26**, e5743 (2016).
25. J. M. Andersson, K. Roger, M. Larsson, E. Sparr, The Impact of Nonequilibrium Conditions in Lung Surfactant: Structure and Composition Gradients in Multilamellar Films. *Acs Central Sci* **4**, 1315–1325 (2018).
26. L. Cwiklik, Tear film lipid layer: A molecular level view. *Bba-Biomembranes* **1858**, 2421–2430 (2016).
27. P. E. King-Smith, B. A. Fink, R. M. Hill, K. W. Koelling, J. M. Tiffany, The thickness of the tear film. *Curr Eye Res* **29**, 357–368 (2004).
28. P. E. King-Smith *et al.*, The thickness of the human precorneal tear film: Evidence from reflection spectra. *Invest Ophth Vis Sci* **41**, 3348–3359 (2000).
29. T. J. Millar, B. S. Schuett, The real reason for having a meibomian lipid layer covering the outer surface of the tear film - A review. *Experimental Eye Research* **137**, 125–138 (2015).

30. T. F. Svitova, M. C. Lin, Evaporation retardation by model tear-lipid films: The roles of film aging, compositions and interfacial rheological properties. *Colloid Surface B* **197** (2021).
31. S. H. J. Brown *et al.*, A Comparison of Patient Matched Meibum and Tear Lipidomes. *Invest Ophth Vis Sci* **54**, 7417–7423 (2013).
32. S. M. Lam *et al.*, Extensive characterization of human tear fluid collected using different techniques unravels the presence of novel lipid amphiphiles. *J Lipid Res* **55**, 289–298 (2014).
33. J. Z. Chen, K. B. Green, K. K. Nichols, Quantitative Profiling of Major Neutral Lipid Classes in Human Meibum by Direct Infusion Electrospray Ionization Mass Spectrometry. *Invest Ophth Vis Sci* **54**, 5730–5753 (2013).
34. I. A. Butovich, Meibomian glands, meibum, and meibogenesis. *Exp Eye Res* **163**, 2–16 (2017).
35. I. A. Butovich, Tear film lipids. *Exp Eye Res* **117**, 4–27 (2013).
36. A. Rantamäki, J. Telenius, A. Koivuniemi, I. Vattulainen, J. M. Holopainen, Lessons from the biophysics of interfaces: Lung surfactant and tear fluid. *Prog Retin Eye Res* **30**, 204–215 (2011).
37. J. P. McCulley, W. Shine, A compositional based model for the tear film lipid layer. *Trans Am Ophthalmol Soc* **95**, 79–88; discussion 88–93 (1997).
38. M. S. Norn, Desiccation of the precorneal film. I. Corneal wetting-time. *Acta Ophthalmol (Copenh)* **47**, 865–880 (1969).
39. F. J. Holly, Diagnostic Methods and Treatment Modalities of Dry Eye Conditions. *Int Ophthalmol* **17**, 113–125 (1993).
40. J. D. Sheppard, K. K. Nichols, Dry Eye Disease Associated with Meibomian Gland Dysfunction: Focus on Tear Film Characteristics and the Therapeutic Landscape. *Ophthalmol Ther* **12**, 1397–1418 (2023).
41. S. Khanal *et al.*, Human meibum and tear film derived cholesteryl and wax esters in meibomian gland dysfunction and tear film structure. *Ocul Surf* **23**, 12–23 (2022).
42. F. Lallemand, J.-S. Garrigue, "Emulsions for Topical Eye Delivery: State of the Art and Future Perspectives" in Ophthalmic Product Development: From Bench to Bedside, S. Neervannan, U. B. Kompella, Eds. (Springer International Publishing, Cham, 2021), 10.1007/978-3-030-76367-1_13, pp. 349–379.
43. S. Reimondez-Troitiño, N. Csaba, M. J. Alonso, M. de la Fuente, Nanotherapies for the treatment of ocular diseases. *Eur J Pharm Biopharm* **95**, 279–293 (2015).

44. J. S. Garrigue, M. Amrane, M. O. Faure, J. M. Holopainen, L. Tong, Relevance of Lipid-Based Products in the Management of Dry Eye Disease. *J Ocul Pharmacol Th* **33**, 647–661 (2017).
45. J. J. López-Cano, M. A. González-Cela-Casamayor, V. Andrés-Guerrero, R. Herrero-Vanrell, I. T. Molina-Martínez, Liposomes as vehicles for topical ophthalmic drug delivery and ocular surface protection. *Expert Opin Drug Del* **18**, 819–847 (2021).
46. E. Sánchez-López *et al.*, "Nanoparticle Products for the Eye: Preformulation, Formulation, and Manufacturing Considerations" in Ophthalmic Product Development: From Bench to Bedside, S. Neervannan, U. B. Kompella, Eds. (Springer International Publishing, Cham, 2021), 10.1007/978-3-030-76367-1_15, pp. 409–447.
47. B. Yavuz, U. B. Kompella, "Ocular Drug Delivery" in Pharmacologic Therapy of Ocular Disease, S. M. Whitcup, D. T. Azar, Eds. (Springer International Publishing, Cham, 2017), 10.1007/164_2016_84, pp. 57–93.
48. H. Shimizu, "Structure and function of the skin" in Shimizu's Dermatology. (2017), pp. 1–42.
49. R. J. Scheuplein, I. H. Blank, Permeability of the skin. *Physiol Rev* **51**, 702–747 (1971).
50. E. Candi, R. Schmidt, G. Melino, The cornified envelope: a model of cell death in the skin. *Nat Rev Mol Cell Biol* **6**, 328–340 (2005).
51. P. M. Elias, Epidermal lipids, barrier function, and desquamation. *J Invest Dermatol* **80**, 44s–49s (1983).
52. C. L. Silva *et al.*, Stratum corneum hydration: phase transformations and mobility in stratum corneum, extracted lipids and isolated corneocytes. *Biochim Biophys Acta* **1768**, 2647–2659 (2007).
53. J. A. Bouwstra *et al.*, Water distribution and related morphology in human stratum corneum at different hydration levels. *Journal of Investigative Dermatology* **120**, 750–758 (2003).
54. B. Wang, W. Yang, J. McKittrick, M. A. Meyers, Keratin: Structure, mechanical properties, occurrence in biological organisms, and efforts at bioinspiration. *Prog Mater Sci* **76**, 229–318 (2016).
55. E. H. Mojumdar, Q. D. Pham, D. Topgaard, E. Sparr, Skin hydration: interplay between molecular dynamics, structure and water uptake in the stratum corneum. *Sci Rep* **7**, 15712 (2017).
56. E. Sparr *et al.*, The stratum corneum barrier - From molecular scale to macroscopic properties. *Curr Opin Colloid In* **67** (2023).
57. N. J. Starr *et al.*, Elucidating the molecular landscape of the stratum corneum. *P Natl Acad Sci USA* **119** (2022).
58. L. Norlen, I. Nicander, A. Lundsjo, T. Cronholm, B. Forslind, A new HPLC-based method for the quantitative analysis of inner stratum

corneum lipids with special reference to the free fatty acid fraction. *Arch Dermatol Res* **290**, 508–516 (1998).
59. P. W. Wertz, M. Kremer, C. A. Squier, Comparison of lipids from epidermal and palatal stratum corneum. *J Invest Dermatol* **98**, 375–378 (1992).
60. M. Suzuki, Y. Ohno, A. Kihara, Whole picture of human stratum corneum ceramides, including the chain-length diversity of long-chain bases. *J Lipid Res* **63** (2022).
61. J. van Smeden *et al.*, Combined LC/MS-platform for analysis of all major stratum corneum lipids, and the profiling of skin substitutes. *Bba-Mol Cell Biol L* **1841**, 70–79 (2014).
62. J. A. Bouwstra, G. S. Gooris, M. A. Salomonsdevries, J. A. Vanderspek, W. Bras, Structure of Human Stratum-Corneum as a Function of Temperature and Hydration - a Wide-Angle X-Ray-Diffraction Study. *Int J Pharm* **84**, 205–216 (1992).
63. S. H. White, D. Mirejovsky, G. I. King, Structure of Lamellar Lipid Domains and Corneocyte Envelopes of Murine Stratum-Corneum - an X-Ray-Diffraction Study. *Biochemistry-Us* **27**, 3725–3732 (1988).
64. J. A. Bouwstra, G. S. Gooris, F. E. R. Dubbelaar, M. Ponec, Phase behavior of lipid mixtures based on human ceramides: coexistence of crystalline and liquid phases. *J Lipid Res* **42**, 1759–1770 (2001).
65. Q. D. Pham, S. Bjorklund, J. Engblom, D. Topgaard, E. Sparr, Chemical penetration enhancers in stratum corneum - Relation between molecular effects and barrier function. *J Control Release* **232**, 175–187 (2016).
66. A. Alonso, N. C. Meirelles, V. E. Yushmanov, M. Tabak, Water increases the fluidity of intercellular membranes of stratum corneum: Correlation with water permeability, elastic, and electrical resistance properties. *Journal of Investigative Dermatology* **106**, 1058–1063 (1996).
67. O. Engberg *et al.*, The Sphingosine and Acyl Chains of Ceramide [NS] Show Very Different Structure and Dynamics That Challenge Our Understanding of the Skin Barrier. *Angew Chem Int Edit* **59**, 17383–17387 (2020).
68. S. Björklund, A. Nowacka, J. A. Bouwstra, E. Sparr, D. Topgaard, Characterization of Stratum Corneum Molecular Dynamics by Natural-Abundance C Solid-State NMR. *Plos One* **8** (2013).
69. F. Fandrei *et al.*, The intriguing molecular dynamics of Cer[EOS] in rigid skin barrier lipid layers requires improvement of the model. *J Lipid Res* **64** (2023).

70. A. P. Ramos, G. Gooris, J. Bouwstra, M. Lafleur, Evidence of hydrocarbon nanodrops in highly ordered stratum corneum model membranes. *J Lipid Res* **59**, 137–143 (2018).
71. I. Sagrafena *et al.*, Assembly of Human Stratum Corneum Lipids In Vitro: Fluidity Matters. *Journal of Investigative Dermatology* **142**, 2036–2039 (2022).
72. J. A. Bouwstra, M. Ponec, The skin barrier in healthy and diseased state. *Bba-Biomembranes* **1758**, 2080–2095 (2006).
73. B. Cravello, A. Ferri, Relationships between skin properties and environmental parameters. *Skin Res Technol* **14**, 180–186 (2008).
74. I. H. Blank, J. Moloney, A. G. Emslie, I. Simon, C. Apt, The Diffusion of Water across the Stratum-Corneum as a Function of Its Water-Content. *Journal of Investigative Dermatology* **82**, 188–194 (1984).
75. M. R. Prausnitz, R. Langer, Transdermal drug delivery. *Nat Biotechnol* **26**, 1261–1268 (2008).
76. S. Björklund, J. Engblom, K. Thuresson, E. Sparr, A water gradient can be used to regulate drug transport across skin. *J Control Release* **143**, 191–200 (2010).
77. A. Rawlings, "Sources and Role of Stratum Corneum Hydration". (2005), 10.1201/b14173-25, pp. 399–425.
78. K. Maeno, Direct Quantification of Natural Moisturizing Factors in Stratum Corneum using Direct Analysis in Real Time Mass Spectrometry with Inkjet-Printing Technique. *Sci Rep-Uk* **9** (2019).
79. J. D'Orazio, S. Jarrett, A. Amaro-Ortiz, T. Scott, UV Radiation and the Skin. *Int J Mol Sci* **14**, 12222–12248 (2013).
80. D. I. Pattison, M. J. Davies, Actions of ultraviolet light on cellular structures. *EXS* 10.1007/3-7643-7378-4_6, 131–157 (2006).
81. M. Menoni, P. Alcoba, M. J. Zuluaga, R. D. Peluffo, Generation of cellular reactive oxygen and nitrogen species by exposure to ultraviolet radiation. *Biophys Rev* **17**, 547–560 (2025).
82. S. Briganti, M. Picardo, Antioxidant activity, lipid peroxidation and skin diseases. What's new. *J Eur Acad Dermatol Venereol* **17**, 663–669 (2003).
83. F. A. Wagener, C. E. Carels, D. M. Lundvig, Targeting the redox balance in inflammatory skin conditions. *Int J Mol Sci* **14**, 9126–9167 (2013).
84. Y. Shindo, E. Witt, D. Han, W. Epstein, L. Packer, Enzymic and non-enzymic antioxidants in epidermis and dermis of human skin. *J Invest Dermatol* **102**, 122–124 (1994).
85. S. Nocchi, S. Bjorklund, B. Svensson, J. Engblom, T. Ruzgas, Electrochemical monitoring of native catalase activity in skin using skin covered oxygen electrode. *Biosens Bioelectron* **93**, 9–13 (2017).

86. M. Szczepanczyk, T. Ruzgas, F. Gullfot, A. Gustafsson, S. Bjorklund, Catalase Activity in Keratinocytes, Stratum Corneum, and Defatted Algae Biomass as a Potential Skin Care Ingredient. *Biomedicines* **9** (2021).
87. L. Hellemans, H. Corstjens, A. Neven, L. Declercq, D. Maes, Antioxidant enzyme activity in human stratum corneum shows seasonal variation with an age-dependent recovery. *J Invest Dermatol* **120**, 434–439 (2003).
88. A. R. Hernandez, B. Vallejo, T. Ruzgas, S. Bjorklund, The Effect of UVB Irradiation and Oxidative Stress on the Skin Barrier-A New Method to Evaluate Sun Protection Factor Based on Electrical Impedance Spectroscopy. *Sensors (Basel)* **19** (2019).
89. K. Biniek, K. Levi, R. H. Dauskardt, Solar UV radiation reduces the barrier function of human skin. *Proc Natl Acad Sci U S A* **109**, 17111–17116 (2012).
90. Z. W. Lipsky, G. K. German, Ultraviolet light degrades the mechanical and structural properties of human stratum corneum. *J Mech Behav Biomed Mater* **100**, 103391 (2019).
91. O. G. Mouritsen, L. A. Bagatolli, "Head and Tail" in LIFE - AS A MATTER OF FAT: Lipids in a Membrane Biophysics Perspective. (Springer International Publishing, Cham, 2016), 10.1007/978-3-319-22614-9_2, pp. 19–30.
92. D. F. W. Evans, Håkan, "Solutes and solvents, Self-assembly of Amphiphiles" in Colloidal Domain: Where Physics, Chemistry, Biology, and Technology Meet. (John Wiley & Sons Inc, Canada, 1999), chap. 1, pp. 1–45.
93. G. Cevc, How membrane chain-melting phase-transition temperature is affected by the lipid chain asymmetry and degree of unsaturation: an effective chain-length model. *Biochemistry-Us* **30**, 7186–7193 (1991).
94. R. Koynova, B. Tenchov, "Phase Transitions and Phase Behavior of Lipids" in Encyclopedia of Biophysics, G. C. K. Roberts, Ed. (Springer Berlin Heidelberg, Berlin, Heidelberg, 2013), 10.1007/978-3-642-16712-6_542, pp. 1841–1854.
95. D. F. W. Evans, Håkan, "Forces in Colloidal Systems" in Colloidal Domain: Where Physics, Chemistry, Biology, and Technology Meet. (John Wiley & Sons Inc, Canada, 1999), chap. 5, pp. 217–294.
96. B. H. Kronberg, K; and Lindman, B., "Emulsions and Emulsifiers" in Surface Chemistry of Surfactants and Polymers. (Wiley & Sons, Ltd., United Kingdom, 2014), chap. 24, pp. 431–445.

97. D. Cholakova, S. Tcholakova, N. Denkov, Polymorphic Phase Transitions in Bulk Triglyceride Mixtures. *Cryst Growth Des* **23**, 2075–2091 (2023).
98. N. Arita-Merino, H. van Valenberg, E. P. Gilbert, E. Scholten, Quantitative Phase Analysis of Complex Fats during Crystallization. *Cryst Growth Des* **20**, 5193–5202 (2020).
99. Anonymous, "Lipids Speak the Language of Curvature" in Life — As a Matter of Fat: The Emerging Science of Lipidomics. (Springer Berlin Heidelberg, Berlin, Heidelberg, 2005), 10.1007/3-540-27076-0_5, pp. 43–52.
100. T. Schmitt, R. H. H. Neubert, State of the art in research: The biophysical properties of ceramides. *Chemistry and Physics of Lipids* **216**, 91–103 (2018).
101. M. A. Miranda *et al.*, "Lipid Nanocarriers" in Nanocarriers for Drug Delivery: Concepts and Applications, J. O. Eloy, J. P. Abriata, J. M. Marchetti, Eds. (Springer International Publishing, Cham, 2021), 10.1007/978-3-030-63389-9_2 chap. 2, pp. 19–47.
102. E. A. Disalvo, "Membrane Hydration: A Hint to a New Model for Biomembranes" in Membrane Hydration: The Role of Water in the Structure and Function of Biological Membranes, E. A. Disalvo, Ed. (Springer International Publishing, Cham, 2015), 10.1007/978-3-319-19060-0_1 chap. 1, pp. 1–16.
103. R. Feistel, Defining relative humidity in terms of water activity. Part 2: relations to osmotic pressures. *Metrologia* **56**, 1–7 (2019).
104. J. Feher, "2.7 - Osmosis and Osmotic Pressure" in Quantitative Human Physiology (Second Edition), J. Feher, Ed. (Academic Press, Boston, 2017), pp. 182–198.
105. E. Asmus, C. Popp, A. A. Friedmann, K. Arand, M. Riederer, Water Sorption Isotherms of Surfactants: A Tool To Evaluate Humectancy. *J Agr Food Chem* **64**, 5310–5316 (2016).
106. N. Markova, E. Sparr, L. Wadsö, H. Wennerström, A calorimetric study of phospholipid hydration. simultaneous monitoring of enthalpy and free energy. *J Phys Chem B* **104**, 8053–8060 (2000).
107. A. S. Rosa, E. A. Disalvo, M. D. Frías, Dialog Between Phospholipids and Water: Functional Groups Contributions to Sorption Isotherms. *J Phys Chem B* **129**, 8414–8427 (2025).
108. H. Pfeiffer, "Hydration Forces Between Lipid Bilayers: A Theoretical Overview and a Look on Methods Exploring Dehydration" in Membrane Hydration: The Role of Water in the Structure and Function of Biological Membranes, E. A. Disalvo, Ed. (Springer International Publishing, Cham, 2015), 10.1007/978-3-319-19060-0_4, pp. 69–104.

109. H. M. Mansour, G. Zografi, The relationship between water vapor absorption and desorption by phospholipids and bilayer phase transitions. *J Pharm Sci-Us* **96**, 377–396 (2007).
110. E. Y. Shalaev, P. L. Steponkus, Phase diagram of 1,2-dioleoylphosphatidylethanolamine (DOPE): water system at subzero temperatures and at low water contents. *Bba-Biomembranes* **1419**, 229–247 (1999).
111. Anonymous, "The More We Are Together" in Life — As a Matter of Fat: The Emerging Science of Lipidomics. (Springer Berlin Heidelberg, Berlin, Heidelberg, 2005), 10.1007/3-540-27076-0_10, pp. 91–103.
112. Anonymous, "Social Lipids" in Life — As a Matter of Fat: The Emerging Science of Lipidomics. (Springer Berlin Heidelberg, Berlin, Heidelberg, 2005), 10.1007/3-540-27076-0_12, pp. 117–128.
113. C. Aberg, E. Sparr, H. Wennerström, Lipid phase behaviour under steady state conditions. *Faraday Discuss* **161**, 151–166; discussion 273–303 (2013).
114. K. H. Bengt Kronberg, Björn Lindman, "Introduction to Phase Diagrams" in Surface Chemistry of Surfactants and Polymers. (2014), pp. 95–111.
115. X. Q. Yu *et al.*, Interfacial Water Structure of Binary Liquid Mixtures Reflects Nonideal Behavior. *J Phys Chem B* **125**, 10639–10646 (2021).
116. V. Tchakalova, T. Zemb, D. Benczédi, Evaporation triggered self-assembly in aqueous fragrance-ethanol mixtures and its impact on fragrance performance. *Colloid Surface A* **460**, 414–421 (2014).
117. K. Roger, M. Liebi, J. Heimdal, Q. D. Pham, E. Sparr, Controlling water evaporation through self-assembly. *P Natl Acad Sci USA* **113**, 10275–10280 (2016).
118. K. Roger, E. Sparr, H. Wennerström, Evaporation, diffusion and self-assembly at drying interfaces. *Phys Chem Chem Phys* **20**, 10430–10438 (2018).
119. D. F. W. Evans, Håkan, "Bilayer systems" in Colloidal Domain: Where Physics, Chemistry, Biology, and Technology Meet. (John Wiley & Sons Inc, 1999), chap. 6, pp. 295–350.
120. D. F. W. Evans, Håkan, "Polymers in Colloidal Systems " in Colloidal Domain: Where Physics, Chemistry, Biology, and Technology Meet. (John Wiley & Sons Inc, 1999), chap. 7, pp. 351–404.
121. L. A. Clifton *et al.*, Design and use of model membranes to study biomolecular interactions using complementary surface-sensitive techniques. *Adv Colloid Interface Sci* **277**, 102118 (2020).

122. K. W. Swana, T. A. Camesano, R. Nagarajan, Formation of a Fully Anionic Supported Lipid Bilayer to Model Bacterial Inner Membrane for QCM-D Studies. *Membranes-Basel* **12** (2022).
123. B. K. Rastogi, A. Nordoy, Lipid-Composition of Cultured Human-Endothelial Cells. *Thromb Res* **18**, 629–641 (1980).
124. T. Harayama, H. Riezman, Understanding the diversity of membrane lipid composition. *Nat Rev Mol Cell Biol* **19**, 281–296 (2018).
125. D. Oursel *et al.*, Lipid composition of membranes of by liquid chromatography/tandem mass spectrometry using negative electrospray ionization. *Rapid Commun Mass Sp* **21**, 1721–1728 (2007).
126. L. A. Clifton *et al.*, Asymmetric phospholipid: lipopolysaccharide bilayers; a Gram-negative bacterial outer membrane mimic. *J R Soc Interface* **10** (2013).
127. T. K. Lind *et al.*, Formation and Characterization of Supported Lipid Bilayers Composed of Hydrogenated and Deuterated Lipids. *Plos One* **10** (2015).
128. M. Sochorova *et al.*, Permeability and microstructure of cholesterol-depleted skin lipid membranes and human stratum corneum. *J Colloid Interface Sci* **535**, 227–238 (2019).
129. T. Schmitt *et al.*, The long periodicity phase (LPP) controversy part I: The influence of a natural-like ratio of the CER[EOS] analogue [EOS]-br in a CER[NP]/[AP] based modelling system: A neutron diffraction study. *Bba-Biomembranes* **1861**, 306–315 (2019).
130. C. M. M. Beddoes *et al.*, The importance of ceramide headgroup for lipid localisation in skin lipid models. *Bba-Biomembranes* **1864** (2022).
131. N. Sekkat, Y. N. Kalia, R. H. Guy, Biophysical study of porcine ear skin and its comparison to human skin. *J Pharm Sci-Us* **91**, 2376–2381 (2002).
132. B. Godin, E. Touitou, Transdermal skin delivery: predictions for humans from in vivo, ex vivo and animal models. *Adv Drug Deliv Rev* **59**, 1152–1161 (2007).
133. J. Caussin, G. S. Gooris, M. Janssens, J. A. Bouwstra, Lipid organization in human and porcine stratum corneum differs widely, while lipid mixtures with porcine ceramides model human stratum corneum lipid organization very closely. *Biochimica et Biophysica Acta (BBA) - Biomembranes* **1778**, 1472–1482 (2008).
134. I. Vavasour, N. Kitson, A. MacKay, What's water got to do with it? A nuclear magnetic resonance study of molecular motion in pig stratum corneum. *J Investig Dermatol Symp Proc* **3**, 101–104 (1998).

135. P. W. Wertz, "Biochemistry of Human Stratum Corneum Lipids" in Skin Barrier. (Taylor & Francis Group, New York, 2006), chap. 5, pp. 33–42.
136. M. Keramatnejad, C. DeWolf, A biophysical study of tear film lipid layer model membranes. *Bba-Biomembranes* **1865** (2023).
137. A. Olzynska, A. Wizert, M. Stefl, D. R. Iskander, L. Cwiklik, Mixed polar-nonpolar lipid films as minimalistic models of Tear Film Lipid Layer: A Langmuir trough and fluorescence microscopy study. *Bba-Biomembranes* **1862** (2020).
138. S. Inoué, "Foundations of Confocal Scanned Imaging in Light Microscopy" in Handbook Of Biological Confocal Microscopy, J. B. Pawley, Ed. (Springer US, Boston, MA, 2006), 10.1007/978-0-387-45524-2_1, pp. 1–19.
139. E. H. K. Stelzer, Contrast, resolution, pixelation, dynamic range and signal-to-noise ratio: fundamental limits to resolution in fluorescence light microscopy. *J Microsc-Oxford* **189**, 15–24 (1998).
140. H. E. Keller, "Objective Lenses for Confocal Microscopy" in Handbook Of Biological Confocal Microscopy, J. B. Pawley, Ed. (Springer US, Boston, MA, 2006), 10.1007/978-0-387-45524-2_7, pp. 145–161.
141. E. H. K. Stelzer, "The Intermediate Optical System of Laser-Scanning Confocal Microscopes" in Handbook Of Biological Confocal Microscopy, J. B. Pawley, Ed. (Springer US, Boston, MA, 2006), 10.1007/978-0-387-45524-2_9, pp. 207–220.
142. J. B. Pawley, "Fundamental Limits in Confocal Microscopy" in Handbook Of Biological Confocal Microscopy, J. B. Pawley, Ed. (Springer US, Boston, MA, 2006), 10.1007/978-0-387-45524-2_2, pp. 20–42.
143. E. Gratton, M. J. vandeVen, "Laser Sources for Confocal Microscopy" in Handbook Of Biological Confocal Microscopy, J. B. Pawley, Ed. (Springer US, Boston, MA, 2006), 10.1007/978-0-387-45524-2_5, pp. 80–125.
144. B. Dietzek, D. Cialla, M. Schmitt, J. Popp, "Introduction to the Fundamentals of Raman Spectroscopy" in Confocal Raman Microscopy, T. Dieing, O. Hollricher, J. Toporski, Eds. (Springer Berlin Heidelberg, Berlin, Heidelberg, 2011), 10.1007/978-3-642-12522-5_2, pp. 21–42.
145. D. G. Smith Ewen, "Introduction, Basic Theory and Principles" in Modern Raman Spectroscopy. (John Wiley & Sons Ltd, 2019), chap. 1, pp. 1–20.

146. A. S. Rosa, E. A. Disalvo, M. A. Frias, Water Behavior at the Phase Transition of Phospholipid Matrixes Assessed by FTIR Spectroscopy. *J Phys Chem B* **124**, 6236–6244 (2020).
147. P. Larkin, "Chapter 4 - Environmental Dependence of Vibrational Spectra" in Infrared and Raman Spectroscopy, P. Larkin, Ed. (Elsevier, Oxford, 2011), pp. 55–62.
148. V. Zhelyaskov, G. Georgiev, Z. Nickolov, Temperature Study of Intra-Molecular and Inter-Molecular Coupling and Fermi Resonance Constants in the Raman-Spectra of Liquid Water Using Fourier Deconvolution. *J Raman Spectrosc* **19**, 405–412 (1988).
149. N. Ghosh, S. Roy, A. Bandyopadhyay, J. A. Mondal, Vibrational Raman Spectroscopy of the Hydration Shell of Ions. *Liquids-Basel* **3**, 19–39 (2022).
150. D. M. Carey, G. M. Korenowski, Measurement of the Raman spectrum of liquid water. *J Chem Phys* **108**, 2669–2675 (1998).
151. B. Rossi, M. Tommasini, P. M. Ossi, M. Paolantoni, Pre-resonance effects in deep UV Raman spectra of normal and deuterated water. *Phys Chem Chem Phys* **26**, 22023–22030 (2024).
152. S. V. Adichtchev, N. V. Surovtsev, Raman spectroscopy for quantification of water-to-lipid ratio in phospholipid suspensions. *Vib Spectrosc* **97**, 102–105 (2018).
153. E. A. Dobrynina, S. V. Adichtchev, N. V. Surovtsev, Raman spectroscopy characterization of interbilayer water of hydrated phospholipid multibilayers. *Chemistry and Physics of Lipids* **271** (2025).
154. P. J. Caspers, G. W. Lucassen, E. A. Carter, H. A. Bruining, G. J. Puppels, In vivo confocal Raman microspectroscopy of the skin: noninvasive determination of molecular concentration profiles. *J Invest Dermatol* **116**, 434–442 (2001).
155. C. A. Téllez-Soto *et al.*, determination of dermal water content in chronological skin aging by confocal Raman spectroscopy. *Vib Spectrosc* **112** (2021).
156. K. Czamara *et al.*, Raman spectroscopy of lipids: a review. *J Raman Spectrosc* **46**, 4–20 (2015).
157. S. V. Adichtchev, K. A. Okotrub, A. M. Pugachev, I. V. Zaytseva, N. V. Surovtsev, Raman Spectroscopic Study of Phase Coexistence in Binary Phospholipid Bilayers. *Appl Spectrosc* **75**, 87–93 (2021).
158. C. B. Fox, R. H. Uibel, J. M. Harris, Detecting phase transitions in phosphatidylcholine vesicles by Raman microscopy and self-modeling curve resolution. *J Phys Chem B* **111**, 11428–11436 (2007).

159. J. P. Kitt, D. A. Bryce, J. M. Harris, Calorimetry-Derived Composition Vectors to Resolve Component Raman Spectra in Phospholipid Phase Transitions. *Appl Spectrosc* **70**, 1165–1175 (2016).
160. H. Akutsu, Direct Determination by Raman-Scattering of the Conformation of the Choline Group in Phospholipid-Bilayers. *Biochemistry-Us* **20**, 7359–7366 (1981).
161. W. G. Jerome, "The Theory of Fluorescence" in Basic Confocal Microscopy, W. G. Jerome, R. L. Price, Eds. (Springer International Publishing, Cham, 2018), 10.1007/978-3-319-97454-5_2, pp. 21–36.
162. V. Fidler, P. Kapusta, "Fluorescence Kinetics and Time-Resolved Measurement" in Fluorescence Spectroscopy and Microscopy in Biology, R. Šachl, M. Amaro, Eds. (Springer International Publishing, Cham, 2023), 10.1007/4243_2022_31, pp. 53–86.
163. J. Sýkora, P. Kapusta, V. Fidler, M. Hof, On What Time Scale Does Solvent Relaxation in Phospholipid Bilayers Happen? *Langmuir* **18**, 571–574 (2002).
164. M. L. Horng, J. A. Gardecki, A. Papazyan, M. Maroncelli, Subpicosecond Measurements of Polar Solvation Dynamics - Coumarin-153 Revisited. *J Phys Chem-Us* **99**, 17311–17337 (1995).
165. M. J. Sarmento, F. Fernandes, "Choosing the Right Fluorescent Probe" in Fluorescence Spectroscopy and Microscopy in Biology, R. Šachl, M. Amaro, Eds. (Springer International Publishing, Cham, 2023), 10.1007/4243_2022_30, pp. 3–51.
166. B. R. Masters, B. Chance, "CHAPTER 28 - Redox Confocal Imaging: Intrinsic Fluorescent Probes of Cellular Metabolism" in Fluorescent and Luminescent Probes for Biological Activity (Second Edition), W. T. Mason, Ed. (Academic Press, London, 1999), pp. 361–374.
167. A. B. T. Ghisaidoobe, S. J. Chung, Intrinsic Tryptophan Fluorescence in the Detection and Analysis of Proteins: A Focus on Forster Resonance Energy Transfer Techniques. *Int J Mol Sci* **15**, 22518–22538 (2014).
168. R. Brandes, D. M. Bers, Increased work in cardiac trabeculae causes decreased mitochondrial NADH fluorescence followed by slow recovery. *Biophys J* **71**, 1024–1035 (1996).
169. M. Monici, Cell and tissue autofluorescence research and diagnostic applications. *Biotechnol Annu Rev* **11**, 227–256 (2005).
170. Y. H. Fu, N. S. Finney, Small-molecule fluorescent probes and their design. *Rsc Adv* **8**, 29051–29061 (2018).
171. O. Maier, V. Oberle, D. Hoekstra, Fluorescent lipid probes: some properties and applications (a review). *Chemistry and Physics of Lipids* **116**, 3–18 (2002).

172. Anonymous (18:0 Cyanine 5.5 PE. pp Avanti Polar Lipids Inc , https://avantiresearch.com/product/810346
173. Anonymous (18:1-18:1-C11 TopFluor™ TG. pp Avanti Polar Lipids Inc , https://avantiresearch.com/product/810298.
174. Anonymous (Rhodamine B. pp CAS DataBase List , https://www.chemicalbook.com/.
175. P. Willmott, "The Interaction of X-rays with Matter" in An Introduction to Synchrotron Radiation. (2019), pp. 19–49.
176. W. H. de Jeu, "Introduction and Overview" in Basic X-Ray Scattering for Soft Matter. (Oxford University Press, 2016), 10.1093/acprof:oso/9780198728665.003.0001 chap. 1, pp. 1–17.
177. W. H. de Jeu, "Basic Scattering by Particles" in Basic X-Ray Scattering for Soft Matter. (Oxford University Press, 2016), 10.1093/acprof:oso/9780198728665.003.0002 chap. 2, pp. 18–38.
178. T. Hashimoto, "Scattering Structure Factor: Spectral Intensity Distribution of Fourier Modes of Structure" in Principles and Applications of X-ray, Light and Neutron Scattering. (Springer Nature Singapore, Singapore, 2022), 10.1007/978-981-16-1645-7_9, pp. 107–118.
179. A. Nowacka, P. C. Mohr, J. Norrman, R. W. Martin, D. Topgaard, Polarization transfer solid-state NMR for studying surfactant phase behavior. *Langmuir* **26**, 16848–16856 (2010).
180. S. Björklund *et al.*, Stratum corneum molecular mobility in the presence of natural moisturizers. *Soft Matter* **10**, 4535–4546 (2014).
181. A. Nowacka, N. A. Bongartz, O. H. S. Ollila, T. Nylander, D. Topgaard, Signal intensities in H-C CP and INEPT MAS NMR of liquid crystals. *J Magn Reson* **230**, 165–175 (2013).
182. A. Pines, J. S. Waugh, M. G. Gibby, Proton-Enhanced Nuclear Induction Spectroscopy - Method for High-Resolution Nmr of Dilute Spins in Solids. *J Chem Phys* **56**, 1776–& (1972).
183. J. Engstedt, M. Talaikis, J. Barauskas, G. Niaura, V. Kocherbitov, Hydration-induced lipid redistribution in swelling of controlled release liquid crystalline depots. *Commun Chem* **8** (2025).
184. S. Franzé, F. Selmin, E. Samaritani, P. Minghetti, F. Cilurzo, Lyophilization of Liposomal Formulations: Still Necessary, Still Challenging. *Pharmaceutics* **10** (2018).
185. A. Zioud *et al.*, Effects of Drying Methods on Chemical Composition, Lipid Oxidation, and Fatty Acid Profile of a Traditional Dried Meat Kaddid. *Foods* **12** (2023).
186. L. J. Lis, M. Mcalister, N. Fuller, R. P. Rand, V. A. Parsegian, Interactions between Neutral Phospholipid-Bilayer Membranes. *Biophysical Journal* **37**, 657–665 (1982).

187. K. Roger, B. Cabane, U. Olsson, Formation of 10-100 nm size-controlled emulsions through a sub-PIT cycle. *Langmuir* **26**, 3860–3867 (2010).
188. J. M. Andersson, O. Masbernat, K. Roger, Emulsions stabilized by phospholipids. *J Colloid Interface Sci* **678**, 410–418 (2025).
189. L. Yang, L. Ding, H. W. Huang, New phases of phospholipids and implications to the membrane fusion problem. *Biochemistry-Us* **42**, 6631–6635 (2003).
190. R. J. Braun, P. E. King-Smith, C. G. Begley, L. F. Li, N. R. Gewecke, Dynamics and function of the tear film in relation to the blink cycle. *Prog Retin Eye Res* **45**, 132–164 (2015).
191. X. J. Xu, G. L. Li, Y. Y. Zuo, Effect of Model Tear Film Lipid Layer on Water Evaporation. *Invest Ophth Vis Sci* **64** (2023).
192. R. O. Paananen, M. Javanainen, J. M. Holopainen, I. Vattulainen, Crystalline Wax Esters Regulate the Evaporation Resistance of Tear Film Lipid Layers Associated with Dry Eye Syndrome. *J Phys Chem Lett* **10**, 3893–3898 (2019).
193. A. J. Bron, J. M. Tiffany, S. M. Gouveia, N. Yokoi, L. W. Voon, Functional aspects of the tear film lipid layer. *Experimental Eye Research* **78**, 347–360 (2004).
194. A. Tomlinson, S. Khanal, K. Ramaesh, C. Diaper, A. McFadyen, Tear film osmolarity: Determination of a referent for dry eye diagnosis. *Invest Ophth Vis Sci* **47**, 4309–4315 (2006).
195. R. M. Trevorah *et al.*, New Insights into the Molecular Structure of Tear Film Lipids Revealed by Surface X-ray Scattering. *J Phys Chem Lett* **15**, 316–322 (2024).
196. A. Wizert, D. R. Iskander, L. Cwiklik, Organization of Lipids in the Tear Film: A Molecular-Level View. *Plos One* **9** (2014).
197. A. S. Michaels, S. K. Chandrasekaran, J. E. Shaw, Drug Permeation through Human Skin - Theory and Invitro Experimental Measurement. *Aiche J* **21**, 985–996 (1975).
198. B. Stenqvist *et al.*, Membrane permeability based on mesh analysis. *J Colloid Interf Sci* **633**, 526–535 (2023).
199. H. I. Petrache *et al.*, Structure and fluctuations of charged phosphatidylserine bilayers in the absence of salt. *Biophys J* **86**, 1574–1586 (2004).
200. J. van Smeden, M. Janssens, G. S. Gooris, J. A. Bouwstra, The important role of stratum corneum lipids for the cutaneous barrier function. *Bba-Mol Cell Biol L* **1841**, 295–313 (2014).
201. E. H. Mojumdar *et al.*, Stratum corneum lipid matrix: Location of acyl ceramide and cholesterol in the unit cell of the long periodicity phase. *Bba-Biomembranes* **1858**, 1926–1934 (2016).

202. I. Iwai *et al.*, The Human Skin Barrier Is Organized as Stacked Bilayers of Fully Extended Ceramides with Cholesterol Molecules Associated with the Ceramide Sphingoid Moiety. *Journal of Investigative Dermatology* **132**, 2215–2225 (2012).
203. D. Groen, G. S. Gooris, J. A. Bouwstra, New Insights into the Stratum Corneum Lipid Organization by X-Ray Diffraction Analysis. *Biophysical Journal* **97**, 2242–2249 (2009).
204. Q. D. Pham *et al.*, Solid and fluid segments within the same molecule of stratum corneum ceramide lipid. *Q Rev Biophys* **51** (2018).
205. L. Yu *et al.*, A Comprehensive Review of Fluorescence Correlation Spectroscopy. *Front Phys-Lausanne* **9** (2021).
206. I. Sagrafena *et al.*, Structure and function of skin barrier lipids: Effects of hydration and natural moisturizers in vitro. *Biophys J* **123**, 3951–3963 (2024).
207. C. Crous, J. Pretorius, A. Petzer, Overview of popular cosmeceuticals in dermatology. *Skin Health Dis* **4**, e340 (2024).
208. E. K. Pender, B. Kirby, An update on topical therapies for psoriasis. *Curr Opin Rheumatol* **36**, 289–294 (2024).
209. I. Jawed *et al.*, Effect of topical treatment with urea in ichthyosis, atopic dermatitis, psoriasis, and other skin conditions-a systematic review. *Ann Med Surg (Lond)* **87**, 276–284 (2025).
210. J. W. Yang *et al.*, The role and safety of UVA and UVB in UV-induced skin erythema. *Front Med-Lausanne* **10** (2023).
211. R. S. Azfar, A. S. Van Voorhees, "Ultraviolet and laser therapy" in Treatment of Psoriasis, J. M. Weinberg, Ed. (Birkhäuser Basel, Basel, 2008), 10.1007/978-3-7643-7724-3_6, pp. 71–101.
212. T. M. Ansary, M. R. Hossain, K. Kamiya, M. Komine, M. Ohtsuki, Inflammatory Molecules Associated with Ultraviolet Radiation-Mediated Skin Aging. *Int J Mol Sci* **22** (2021).

Acknowledgments

First of all, I would like to thank Emma, my main supervisor, for all the years of guidance and for being a profound educator, leader and supporter. Today, I have no doubt that “Home” was the best place for me to be. Thank you for challenging me in the best ways, for letting me develop as an individual researcher and for solving all my problems when I needed it the most. I will always be grateful for the time I spent under your supervision, as there wouldn’t be enough space to write down how many things I have learned from you.

Secondly, I would like to thank Kevin, my co-supervisor, for never giving up on the research ideas and for showing me that the best experiments are done when they are not planned. Thank you for challenging me and for pushing me to do the tasks that I would rather have skipped throughout all the years. I am very grateful for the time I spent with you in Toulouse, in labs and during beamtimes. It has been a true pleasure to work by your side and to develop as a person and researcher under your supervision. I am very sure that none of this thesis work would have been possible without you.

This thesis would not be possible without so many other scientists and their expertise.

I would like to add special thanks to all the coauthors and collaborators which have initiated and contributed to the articles and manuscripts included in this thesis work. Also special thanks to all the instrument scientists and experimental support at MaxIV and PSI, especially at the ForMAX and cSAXS beamlines.

Special thanks to Enamul, co-supervisor of my master thesis and later coauthor of several articles in this work. Thank you for all the inputs and the discussions over the years and for inspiring me to continue doing research in the same field.

Additional thanks to all the support at physical and computational chemistry division. Especially, Chris, Peter, Maria S., Maria L., for making everything to run smoothly. Thank you for all the support and the discussions that we have had over the years. I could always relay that one of you will always be able to solve any of problems.

Writing this thesis would also not be possible without the incredible people that I have met through these years; the ones that have contributed to the lifelong memories. To my closest office friends. Ismail, my PhD twin… I would not have been able to do all of this without you, from the first particle in a box simulation - to literally finalizing this very acknowledgement section. I am very grateful for having you as a true friend (and bestie) by my side for all the years. I have learned so much from you, mainly because stoicism cannot be practised in peace. In the same vein, I would love to thank

Iria, Najla, Jason, Papu and Monah: for all the time that we shared together, the memories that should never be spoken of, and the memories that will last forever.

Following this, I would also like to thank all the friends and colleagues from the physical and computational chemistry division that have been there for me throughout all the years. Thank you for great discussions, all conferences and after work activities. Special thanks to: David R. for emotional support during all the personal rollercoasters, Ariane for being the most energetic star that lights up the sky, Nizar for coming up with the best and worst advices when I needed it the most, Alex for all the jokes and always lighting up my mood, and David M. for being a sweetheart.

I would also like to thank all the incredible people I have met outside of my division, special thanks to everyone that have been involved in NDR: you guys have been a true source of inspiration. Additional thanks to all the LINXS fellows and YRIs, special thanks to Swati, Daniel, Annika and Oliver for all the work that we have done together.

I also need to acknowledge the most inspiring people and researchers that I have met abroad. To my HERCULES 2024 team, meeting you has been one of the best experiences and during my PhD. Thank you for the most beautiful and challenging weeks in Grenoble, for the LocoMosquito and all the tequila shots that we had all over Europe, which I will never forget. Additional thanks to friends and colleagues that I have met at Biofilms Research Canter in Malmö, especially Hannah, Annie & Jesus, you have been there from the start, thank you for the incredible Karaoke nights, conference trips and shared memories. Additional thanks to all beautiful people that hosted me and made me feel welcome during my stay at Laboratoire de Génie Chimique in Toulouse.

Finally, this thesis would not be possible without the support from my precious family members. Mamie i tacie, dziękuje za bezwarunkową miłość i wsparcie; babci Lili, Krysi i dziadkowi Andrzejowi, za rady i mądrość; i całej rodzinie dziękuję, że mogę zawsze na was liczyć… My beloved sister, Stina, you are the core of my strengh, my grounding rock. Jag älskar dig, och den här boken är dedikerad till dina barn. I tylko dzięki wam, po wszystkich doświadczeniach życiowych, jestem w stanie obronić ten doktorat.

I would need many more pages to acknowledge you all…

Cheers, N

Tryckeriet i E-huset, Lund 2025

ISBN: 978-91-8096-136-3 (print)
ISBN: 978-91-8096-137-0 (electronic)